Creating and probing laser-cooled atomic ensembles inside a hollow-core optical fibre

by

Paul Anderson

A thesis
presented to the University of Waterloo
in fulfillment of the
thesis requirement for the degree of
Doctor of Philosophy
in
Physics (Quantum Information)

Waterloo, Ontario, Canada, 2023

Examining Committee Membership

The following served on the Examining Committee for this thesis. The decision of the Examining Committee is by majority vote.

External Examiner: Guru Dev Dutt
Professor, Dept. of Physics, University of Pittsburgh

Supervisor: Michal Bajcsy
Professor, Dept. of Physics, University of Waterloo

Internal-External Member: Michael E. Reimer
Professor, Dept. of Electrical & Computer Engineering,
University of Waterloo

Internal Member: Alan Jamison
Professor, Dept. of Physics, University of Waterloo

Internal Member: Thomas Jennewein
Professor, Dept. of Physics, University of Waterloo

Internal Member: Adrian Lupascu
Professor, Dept. of Physics, University of Waterloo

Author's Declaration

I hereby declare that I am the sole author of this thesis. This is a true copy of the thesis, including any required final revisions, as accepted by my examiners.

I understand that my thesis may be made electronically available to the public.

Abstract

A laser-cooled atomic ensemble confined inside a hollow-core optical fiber offers a unique platform for enhanced light-matter interactions and their applications. At the same time, transferring a cloud of laser-cooled atoms from a free space magneto-optical trap into the few-micron diameter core of the optical fiber presents a host of experimental challenges (and requires optimization of in a multidimensional parameter space). This thesis investigates loading of laser-cooled caesium atoms into a hollow-core photonic-crystal fiber, develops diagnostic methods to optimize the process and probe the atoms inside the fiber, presents initial experiments exploring the optical properties of the fiber-confined atomic ensemble, and discusses the potential uses of fiber-confined atomic ensembles in 'hybrid' quantum repeaters that utilize quantum dots as source of entangled photon pairs.

Fluorescence-based methods are also employed to estimate atom numbers and assess temperature of the atomic cloud collected initially in the magneto-optical trap and to aid in the alignment of the atom cloud with the fiber's core.

Machine learning, specifically Gaussian processes, is explored as a means to optimize experimental parameters. M-LOOP, a Python-based tool, is utilized for this purpose, demonstrating its ability to navigate around local minima. The influence of dipole beam characteristics, such as intensity and resonance, on loading efficiency is examined, considering factors like Stark shifts and trap depth.

The dissertation also delves into two-photon electromagnetically induced absorption (TPEIA) with cold atomic cesium, highlighting the importance of optical depth for efficient wavelength conversion. The ladder scheme is discussed, showcasing its potential for quantum memory systems with modest delays in electromagnetically induced transparency (EIT) media. The concept of slow light under EIT conditions is presented, illustrating its utility in optical communication traffic buffering and quantum memory. We also discuss the potential uses of this platform in a quantum repeater.

Acknowledgements

Dedication

To Maya and Asuga,

For your unwavering love, patience, and understanding, which have been my greatest source of strength and motivation throughout this journey. Your presence and support have illuminated the path to this achievement, and I dedicate this thesis to both of you, with all my love.

Table of Contents

List of Figures

List of Tables

List of Abbreviations

4WM four-wave mixing 9–11, 15, 66

AI artificial intelligence 39

AOM acousto-optic modulator 31, 53, 58, 67, 77

BEC Bose-Einstein condensate 39

BSM Bell state measurement 8

DAVLL dichroic atomic vapour laser lock 28–31, 33–35, 37, 76, 77

EIT electromagnetically induced transparency iv, 29–31, 33, 34, 69, 70, 72–75, 77, 79

EOM electro-optic modulator 80, 82

GP Gaussian Process 39–42, 45

HCPCF hollow-core photonic crystal fiber 5, 6, 16, 38

ML machine learning 39, 46, 47, 77

MLOO machine learning online optimization 38, 39

MOT Magneto-optic trap 18, 19, 22

NIR near infrared 15

PGC polarization gradient cooling 38, 42, 47

Chapter 1

Introduction

1.1 Interfacing atoms with waveguides

Interfacing light with atomic vapour and atomic clouds has been a major topic in physics for half a century. Mediation of this interaction with waveguides, while a popular and diverse field today, began in earnest with the desire to develop matter-wave interferometers. Such interferometers require atomic analogs to traditional optical elements like mirrors and beamsplitters. Thankfully, it was known that light could manipulate atoms or dielectric particles from works such as Ref. [1, 2]. In fact, it was from Ref. [3] who first suggested the notion of specularly reflecting atoms by means of an evanescent wave. Born & Wolf furthered this with the fact that such a wave could be generated as a result of a field undergoing total internal reflection against a dielectric-vacuum interface (with the evanescent wave forming on the vacuum side) [4]. This was verified experimentally by Balykin (1989) [5] with warm sodium and Kasevich (1990) with cold sodium [6]. These flat "atom mirrors" were successful in bouncing atoms off of them but suffered a spatial drift to a point of low to no evanescent field thought to be due to the small spot size of the source field [6]. This prompted Kasevich to propose the idea of a curved mirror [6]. However, a curved evanescent mirror proved to be more intriguing after initial calculations were performed for it [7]. Such modal structure calculations by Cohen-Tannoudji (1992) pointed to this parabolic evanescent wave having a propensity to confine the atoms within the focus of the field [7]. Thus, combining this with a secondary, counteracting, force like gravity would create an atom trap [7]. Around the same time, there was a proposal by Ovchinnikov et al. (1991), that a trap could also be made using the flat mirror but have two fields incident on the dielectric at different angles with opposite detunings (red and blue); a "push and

pull" trap [8].

It is at this point that we begin to see the evolution of this field into waveguide confinement as Ochinnikov continued the thought from his previous paper further along with Ol'Shaniii and Letokhov with the proposed idea of a glass capillary or hollow fiber with an interior-propagating beam [9]. Such a beam, whose detuning sits below the atomic transition (red-detuned), would create an attractive gradient force, drawing atoms towards the point of highest intensity (namely, the center for Gaussian beams). While this paper was a theoretical proposal, glass capillary fibers were shown to be able to support leaky electromagnetic modes but whose field amplitude propagates predominantly in the capillary's core [10]. Fortunately, these modes are of the zeroth order in Bessel functions (J_0) which have an amplitude maximum in the center [10]. This is important as the notion of a red-detuned beam propagating inside would draw atoms towards the center, away from the walls of the capillary. Such a system was experimentally realized by [11]. While this is not an atom trap as the previous endeavour, this would be the first implementation of an atom interacting with a waveguide.

In terms of atom confinement, there are multiple convex optical resonators employing evanescent light-wave traps, wherein at least one field is red-detuned, creating an attractive force. Simultaneously, a centrifugal force or a blue-detuned field acts as a repulsive counter-force, thereby maintaining atoms in stable orbits around the dielectric, optical resonator's convex shape. An illustrative analogy is the acoustical whispering gallery, characterized by a circular or elliptical horizontal cross-section. Within this gallery or dome, faint sounds propagate with exceptional clarity along the inner wall's circumference, exhibiting minimal attenuation. Similarly, optical whispering gallery mode (WGM) manifest in dielectric resonators with circular cross-sections like spheres or disks, where light propagates through total internal reflection around the periphery. When the circle possesses a radius R, resonance between the geometry and light materializes when an integral number of wavelengths λ encircle the circumference, denoted as $l\lambda = 2\pi R, l \in \mathbb{N}$ [12]. These resonances correspond to the Mie resonances of the dielectric resonator, as explained by van de Hulst in 1981 [12]. The exceptional low-loss total internal reflection characteristic of these optical modes allows optical fields to accumulate to high values, establishing a high-Q cavity [12]. Recognizing that enhanced atom-cavity interaction arises from prolonged interaction times, Mabuchi and Kimble proposed the concept of binding atoms to WGM using the evanescently decaying vacuum field [13]. In this scenario, the atom orbits a dielectric microsphere. These modes, which propagate along the sphere's equator through total internal reflection, generate substantial exponential fields at the dielectric-vacuum interface, as discussed by Treussart et al. in 1994 [14]. The underlying idea involves red-detuning one field to attract the atom to the sphere while counteracting this attraction with centrifugal

2

force (or a blue-detuned field), thereby enabling the atom to orbit the microsphere [14]. While not viewed in the same way as the capillary in terms of an atom interacting with a waveguide, these microstructures are still an important development in mediating the interaction of light and cold atoms in a controllable way.

Whispering gallery resonators offer a unique means of confining and interacting with atoms through an evanescent field, despite not being waveguides, and this concept subsequently led to research on solid fiber waveguides that could achieve both atom confinement through the vacuum side evanescent field and guided light propagation in the core, a few years later. In 2004, Kien, Balykin and Hakuta brought forth this concept with the suggestion of using a subwavelength-diameter optical fiber to facilitate the propagation of red and blue detuned fields to trap atoms close to the outside of the fiber's surface [15]. Such fibers were eventually realized by taking conventional and commercially available optical fibers and taper an inner portion of them to produce this subwavelength-diameter region whose evanescent fields interact with atoms in its vicinity. The first of the synthesis of such a fiber was reported by Mazur et al [16]. around the same time that Hakuta et al. posited the notion of interfacing atoms with these fibers. One of the first interactions with atoms and nanofibers also occurred the next year with the same authors observing spontaneous emission from a cesium atom being coupled into a nearby nanofiber [17]. The inception is culminated by the implementation of the two-colour trapping, which was detailed by Hakuta in the original theory paper, by Kien et al. [18]. Even to this day, there is still active research utilizing nanofibers to trap and interact with atoms.

At this point it would be pertinent to elaborate on the creation and use of photonic crystal hollow core fibers, the very same approach employed in this dissertation. The concept of a photonic crystal fiber was initially introduced by Yeh et al. in 1978 [19]. They suggested the use of a Bragg grating to clad a fiber core, akin to a 1D photonic crystal. In 1992, P. Russell pioneered the development of a photonic crystal fiber constructed with a 2D photonic crystal and an air core [20]. The first photonic crystal fiber was officially documented at the Optical Fiber Conference (OFC) in 1996 and the paper published shortly after [21]. Russell again penned a retrospective article of the decade since the first synthesis of a photonic crystal fiber [22]. There, he lists a few prospective uses for these fibers, including interfacing light and atomic vapour confined in the fiber's core [22]. Coincidentally, it was that same year when Knize purported to be the first to have guided cold atoms (rubidium) in the hollow core of a photonic crystal fiber [23]. Balic reported the same accomplishment about a month later [24].

To this day, each of the above mentioned waveguides are still actively researched with the goal of this dissertation being to provide details on some of the newest experiments with one of these waveguides.

1.1.1 Hollow-core fibers
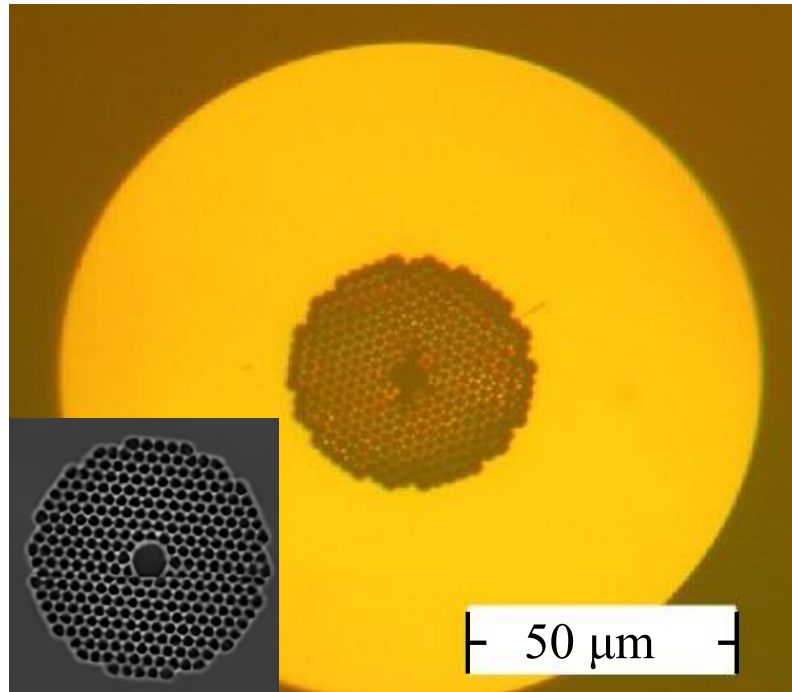
Figure 1.1: Hollow-core photonic crystal bandgap fibers are typically constructed by introducing a periodic arrangement of air holes or voids in the glass cladding region of the fiber. The periodic arrangement of air holes creates a photonic bandgap within the fiber. This bandgap corresponds to a range of wavelengths where light cannot propagate in certain modes. Essentially, the fiber acts as a "photonic insulator" for these wavelengths. Pictured is a hollow-core fiber optimal for 850 nm light (cesium D2 line); the band permits 750-950 nm light with reasonable efficiency which encompasses all of our interested wavelengths.

Hollow-core fibers are waveguides similar to standard commercial optical fibers in that they both guide light within a core that is surround by a glass cladding, however standard fibers have a solid, glass, core whereas the aptly-named hollow-core fiber is guiding light within vacuum or air (figure 1.1). Traditional optical fibers guide light through total internal reflection, where light rays incident at certain angles are trapped within the core of the fiber due to the difference in refractive index between the core and the cladding. Total internal reflection demands that the core be of higher refractive index than the cladding which is impossible for a hollow-core fiber. Therefore, these fibers must guide in a different way. There are two major types of hollow-core fiber whose guiding physics are

4

slightly disparate. There are Kagome fibers which consist of a lattice of interconnected hollow capillaries arranged in a pattern that resembles the Kagome lattice, a geometric lattice featuring triangular and hexagonal voids. Such fibers have both a fundamental core mode as well as cladding modes at the same frequency and propagation constant, but weak interactions of these cladding modes with the fundamental mode leads to core guidance [25]. Alternatively, a hollow-core photonic crystal fiber (HCPCF), is a type of optical fiber that utilizes the concept of a photonic bandgap to guide light. They are typically constructed by introducing a periodic arrangement of air holes or voids in the cladding region of the fiber. This periodic structure creates a photonic bandgap, which is a range of frequencies where fundamental mode propagation of light is forbidden. As for the reason why one would opt for a hollow-core fiber over a solid-core fiber, it will predominantly be to take advantage of the enhanced interaction between the core-guided light and something placed inside the core. This began with room temperature gases or vapour [22] and evolved into cold atoms [23].

1.1.2 Cold atoms inside hollow-core fibers

The benefit of facilitating light-atom interactions with a hollow-core fiber extends beyond the simple observation of overlapping the atoms and light spatially. Light guided in the core of the HCPCF used in our lab has a mode-field diameter of 5.5 μm. Such a small diameter means that high intensity beams can be achieved at lower powers. To understand what intensities are needed, we can look at some Rabi frequency values for some useful transitions in the atom of choice which is cesium. The transitions we are interested in are the $6S_{1/2} \rightarrow 6P_j$ and $6P_j \rightarrow 8S_{1/2}$ transitions, with $j = \frac{1}{2}, \frac{3}{2}$. For relatively strong pump beams to be used experimentally, we would want the Rabi frequencies to exceed the linewidth of the particular transition. This is more eloquently depicted using the saturation parameter, s. A good illustrative approximation can be taken from [26], where the saturation threshold $s = 1$ is achieved when $\Omega \approx \gamma/\sqrt{8}$. For cesium, this means a Rabi frequency of $\sim$MHz. In terms of intensity, this would be a few mW/cm^2 which is readily achieved inside the HCPCF using only 200-300 pW of power. In terms of the probe field, we would ideally want single-photon powers. For the two possible probe transitions, the energy of those photons would be 0.22 eV and 0.23 eV for 894 nm and 852 nm, respectively. If these photons are emitted at a rate of 1 MHz, the effective power of this stream would be about 0.035 pW and 0.037 pW which leads to an intensity inside the fiber of 0.22 μW/cm^2 and 0.23 μW/cm^2 for 894 nm and 852 nm, respectively. The objective is to observe single-photon nonlinearities using the cold atoms, and while increasing the power of the single photon stream is not a flexible option (the energy of the photon is fixed and the photon

rate is limited by the type and quality of the source), increasing the intensity using the HCPCF is. Not only does this tight confinement help the intensity of the photons, it also provides atom cloud confinement to allow for a potentially large optical depth.

In the context of an ensemble of cold atoms, optical depth refers to the measure of how effectively the atoms attenuate or absorb light, quantifying the degree to which the atoms interact with and modifies an incident optical beam. Mathematically, it is quantified by $OD = n\sigma_a L$ for a density, n, of atoms across a length, L, with an absorption cross-section, σ_a. The significance of this is revealed in two key ways. First, optical depth is seen as a benchmark for photon storage inside atomic ensembles; it being the key parameter in characterizing storage efficiency [27, 28]. More specifically, the benchmark for good storage efficiency is $OD \gg 1$ [27]. Second, the optical depth is important when attempting to store large bandwidth photons. For photons of bandwidth, $\Delta\nu$, good storage efficiency is achieved for $OD \gg (\Delta\nu/\gamma)$ in atoms with a linewidth, γ [28]. There are two interesting points to take from this. One is that, once again, a large optical depth is required if storing large bandwidth photons is desired. Two, while large optical depths is achievable in warm atomic vapours, the linewidth will be much larger due to inhomogeneous broadening. This means that an even larger optical depth would be required in warm atoms, comparatively.

How the HCPCF helps with accessing large optical depths in cold atoms can be quantified by the ratio $\sigma_a/A_{\mathrm{mode}}$, where A_{mode} is the modea area inside the waveguide. This is a helpful quantity that is used to characterize the potential for using certain waveguides to help interface light with atoms, and it is a major reason for our use of HCPCFs [29]. For a more visual context given the previously mentioned benchmark, this ratio implies that only about 50 cesium atoms are needed inside the fiber to give an optical depth of 1. Additionally, cold atoms afford potentially long coherence times for photon storage given their narrow linewidth compared to warm atoms. Solid state systems have shown the possibility of long coherence times, but with a trade-off of low optical depth and restrictions in increasing optical depth without increasing homogeneous decay [27].

While it has been established why cold atoms inside HCPCFs could prove to be a tantalizing platform for single-photon nonlinearities and good (large bandwidth) photon storage, the context of why this is needed was not established. A number of motivations such as synchronization in quantum computation and converting heralded photon sources into on-demand sources have appeared in literature [27]. For our particular intentions, we wish to take advantage of this system in order to realize at least one node of a quantum repeater.

1.2 Quantum Repeaters

Quantum repeaters are a crucial component in the field of quantum communication and quantum networking. This is due to a problem that similarly appears in classical communication: imperfect or lossy communication channels. For the quantum analog, when quantum states travel through optical fibers or other communication media, they inevitably experience loss, causing the quantum information to degrade and become unusable. Like their classical counterpart, quantum repeaters address this fundamental challenge in quantum communication, known as quantum channel loss. This challenge is exacerbated due to the fragile nature of quantum states, which are easily affected by decoherence and loss (e.g. attenuation) as they travel through communication channels, such as optical fibers.
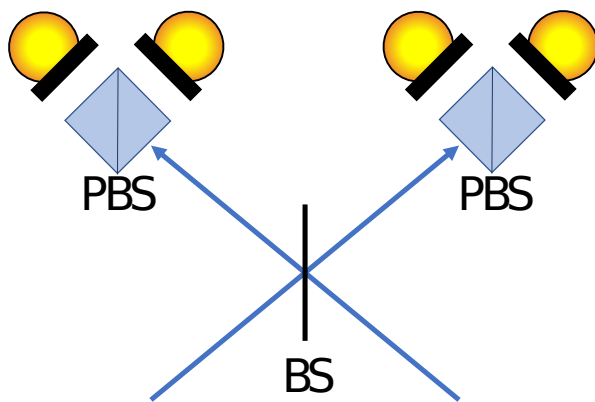
Figure 1.2: An example of a Bell state measurement for a polarization based photonic qubit.

Repeaters used in classical communication amplify and regenerate signals to overcome signal loss. However, in the quantum realm, the "no-cloning theorem" prevents direct copying of an arbitrary unknown quantum state, making traditional amplification impossible. Quantum repeaters offer a solution in a couple of ways. The first approach to this problem

by exploiting the principles of quantum entanglement and swapping. The methodology is as follows: entanglement–a quantum phenomenon where two or more particles become correlated in a way that the state of one particle affects the state of another–must be generated. Given that a flying qubit is required for communication, typically an entangled pair of photons is used. Second, one of the entangled photons is sent across the quantum channel as far as possible, while the decoherence is manageable. At this distance, a second entangled photon pair must be generated and entanglement swapping must be performed. The goal is to have entangled particles shared between what are referred to as quantum repeater nodes (the sites at which entanglement is generated and swapped). What this means is that, if the first node produced an entangled pair denoted as AB and sent photon B to the second node which produced the pair CD, then entanglement swapping will create the entangled pair AD at the cost of photons B and C. This is ultimately done in two steps. At each node (the locations of photons A and D), a measurement called a Bell state measurement (BSM) is performed on particles B and C. A Bell state measurement is a special type of quantum measurement that projects the entangled particles onto one of the four possible Bell states. The implementation of this measurement depends on the nature of the qubit. A BSM on a polarization-based photonic qubit can be done using waveplates and polarizing beam splitters (see figure 1.2). The outcome of the BSM on photons BC will be one of the four Bell states which dictate what corrections need to be applied to photon D to generate entanglement with photon A. Thus, creating entanglement between particles that have never directly interacted by using intermediary particles that were once entangled with each of the distant particles. By having multiple of these intermediate nodes, each of which performs entanglement swapping and error correction processes, one can effectively "renew" the quantum states. This allows them to traverse longer distances without losing too much fidelity.

To realize at least one node of a quantum repeater, we need a single photon source that gives us an entangled photon pair to initiate the entanglement swapping between two nodes as mentioned above. To make this a more versatile source for a quantum repeater, it would be preferential for the wavelength to be long-lived in an optical fiber so we can separate adjacent repeater nodes as far as possible, reducing the total number of nodes needed. Our approach to this is through quantum dots. We utilize InAsP quantum dots that are grown embedded in InP nanowires. Quantum dots are similar to atoms in their ability to produce single photons when excited by a laser but have the benefit of being solid state without the need for trapping them. This similarity can also be seen in the general depiction of the quantum dot's level diagram as seen in figure 1.6. They have the ability to produce a photon pair by excition of a state known as the biexciton (XX) and via a cascade mechanism [30]. Let us take a closer look at the general scheme for
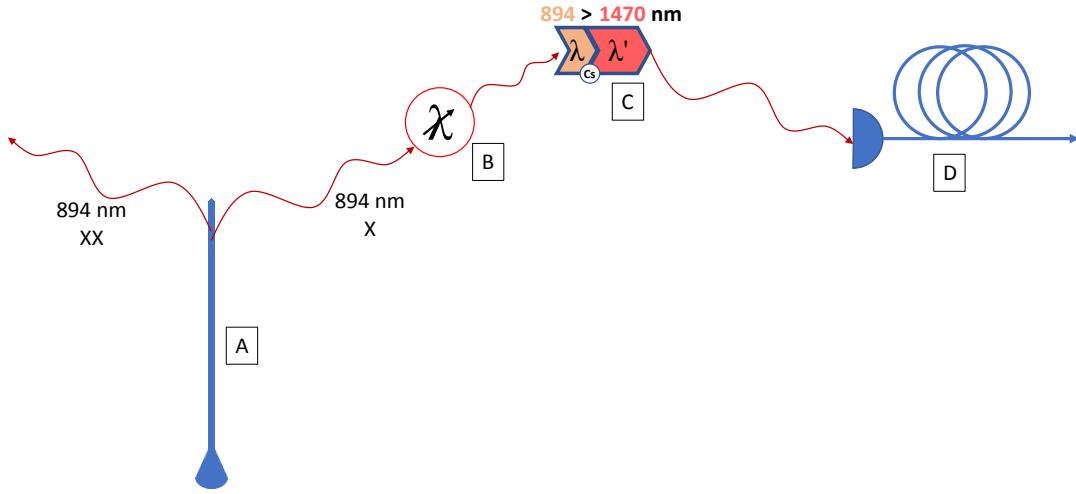
Figure 1.3: Suggested scheme for telecom single photon source. A is an example of an InAsP quantum dot embedded in an InP nanowire. B represents the wavelength tunability of the quantum dot which is done via gas injection in the cryostat housing the quantum dots. C represents the conversion from the base emission around 894 nm to 1470 nm which is longer-lived in optical fibers. This will be done with four-wave mixing in cold atomic cesium. Finally, the converted telecom photon can be coupled into an optical fiber for long distance fiber (D).

single photon generation and manipulation with our system. The pictorial overview can be found in figure 1.3. We begin with a single quantum dot embedded in a nanowire (figure 1.3.A) excited to the biexciton (XX) state. This will lead to a photon pair being generated with a wavelength around 894 nm. *The many levels available to atoms like cesium contributes to nonlinear phenomena such as three and four-wave mixing (4WM). This, 4WM in particular, is discussed in more detail in chapter 6.1 with figure 6.1 visually showing the possible 4WM schemes. To simplify, a photon resonant with the D1 line of cesium can be converted into either a 794 nm or 1470 nm photon through 4WM. The benefit of this is to have a photon that can either be long-lived in atmospheric transit (794 nm) [31] or in an optical fiber (1470 nm) [32]. Our focus is the conversion to telecom

9

which is illustrated in figure 1.3.C which is culminated by the converted photon being coupled into a telecom fiber for long distance transit shown in figure 1.3.D. A zoomed-out overview of what the quantum repeater network could look like with these nodes is shown in figure 1.4. This overview includes the key components outlined in figure 1.3 as well as the two possible means of transmitting photons across long distances in optical fibers and satellite links. A theoretical simulation of photons interacting with cesium under 4WM conditions was performed (refer to chapter 6 and figure 6.2) and found that a previously achieved optical depth of 100 was capable of converting an 894 nm photon into 1470 nm at an efficiency of about 80 %. The importance of this is revealed when comparing the transmission loss in an optical fiber between the two wavelengths. Figure 1.5 not only shows that 1470 nm heavily outperforms 894 nm, but that such a conversion efficiency would begin to outperform 894 nm transmission in less than 1 kilometer. This completes the picture for the proposed single photon source which can produce single photons and entangled photon pairs that can interact with cold cesium as well as be sent across long distances through fibers or space. Of course, one can question the need to interact with atoms. Is it necessary, or would opting for a more direct source of telecom photons suffice if long-distance communication is the priority? This question can be answered by recalling that tuning the photons to resonance with cesium creates two possibilities. The first of wavelength conversion was just discussed, the second is utilizing the cesium atoms as a quantum memory.
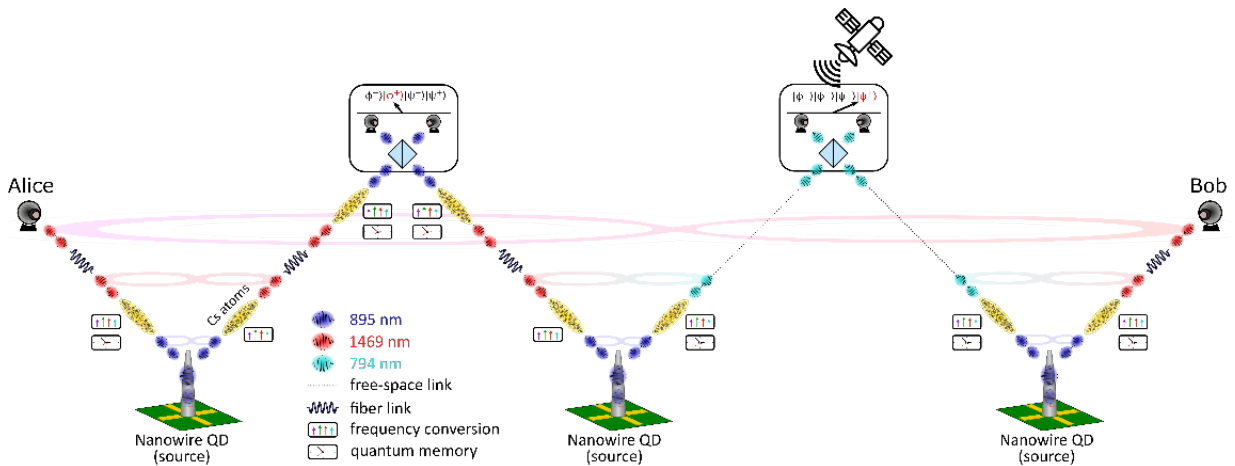
Figure 1.4: Large overview of quantum repeater network realized by nodes investigated in this lab. Both fiber-based and satellite-based photon transmission are illustrated. Credit to Dr. Rubayet Al Maruf for creating this figure.
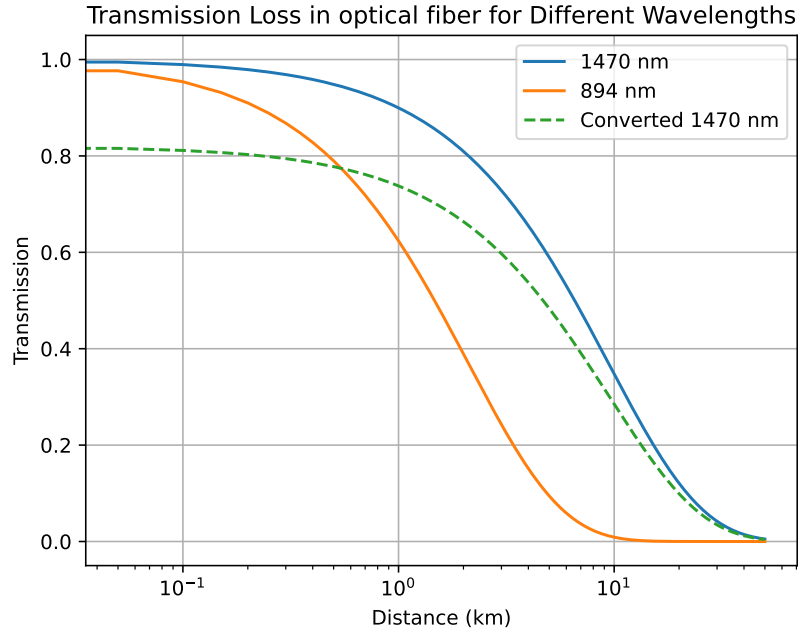
Figure 1.5: Transmission loss of different photons travelling through an optical fiber as a function of distance. The longer-lived telecom photon (1470 nm) expectedly experiences significantly less loss per kilometer than an 894 nm photon. The converted 1470 nm photon represents an 894 nm converted to 1470 nm using 4WM in cesium. The conversion efficiency of 80% has been theoretically shown to be possible with an optical depth of 100 (per figure 6.2).

In describing the implementation of a quantum repeater node, a few important details must be elucidated. First, while the concept of sending a flying qubit like a photon to another location to perform a measurement is relatively straightforward, the notion of holding such a qubit in one spot is not. However, this is exactly what needs to happen to one photon while the other photon is in transit to the next repeater node. Hence the aforementioned second use for cold cesium atoms: a quantum memory. More precisely, a quantum memory with a lifetime that exceeds the time it takes for the photon to arrive at the next node and a Bell state measurement to be performed. If one can push the lifetime of the memory to millisecond timescales, the distance between nodes can be pushed to 100's of kilometers. Moreover, generating entangled photon pairs is a notably intricate task, and the specific characteristics of these photons are a pivotal factor influencing the

choice and quality of the quantum memory. Photons generated the popular periodic-polling technique have bandwidths in excess of 10 GHz, even reaching 100 GHz [33]. Such photons are difficult to store for long periods of time which restricts the choice and execution of the memory. Thus, our quantum dot source which exhibits a bandwidth of 1-3 GHz works comparitively much better with a cold atom memory. This gives us all the key ingredients to realizing a quantum repeater node and now we must experimentally demonstrate the viability of the key steps outlined.

1.3   Experimental approach

Our ultimate goal of realizing a quantum repeater node is separated into two components as touched upon in the earlier section: a good source photons with as narrow a bandwidth as possible, and a quantum memory with a lifetime approaching millisecond to second lifetimes [34]. We have chosen to satisfy these with quantum dot (QD) embedded in nanowires as our photon source, and cold atomic cesium as our quantum memory.

1.3.1   Tunable photons from nanowire-embedded quantum dots
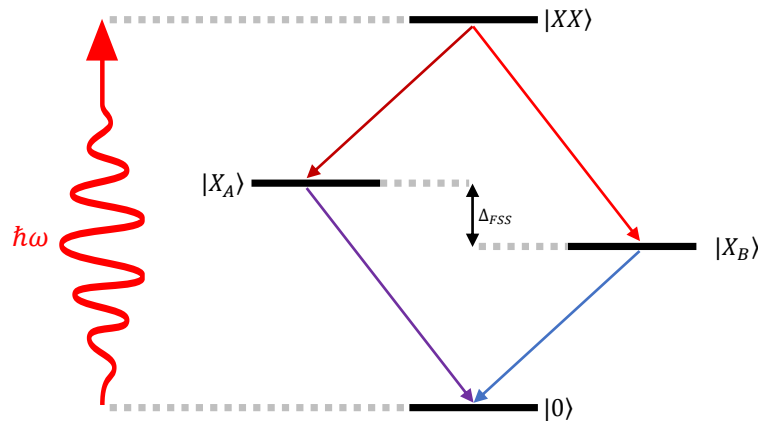
Figure 1.6: Schematic level diagram of the radiative biexciton-exciton cascade for a polarization entangled photon source.

Quantum dots are typically made from semiconductor materials, such as gallium arsenide, or cadmium selenide. These materials have a band gap, which is the energy difference between their valence band (highest energy level filled with electrons) and their conduction band (lowest energy level with available electron states). With diameters typically in the range of a few nanometers, quantum dots exhibit quantum confinement effects. This means that the energy levels available to electrons and holes (electron vacancies in the valence band) become quantized, resembling discrete energy states similar to those in atoms. This comparison to atoms extends to the ability to generate photons by exciting these dots with a laser.
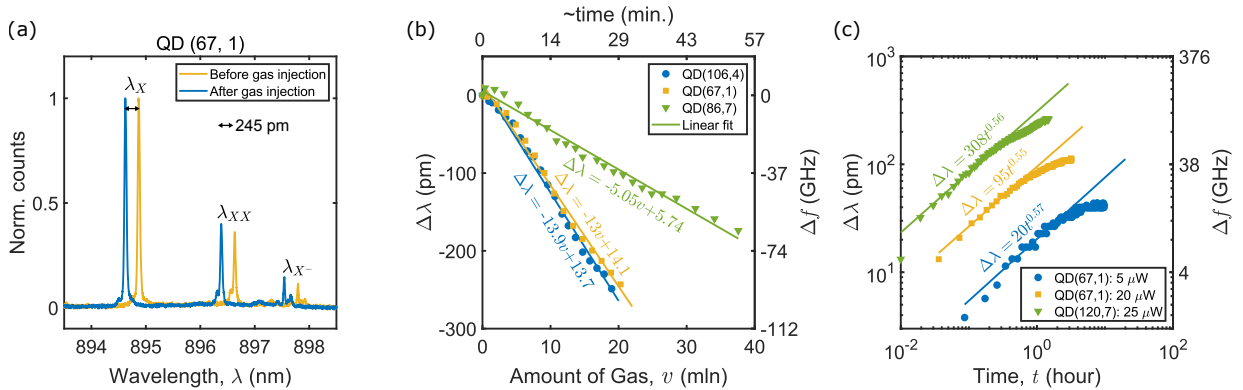
Figure 1.7: (a) Quantum dot emission observed on the spectrometer before and after gas injection. (b) Wavelength shift induced by gas injection: Shown are measurements from three specific quantum dots (e.g., QD(106, 4) indicating the quantum dot's position in a grid). The lower (upper) x-axis depicts the quantity of injected gas (time elapsed), while the left (right) y-axis represents changes in wavelength (frequency) of the emission spectrum. Circles, triangles, and squares represent experimental data points, and the solid lines represent linear regression fits. The corresponding fit equations are displayed alongside the lines. (c) Wavelength shift resulting from laser ablation: Symbols represent experimental data points, and solid lines represent linear fits displayed on a logarithmic scale ($\propto at^b$). Higher laser power results in a faster ablation of N_2 ice, causing a more rapid initial wavelength change. However, the wavelength shift tends to stabilize over time as the amount of evaporated nitrogen locally equilibrates due to redeposition.

Our desire is to use InAsP quantum dots embedded in InP nanowires developed by our collaborators of Philip J. Poole and Dan Dalacu at the National Research Council and researched by our collaborators in the group of Michael E. Reimer at the University of Waterloo [30]. There are several reasons which make this particular photon source

compatible and advantageous for our cold atom setup. The first is that the photons produced by these dots emit very close to the D1 line of cesium of 894 nm.

This wavelength depends on the synthesis of the dot as well as any applied stress on the nanowire. While the former is what leads to the emission in the vicinity of 894 nm, the latter notion of applied stress is of particular intrigue. More specifically, this applied stress comes in the form of injected nitrogen condensing onto the nanowire. This nitrogen gas enters the cryostat by means of a high-accuracy flow controller and proceeds to condense onto the sample's substrate and the nanowire, itself. The outcome is a shift in wavelength of the emission of all quantum dot states. This phenomenon is more explicitly outlined in figure 1.7. Each subplot of this figure demonstrates the shifting of the emission wavelength–for biexciton, exciton, and charged exciton states equally–due to the amount of nitrogen gas injected. This wavelength tunability is highlighted as part B of figure 1.3 which enables adjustment on the picometer level. The reason behind the effort to fine tune the wavelength is to resonate the photons with the D1 line of cesium. This opens the door to two major possibilities, the first of which is wavelength conversion.

The second is the embedding of the dot inside a nanowire which grants two advantages. The coupling of the emission of the dot into the nanowire provides confinement into two modes, (forwards and backwards along the transverse direction of the nanowire) allows us to couple the into a single mode optical fiber with high efficiency to be interface with the cold atoms [35, 30]. The nanowire quantum dot has also shown to produce short bandwidth photons on the order of GHz which is easier to use with cold atoms compared to other solid state photon sources [35, 30, 36]. Furthermore, this quantum dot system has been shown to be able to produce a pair of strongly entangled photons which grants us access to a scheme to build a quantum repeater node [30]. This pair arises from optically exciting the dot into a biexciton state leading to a biexciton-exciton radiative cascade delay (see figure 1.6) [30]. Finally, our recent work has demonstrated the ability to tune the emission wavelength of these quantum dots on the picometer level [36]. This method which involves the injection of nitrogen gas into the cryostat housing the dots causes a strain (due to condensation) that shifts the wavelength [36].

The result is a source of narrow-bandwidth entangled photon pairs whose frequency can be tuned close to an atomic transition which grants access to both wavelength conversion and quantum memory schemes with cold atomic cesium.

1.3.2 Cold atoms

There are many possible media for use as a quantum memory. Such media include solid-state systems like Nitrogen-vacancy centers [37], superconducting circuits [38], and ion-traps [39]. The choice of cold atoms is made for a few key reasons. The most notable being the promise of long lifetimes within cold atom memories [34], but also the flexibility in accepting larger bandwidth photons using Autler-Townes splitting [40] or far-off Raman memories [41]. Moreover, the particular narrow-bandwidth high-efficiency quantum dots being used as the photon source emit in the near infrared (NIR) band close to the D1 line of cesium (see figure 1.7.A). Finally, regardless of choice of photon source and quantum memory, one would have to often choose the photon frequency to match the choice of quantum memory. This choice may often be sub-optimal for communication channels; namely, telecom frequencies for long-lived optical fiber transit [32] or 750-800 nm wavelengths for satellite communications [31]. However, the choice of cesium enables not only photon storage. If one takes advantage of the level structure of cesium, one can convert the frequency of the photon to either telecom or 794 nm which is a low-loss wavelength for ground-to-satellite link [31] via the nonlinear 4WM effect (see chapter 6).

The major challenge with the use of cold atoms is, despite the quantum dot emission being on the lower end of bandwidth compared to other solid-state sources, a GHz bandwidth is still large compared to the linewidth of atoms on the order of MHz. Thus, to gain the benefits of cold atoms while still being able to implement storage and wavelength conversion with good efficiency, a high optical depth is required (this is outlined in more detail in figure 6.2). This can be done with warm atoms or cold atoms with optical lattice trapping. the second problem is that the power of a true single photon source is limited in its power by its frequency and its efficiency (repetition rate). Since the efficiency of photon storage and wavelength conversion also depends on the light's intensity, the only option to adjust this for the photon source is to have a more focused beam. In free space, this can be difficult as simply focusing the light to a small size will lead to a rapidly diverging beam (i.e. a short Rayleigh length). Attempting to have a smaller spot sized collimated beam means very high quality lenses and extremely mechanically stable lens housings. It would be beneficial to have a means of combining the small mode field diameter of optical fibers with the ability to interact with cold atoms.

1.4 Experimental setup

Our experiment is outlined in figure 1.8, we have chosen to utilize a HCPCF which enables us to interface light with a large range of wavelengths (750-950 nm) and cold cesium atoms all within a small cross section of about 7 μm. A 2 cm segment of this fiber is mounted vertically inside a vacuum cell, with all necessary light source coupled in from the bottom via free space (see figure 1.8). Loading atoms into the core of the fiber is done by magneto-optically trapping cesium, sourced by heating an alkalai dispenser, directly above the fiber segment. Once the atom cloud has equilibrated, the magnetic fields are turned off and the atoms are released. immediately upon release, the atoms undergo additional cooling down to 15 μK via polarization gradient cooling. The result is a cloud with minimal expansion, whose motion is predominantly down towards the fiber core due to gravity. We enhance the loading efficiency by coupling a red-detuned attractive dipole beam into the fiber which acts as a funnel to guide more atoms towards and into the core. We employ polarization and spectral filtering to remove the dipole trap from any probe measurements.
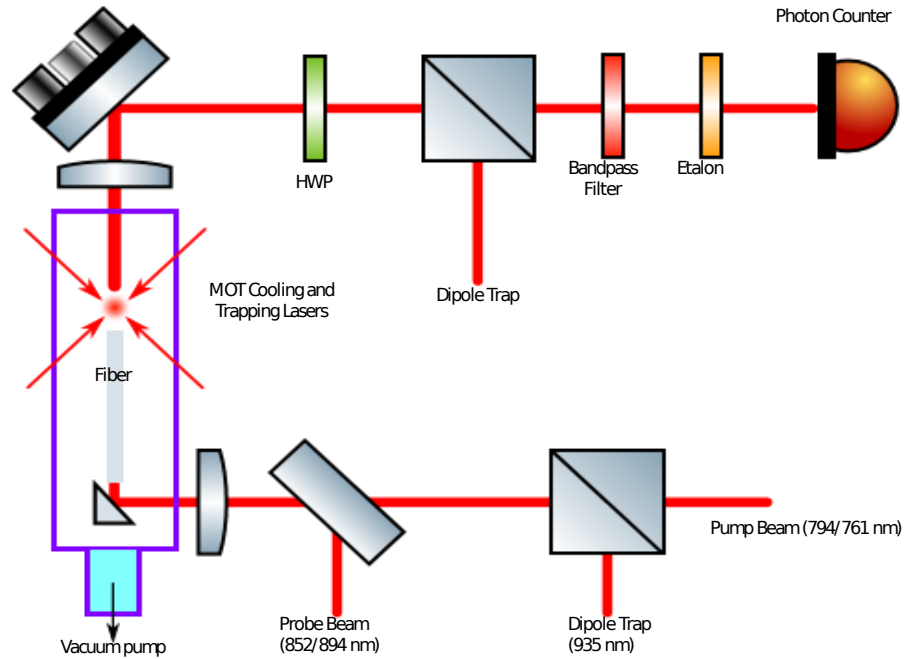
Figure 1.8: The experimental setup is as shown above. Atoms dispensed from a cesium source are first slowed and trapped, just above the fiber segment, by a magneto-optical trap. Typically 60 million atoms are trapped before being released via the turn off of trapping beams and magnetic field. Once released, polarization gradient cooling is employed to bring the cloud temperature to below 15 μK. These cold atoms will drop towards the core of a hollow-core fiber via gravity and a red-detuned attractive dipole beam. After loading, any necessary pump and probe beams are coupled into the fiber and timed with the drop of the atoms. The probe is collected and sent to a SPCM after some polarization and spectral filtering.

Chapter 2

Diagnostics

Like all increasingly complex experimental setups, in order to either fine-tune or investigate the source of problems, a set of diagnostic tools is extremely useful. For this experiment, the major potential problems are either with the atom cloud (e.g. density, temperature, trajectory towards fiber) or fiber coupling (i.e. mode quality). This chapter will outline and detail each diagnostic tool created for this experiment.

2.1 Fluorescence of a laser-cooled atom cloud in free space

While a qualitative view via camera of an atom cloud can be sufficient and simple for most use cases in cold atom physics, a quantitative analysis via the same camera can really aid in attempts to optimize the density of trapped atoms.

To implement this analysis, we can take an equation from Steck's report on Cesium [42] which relates the number of atoms with to details about the Magneto-optic trap (MOT) and the CCD sensor used:

$$N_{atoms} = 8\pi \frac{1 + 4\left(\Delta/\Gamma\right)^2 + \left(6I/I_{sat}\right)}{\Gamma\left(\dfrac{6I}{I_{sat}}\right) t_{cam}\eta_{cam}d\Omega} \tag{2.1}$$

Where everything is with respect to the trapping transition of the MOT ($F = 4 \to F' = 5$ for Cesium). Δ is the detuning of the light from the transition, Γ is the natural linewidth,

I is the intensity of a single beam of a 6-beam configuration, I_{sat} is the saturation intensity (2.7 mW/cm^2 for cesium MOTs), t_{cam} is the camera's exposure time, and η_{cam} is the counts/photon efficiency of the camera. Finally, since the light emission will occur across the 4π solid angle of the cloud and only a fraction of that will reach the camera sensor, $d\Omega$ represents the fraction of light that reaches the sensor. We can write this fraction as [42]:

$$d\Omega = \frac{\pi}{4}\left(\frac{f}{(f/\#)\,d_0}\right)^2 \tag{2.2}$$

For an imaging system with imaging focal length, f, and f-number, $f/\#$, a distance d_0 away from the cloud.

While this number may not be an exact representation of the number of atoms in the cloud due to uncertainties in the camera distance, power calibration, as well as the camera's resolution, this value should still give a good estimate for optimization purposes.

2.2   Absorption imaging of an atom cloud in free space

2.2.1   Atom number

An alternative approach to imaging the emission of the atoms is to instead turn off the trapping and repumping beams and shine a large collimated resonant beam through the cloud and into the camera. The atoms will absorb light from this beam and the cloud's shape will be imprinted as a "shadow" on the camera sensor (see Figure 2.1). From here, a similar measurement as outlined in 2.1 can be done. Except we no longer need to worry about the fraction of light hitting the camera. We do not even have to worry about calibrating the power with the camera pixels. We can use Beer-Lambert's law to get the atomic density of the cloud.

$$I = I_0 e^{-\eta\sigma L}$$
$$\eta = \frac{\ln\left(\frac{I_0}{I}\right)}{\sigma L} \tag{2.3}$$

Where I is the measured intensity, I_0 is the unperturbed intensity, σ is the absorption cross section of the atomic species for this transition, η is the atomic density, and L is the length of the cloud. As one can see, we do not need to know the conversion between intensity and pixel value. We only need to know the pixel value with and without the cloud to compute $\ln\left(\frac{I_0}{I}\right)$. From here, the calculation is carried out per pixel and the resultant value will be
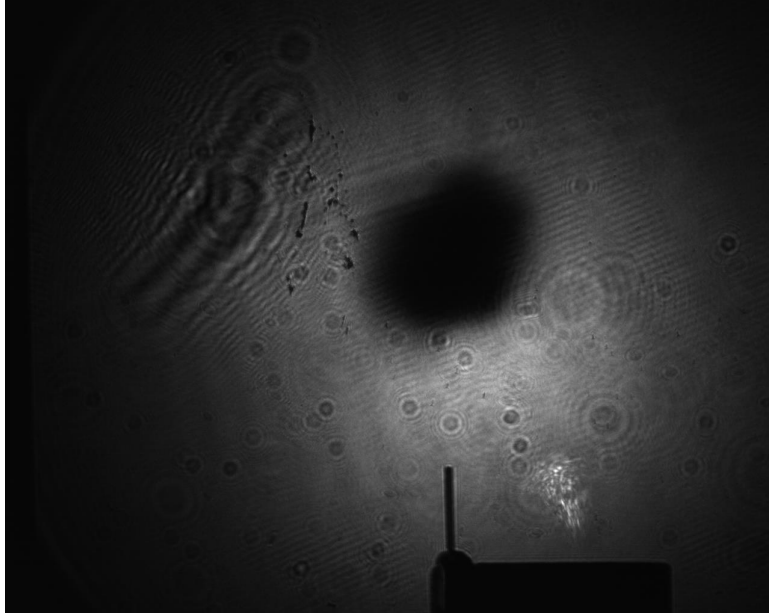
Figure 2.1: Example of an absorption image of a cesium cloud over a mounted hollow-core fiber. The only source of light is coming from a collimated laser beam resonant with $|F = 4\rangle \rightarrow |F' = 5\rangle$. The imperfections visible are due to debris on the CCD coupled with the monochrome nature of the light.

a column density of atoms (ηL). By multiplying this value by the pixel area, we arrive at the number of atoms in that particular pixel. Therefore, the total number of atoms is:

$$N = \frac{A}{\sigma} \sum_{i=0}^{M} \ln \left(\frac{I_0}{I_i} \right) \tag{2.4}$$

Where I_i is the intensity value of the ith pixel and A is the area of an individual pixel.

2.2.2   Temperature of a laser-cooled atomic cloud

The number of atoms alone does not indicate good loading into the hollow-core fiber. The atoms must be sufficiently cold such that the expansion of the cloud is not too great to cause the atoms to miss the core during free fall. A full calculation of the temperature

requires taking several absorption images at different times during the free fall (i.e. time of flight). The temperature of an atom comes directly from their velocity; the relation of which is from the Boltzmann distribution,

$$v = \sqrt{\frac{3k_B T}{m}} \tag{2.5}$$

Where m is the mass of cesium and k_B is the Boltzmann constant. So if one can get the average velocity of atoms in the cloud, one can easily calculate the temperature. To get the average velocity, we look at the expansion of the cloud and measure the change in radius of the cloud. If we know the time lapsed between images and the change in radius, we can calculate the velocity needed to cause that expansion. We can substitute $v = \frac{r}{t}$ in (2.5) and rewrite it in terms of the radius change,

$$r = \sqrt{\frac{3k_B T}{m}} t + r_0 \tag{2.6}$$

where k_B is the Boltzmann constant and m is the mass of a cesium atom. Fitting this equation will arrive at the temperature for the atomic cloud.

2.2.3   Two-view analysis

Performing a time of flight measurement is primarily used for calculating temperature, however it also proves useful for characterizing the trajectory of the cloud towards the fiber. Ideally, we would like to have a top-down view of the cloud but, due to coupling optics for the probe light exiting the fiber, there is no space to place a camera. To compensate, we can approximate this view using two cameras placed 90° from each other along the other dimensions (see figure 2.2). While this does not enable us to perfectly resolve the top-down view, we are able to map the centroid of the cloud with respect to the fiber as it falls. With this information, we can adjust the magnetic field to push the centroid to be directly above the fiber. This tells us not only the position where the densest part of the cloud is, but also when that part has reached the fiber core. This is incredibly valuable as we wish to time our probe pulse with the cloud being completely inside the fiber. One can still see absorption of the probe due to atoms outside the fiber, but there is a significant increase in optical depth once the atoms fully enter the core. This can be observed with a frequency scan across different time delays of the probe pulse (see chapter 6). However, resolving the optical depth requires multiple probe pulses at different detunings which is significantly more time consuming than looking at the free fall of the cloud using two cameras.
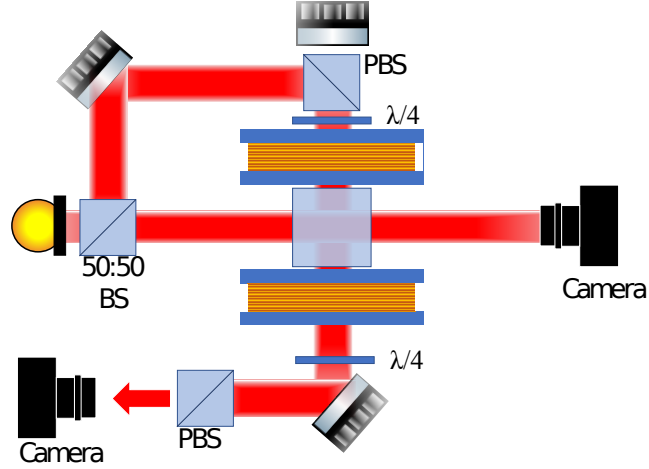
Figure 2.2: Diagram for the perpendicular camera setup. Here, BS is a beamsplitter, PBS is a polarizing beam splitter, and $\lambda/4$ is a quarter waveplate. The complexity of the setup is from space restrictions due to MOT optics and E-field coils. Circumventing this was done by making the probe beam perpendicular in polarization to the MOT beam and multiplexing and demultiplexing them via PBS.

Figures 2.3-2.5 show the analysis of the atomic cloud's position using the two-camera approach. Originally, the only camera view available was the one seen in figure 2.3 and no applied DC field was used (represented in column C of figure 2.3). At a glance, the cloud appears to be well aligned but column C of figure 2.4 highlights the need for both a second camera view as well as the need for shifting the cloud via a DC bias field. The full analysis is culminated in figure 2.5. Firstly, there appears to be a slight initial velocity perpendicular to gravity that causes the cloud to drift across the fiber's core which makes it difficult to judge loading quality using only the live image of the cloud (via fluorescence). The 2-camera absorption image analysis is also extremely useful as a feedback for adjusting parameters like the bias field. The other option would be to probe the absorption through the fiber while varying parameters (i.e. bias field), but this feedback is very binary in that the parameters need to be quite close to optimal in order to see any change. Without any change in the feedback, the only hope would be to randomly adjust parameters and hope to see something. With 2-camera absorption images, even settings which would yield no loading into the fiber (like column A in both fig. 2.3 & 2.4 which falls off the fiber in both axes) still gives useful information to guide how the parameters should change. This approach enabled the quick resolution to the parameter search both in terms of bias field
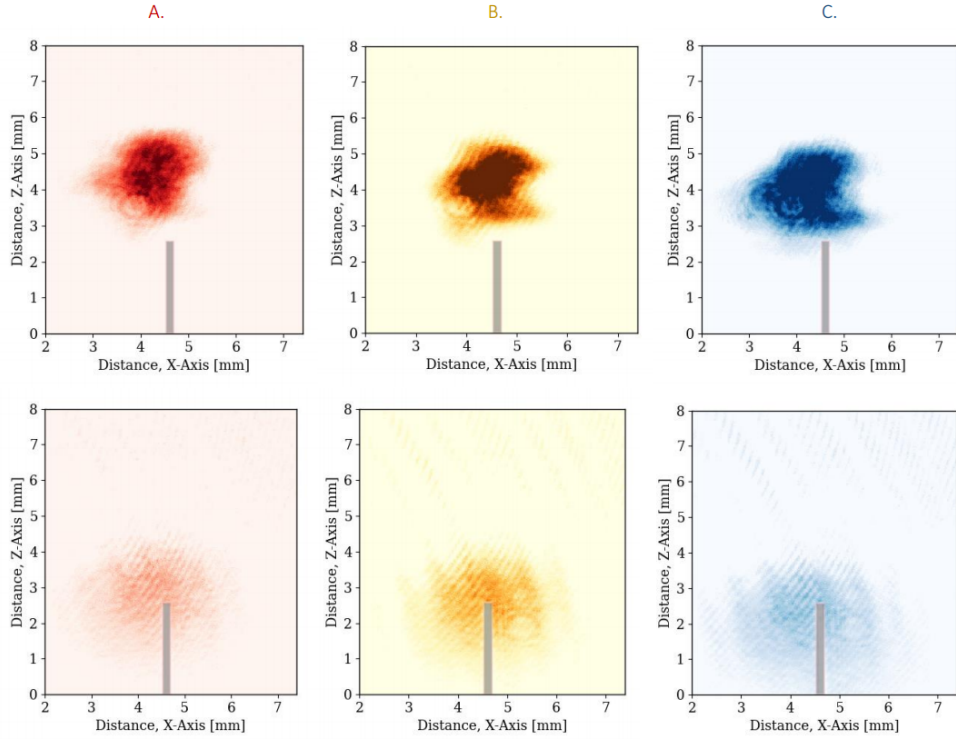
Figure 2.3: Absorption images of cesium cloud taken after 2 ms (top row) and 18 ms (bottom row). Columns A, B, C differ by an applied DC magnetic field which shifts the cloud in the axis of light propagation (towards camera). Column C has no applied field.

settings and in terms of how long it takes for the atoms to reach the fiber. Figure 2.6 shows the result of this optimization via near-resonant probing of atoms in the fiber at different delays with respect to the release of the atom cloud. It is clear from the plot that there is a sudden jump in absorption of the probe light at a long time after release that is only present when the attractive dipole beam is present. The feature can only occur if there are atoms loaded inside the fiber and from here, one can fine tune the settings to maximize the number of atoms loaded via more sensitive measurements beyond imaging.

The combination of atomic density, temperature, and position of the cloud should be sufficient to maximize the loading of atoms into the core. However, often greater atomic density leads to warming of the cloud and better cooling leads to ejection of faster atoms from the cloud. Thus, finding an optimal point between two competing values is nontrivial. This can be mitigated by instead looking at phase space density instead; a
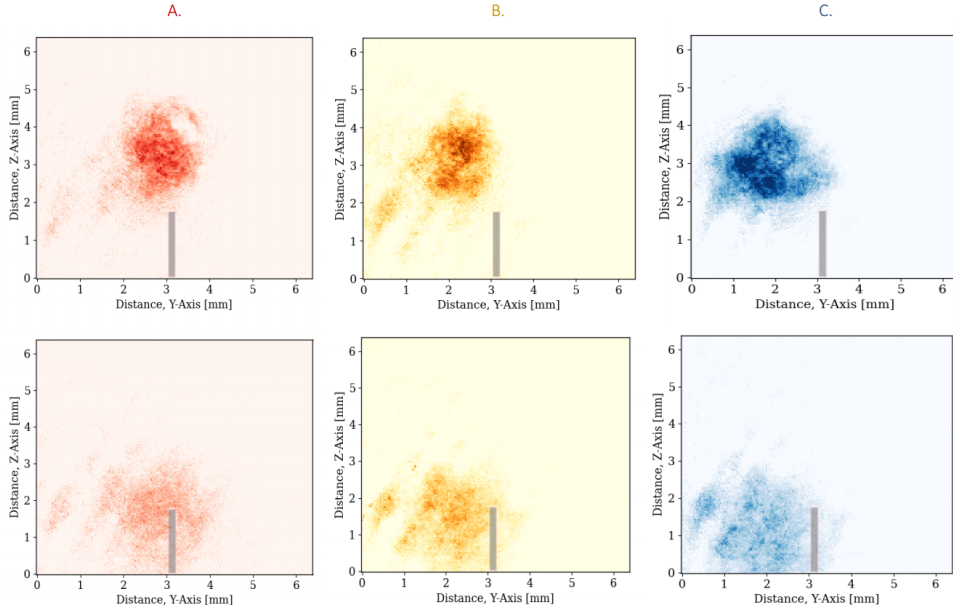
Figure 2.4: Absorption images of cesium cloud taken after 2 ms (top row) and 18 ms (bottom row). Columns A, B, C differ by an applied DC magnetic field which shifts the cloud in the axis perpendicular to light propagation (across camera view). Column C has no applied field.

measure which combines density and temperature in such a way for loading[1]. However, if it were possible to get a gauge of how many atoms inside the fiber with as close to a single-shot measurement as possible then this would be the best case scenario. Thankfully, there is such a measurement that can give use specifically the number of atoms using a single probe pulse sequence. This measurement is called optical bleaching.

2.2.4 Optical bleaching

The general concept of this measurement is to send a train of resonant pulses long enough that all the atoms are moved to a different ground state and the atomic ensemble becomes "bleached" [43]. More specifically, "resonant" must not be a cyclic/closed transition and the excited atoms need to be able to decay to two different ground states. One needs the

---

[1]Phase space density is a unitless value representing the number of atoms contained in a cube whose side lengths are the de Broglie wavelength, $\lambda_B = \frac{h}{p} \propto T^{-1}$. Thus, both a larger atomic density and colder temperatures lead to greater phase space density.
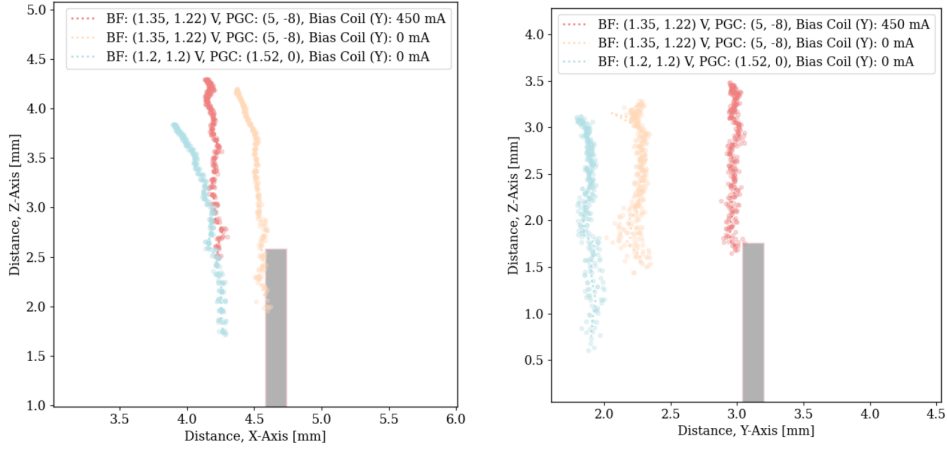
Figure 2.5: Plots of the position of the atomic cloud's centroid in Z (direction of gravity) as well as X (left) and Y (right) for the same applied DC field settings as the previous figures. The directions X and Y represent the views parallel and through the center of the anti-Helmholtz coils, respectively. The gray rectangle represents the hollow-core fiber.

atoms to be moved into a dark state with enough excitations from the pulse train. The key aspect of this measurement is that the number of excitations needed to move the atom to the other ground state must be known and preferably low. For cesium, As shown in figure 2.7, the transition of choice is $|F = 4\rangle$ to $|F' = 4\rangle$. With a branching ratio of 5/11, each atom will scatter just over two photons before moving to the dark $|F = 3\rangle$ state. Once there, the atom will be transparent to any other photons in the pulse train. This means that if one examines a histogram of the pulse train after attempting to load atoms, there will be a portion of some pulses missing due to scattering. Knowing the branching ratio enables us to essentially "count" the number of missing photons to count the number of atoms (see figure 2.7). There are a couple of advantages to this measurement. First, it is fundamentally a single-shot measurement, with only a single pulse train needed to get a result on the number of atoms loaded. Second, with a sufficiently long pulse train, one can see the photon count for pulses that move through the fiber without any scattering. This is very helpful from a purely technical point of view in that, in a single shot, one can get an atom number result and check probe coupling. Probe coupling is an important factor as low coupling will not give an accurate reading of the atom number and very low coupling can appear as more atoms being loaded. It also allows measuring the transverse temperature of the atoms inside the fiber.

The emphasis on the importance of a single-shot measurement may not be able to be
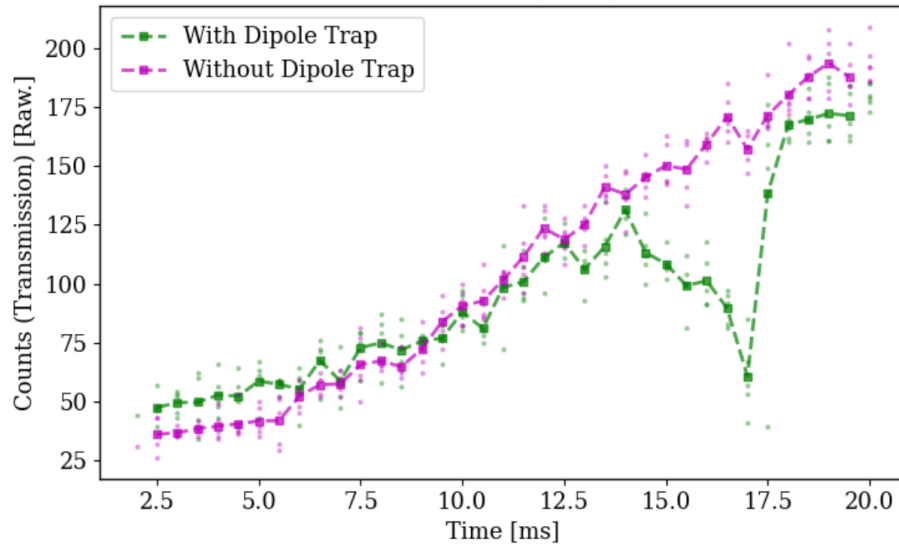
Figure 2.6: Transmission of a near-resonant probe coupled through the hollow-core fiber for different delay times after releasing the atomic cloud. The sudden drop in transmission which only occurs when the dipole beam is present indicates loading of atoms inside the core of the fiber.

fully expressed here. However, such a measurement opens the door to the use of machine learning to fine-tune every controllable parameter in the experiment (see chapter 4).
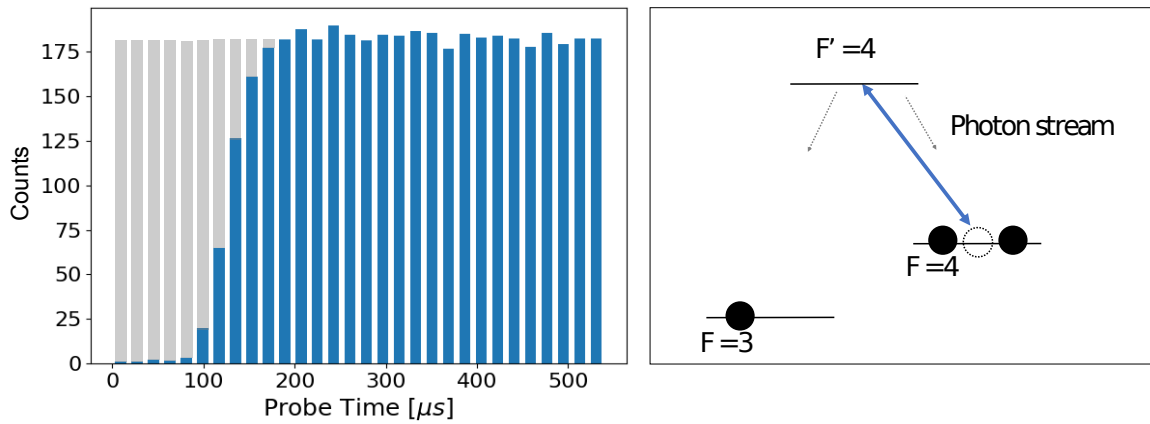
Figure 2.7: (left) A histogram of a train of resonant pulses travelling through the hollow-core fiber with atoms loaded (blue) and without (gray). The absence of counts in the blue histogram is due to atoms, loaded into the core of the fiber, scattering the photons. Counting the missing photons and taking into account the branching ratio will give the number of atoms loaded into the fiber's core. (right) Diagram for the hyperfine levels of interest for optical bleaching in cesium. By preparing our atoms in the $|F = 4\rangle$ ground state and illuminating the $|F = 4\rangle \rightarrow |F' = 4\rangle$ transition, each atom will scatter roughly two photons before moving to the $|F = 3\rangle$ ground state. Once here, the atom will no longer interact with the probe light.

Chapter 3

Dichroic atomic vapor laser lock (DAVLL)

3.1 Overview

For many of the experiments that we wish to perform, we need to be able to implement a cascade/ladder scheme (as illustrated in fig. 3.1) which requires a laser that is locked to a transition between two excited states. This cannot be done using the locking architecture that is typically used for lasers locked from a ground state. That is simply because there is no population in the upper transition and thus would show no spectroscopic signal when scanning such a laser through a vapor cell. Thus, a laser locked from a populated ground state to the intermediate excited state of interest is necessary to pump the atoms and allow a spectroscopic signal to be visible. From here, one could proceed with the traditional architecture of locking to a peak by modulating the laser's frequency. The necessity for this being that the error signal, which is needed for the feedback of any locking scheme, has to be linear or at least anti-symmetric about the lock point. Since a peak is symmetric about the lock point, modulating the laser frequency is done to effectively produce an electronic derivative of the spectroscopic signal which would give the anti-symmetry about the lock point. However, in this particular case where a pump laser is needed, there exists a locking method which directly produces a linear error signal; the method known as dichroic atomic vapor laser lock or DAVLL.

An outline for one of the DAVLL setups we employ is shown in figure 3.3 which is the same for all DAVLL setups other than the two lasers being used. The core principle behind this scheme which sets it apart from more traditional locking methods is the use
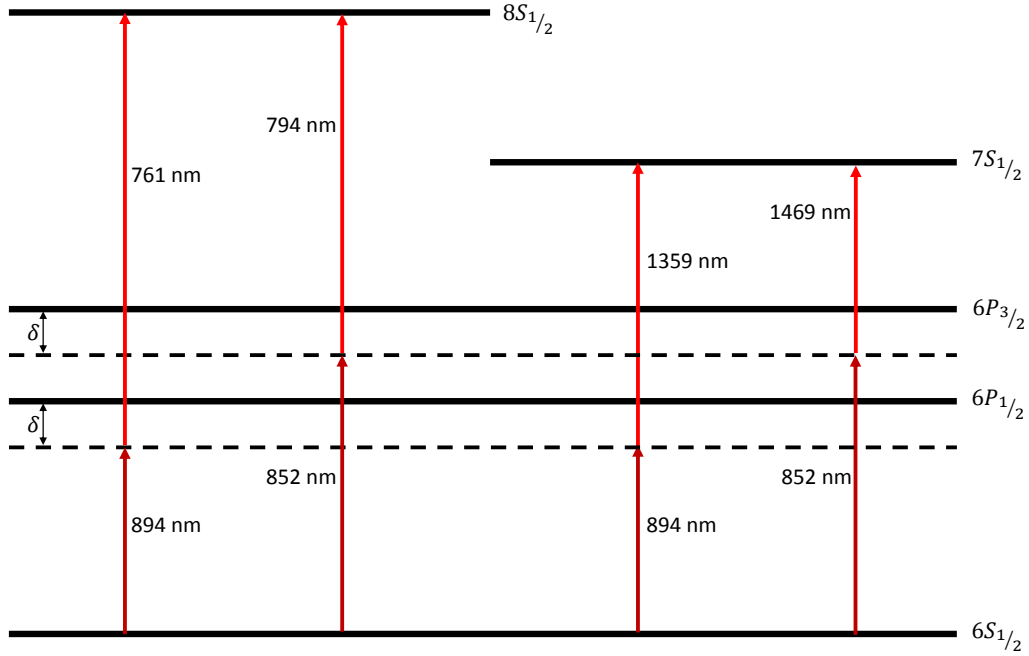
Figure 3.1: Level diagram illustrating four cascade schemes implemented in this project. Both 894 nm and 852 nm lasers are locked via an offset lock which allows for some detuning off of the intermediate state. The DAVLL scheme will lead to the upper laser (761/794/1359/1469 nm) being locked such that the two-photon resonance between the ground state and second excited state is complete.

of an external magnetic field across the vapor cell. The reason behind this is illustrated in figure 3.2. The external field lifts the degeneracy on the sublevels[1] of the intermediate such that a circularly-polarized probe beam will absorb at some detuning away from the $|m_F = 0\rangle$ sublevel. Although this does not complete the full explanation as it is not the probe that is scanning (it is already locked) but rather the meter on the upper transition. Thus, we must elucidate one more aspect of this setup: EIT. In a 3-level system, when both transitions are illuminated on resonance, interference between these two fields leads to a lack of absorption (a transparency window) instead of the maximal absorption seen in the 2-level case. This is important as when the meter beam is resonant with respect to $|m_F = \pm 1\rangle$, there will be absorption of the probe beam due to the EIT effect despite

---

[1]It is important to note that the magnetic field will lift the degeneracy of the sublevels for all three transitions, albeit by different amounts so that there is still an overall shift away from resonance.
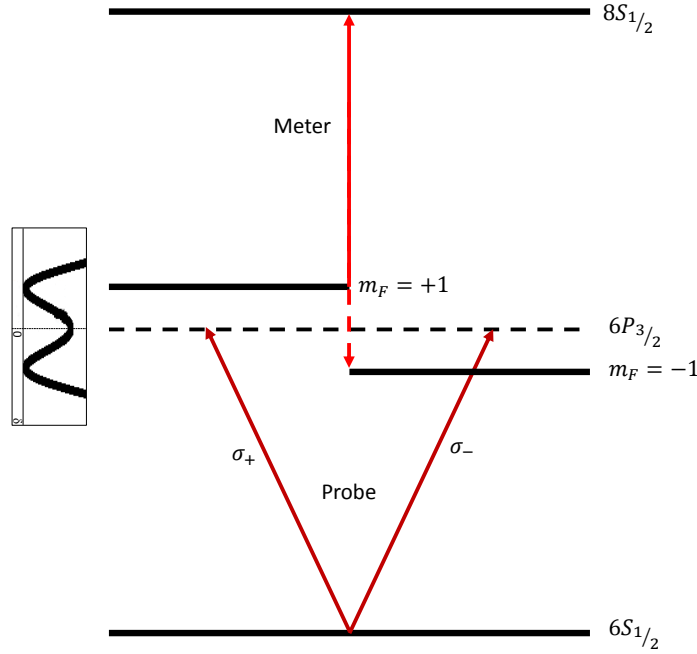
Figure 3.2: Level diagram for the DAVLL system. A linearly polarized probe beam locked to $|m_F = 0\rangle$ which can be decomposed into two beams of σ_+ and σ_- polarizations. When scanning the meter beam, there will be transmission minima when the meter is resonant with either $|m_F = -1\rangle$ or $|m_F = +1\rangle$. When the meter is resonant with the $|m_F = 0\rangle$ sublevel, there will be a transparency window for the probe beam.

the probe beam being resonant with $|m_F = 0\rangle$ and not $|m_F = \pm1\rangle$. This is depicted in figure 3.2 with the inset spectrum on the left-hand side showing two dips split by the EIT window.

3.2 Implementation

Returning to figure 3.3, if the probe laser (852 nm) is linearly polarized, then we can look at it as two beams of equal and opposite circular polarization. When this beam passes through the vapor cell surrounded by magnets while the meter beam's frequency is scanned, two absorption dips will be observed at two different frequencies of the meter. If the probe beam is split into its two circularly polarized constituents, one can invert one of the dips

into a peak which gives rise to a linear section in between with the frequency resonant with $|m_F = 0\rangle$ in the middle. This can be achieved with a polarizing beam splitter (PBS) and a matched photodiode pair whose photocurrents are subtracted from one another. This electronic signal from the matched photodiodes can be used directly as the error signal for locking the meter laser without the need for any modulation. Finally, one can use an additional vapor cell (as shown in fig. 3.3) and a simple photodiode to see the EIT transparency window. If the meter beam is locked as expected, the simple photodiode will show a voltage level at the same height as the peak of the window, indicating that it is locked at the two-photon resonance between the ground state and highest excited state. An example of the error signal and EIT peak can be seen in figure 3.4. One can see that the point when the error signal crosses zero between the two absorption features coincides with the peak of the EIT signal. An additional aspect to this locking approach is that the transparency window appears when the two fields form a two-photon resonance from ground state to the second excited state, even if they are not resonant with the intermediate transition and instead form a virtual transition. What this means is that if the probe beam is detuned away from resonance of the intermediate state, the error signal will lock the meter beam at an equal but opposite detuning about the intermediate state. If one uses an offset lock for the probe, then one has the ability to lock the meter to arbitrary offsets as well which gives much greater flexibility for cascade experiments.

The best way to verify the quality of locking that this DAVLL scheme produces is to simply observe the EIT signal uses our cold atom setup. Given the cold atoms narrow linewidth, we can observe the stability of the lock on the MHz scale.

3.3 Analysis

As shown in figure 3.5, it can be seen that the transparency window moves with the offset of the locked 794 nm laser as intended. To check the quality of the lock's center frequency, multiple datasets are fitted using the derived susceptibility for this system to ascertain what detuning of the meter beam is actually observed (see figure 3.6 for examples of fits). A simple plot of the observed shift as a function of set frequency is shown in figure 3.7. From this plot, it can be seen that there is an almost completely consistent offset of +2 MHz. This is most likely due to a small offset in the acousto-optic modulator (AOM) used as a shutter for the meter laser going into the cold atom setup. Outside of this, it appears that the lock works exceptionally well as, even if the offset is never fixed, a consistent offset is far easier to compensate experimentally than a drift.

However, it is important to note that an unexpected result occurred during scans where

the meter is locked near the resonance of $\left|6\mathrm{P}_{3/2}, m_F = 0\right\rangle$. While a peak is expected around where the meter is locked (to complete the two photon absorption) instead there are two peaks around the resonance as if the initial peak is being split. This phenomenon is examined in more detail in chapter 6.
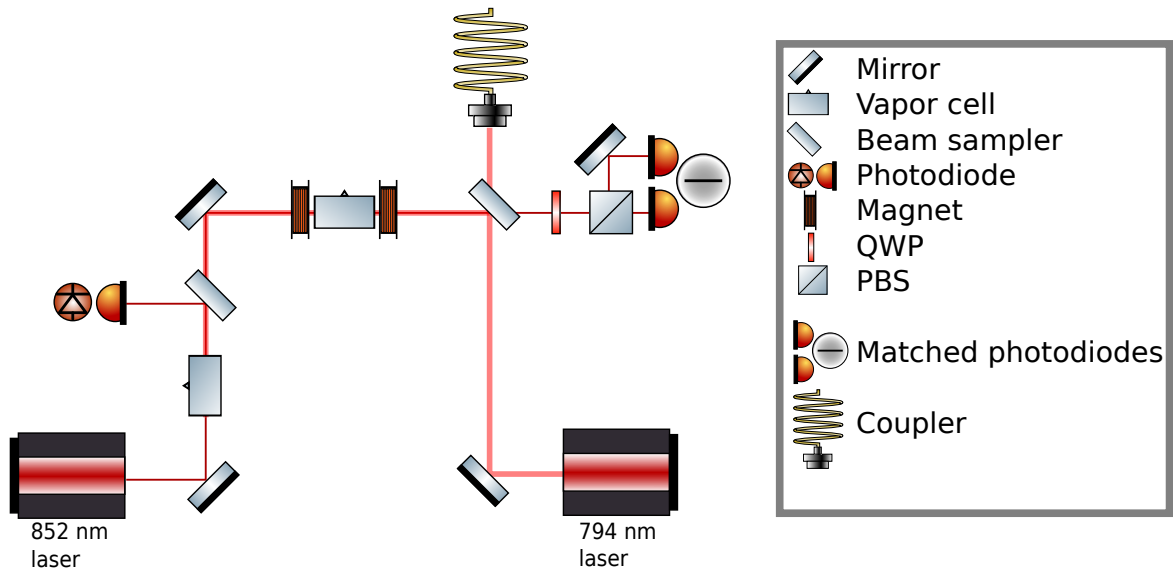
Figure 3.3: Setup for the DAVLL lock. The setup involves two counter-propagating lasers typically named meter (794 nm) and probe (852 nm) overlapped and passing through a vapor cell that has an external magnetic field. The probe is linearly polarized which is equivalent to having two beams with equal and oppposite circular polarization. two absorption peaks will be seen when scanning the meter beam across the shifted Zeeman sublevels while the probe beam is locked to the $|m_F = 0\rangle$. If we separate the two circular polarizations using a quarter waveplate (QWP) and a polarizing beam splitter (PBS) and collect each beam on one of two matched photodiodes. The signal from these photodiodes are subtracted from each other leading to a dip and a peak across the scan with a linear transition in between them crossing zero as the meter becomes resonant with the $|m_F = 0\rangle$ sublevel of the intermediate level. An additional vapor cell with a beam sampler to send some of the probe exiting this cell to a photodiode will show the EIT peak whose signal can confirm whether the meter is locked successfully.
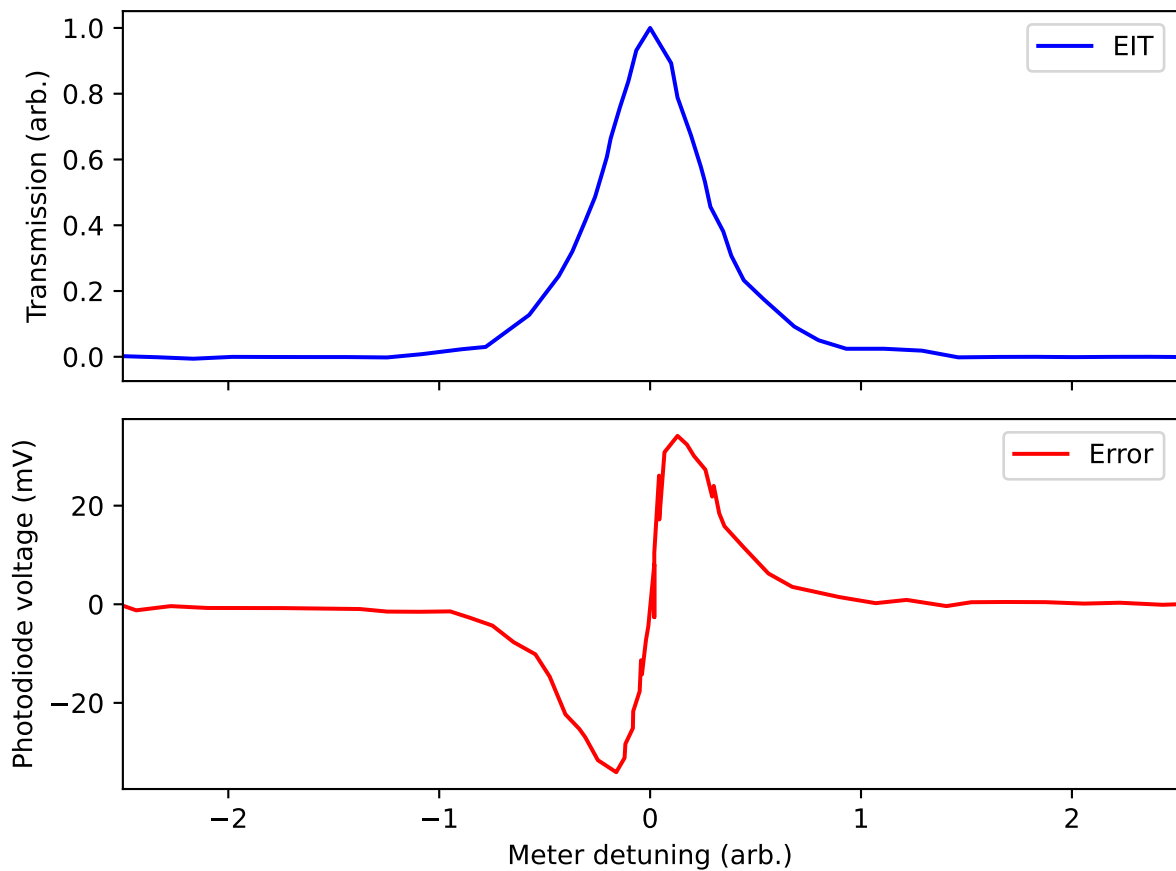
Figure 3.4: Example signals seen on the matched photodiode pair (Error) as well as the single photodiode (EIT) as shown in the DAVLL setup. The probe beam is locked on resonance with the intermediate state and the meter beam is scanned which results in the observed signals. The linear transition between the dip and peak of the error signal can be used as feedback to lock the meter beam. When the error signal is zero between the dip and peak, the meter will be locked such that the probe will sit at the top of the EIT peak.
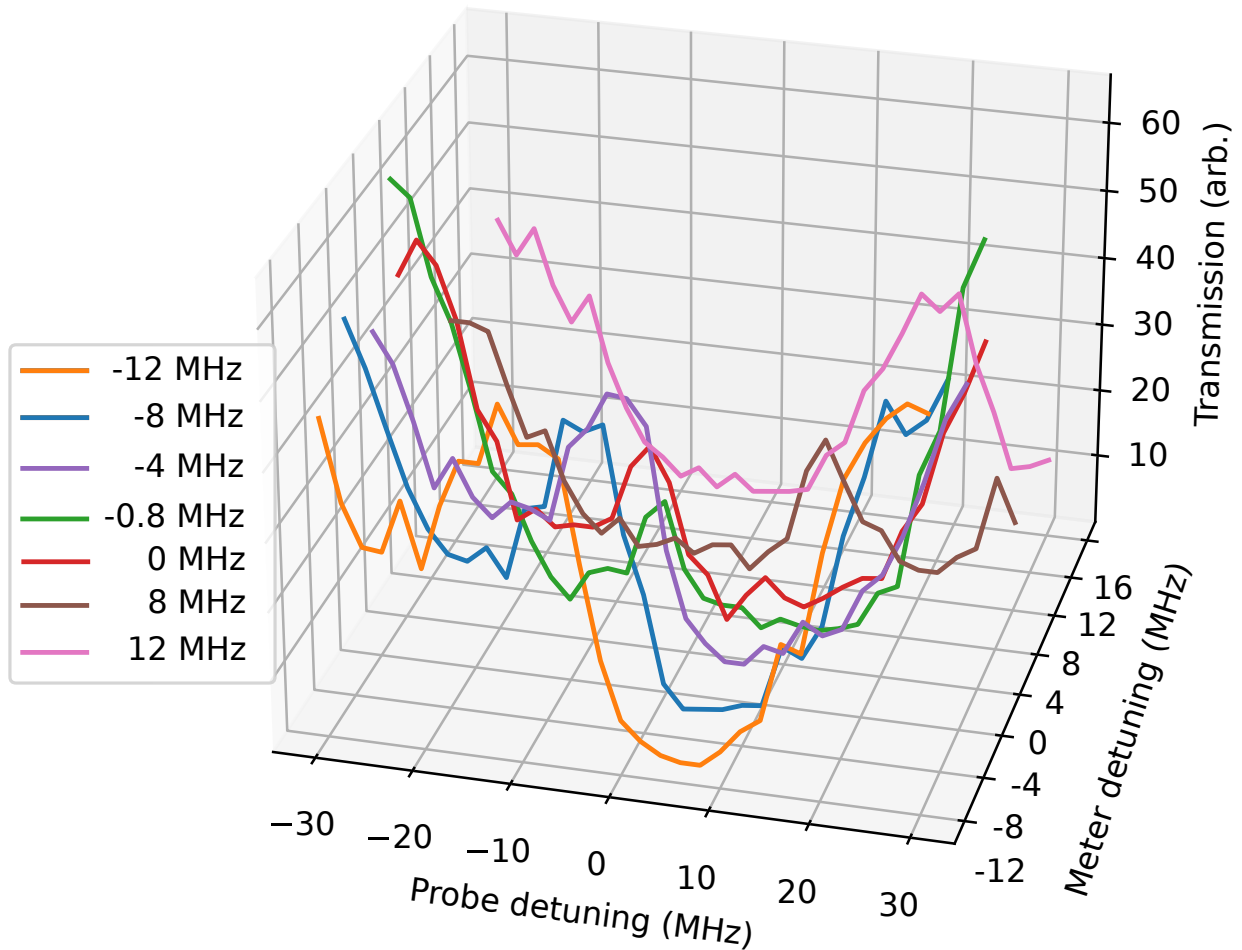
Figure 3.5: Frequency scans of a probe (852 nm) beam sent through a hollow-core photonic crystal fiber loaded with cold cesium atoms along with a copropagating 794 nm that was locked at different offsets using the DAVLL scheme. By using a probe beam that is different from the one used to lock the 794 nm laser, one can verify whether the lock is working as intended. It can be seen that the transparency window moves in frequency as the meter is locked at differing offsets.
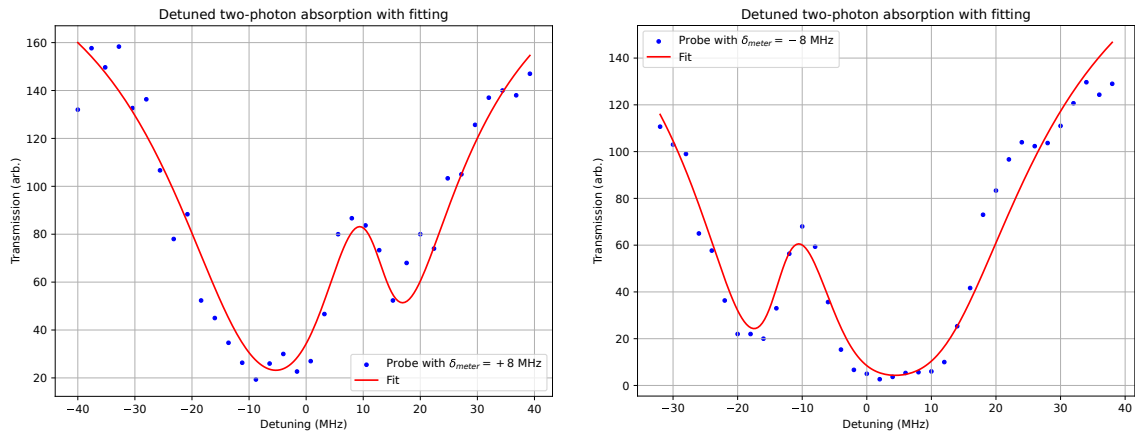
Figure 3.6: Examples of the fitting using the susceptibility derived in this chapter. By fitting multiple datasets with known values of power and detuning, one can narrow down other fitting parameters like optical depth and coherences.
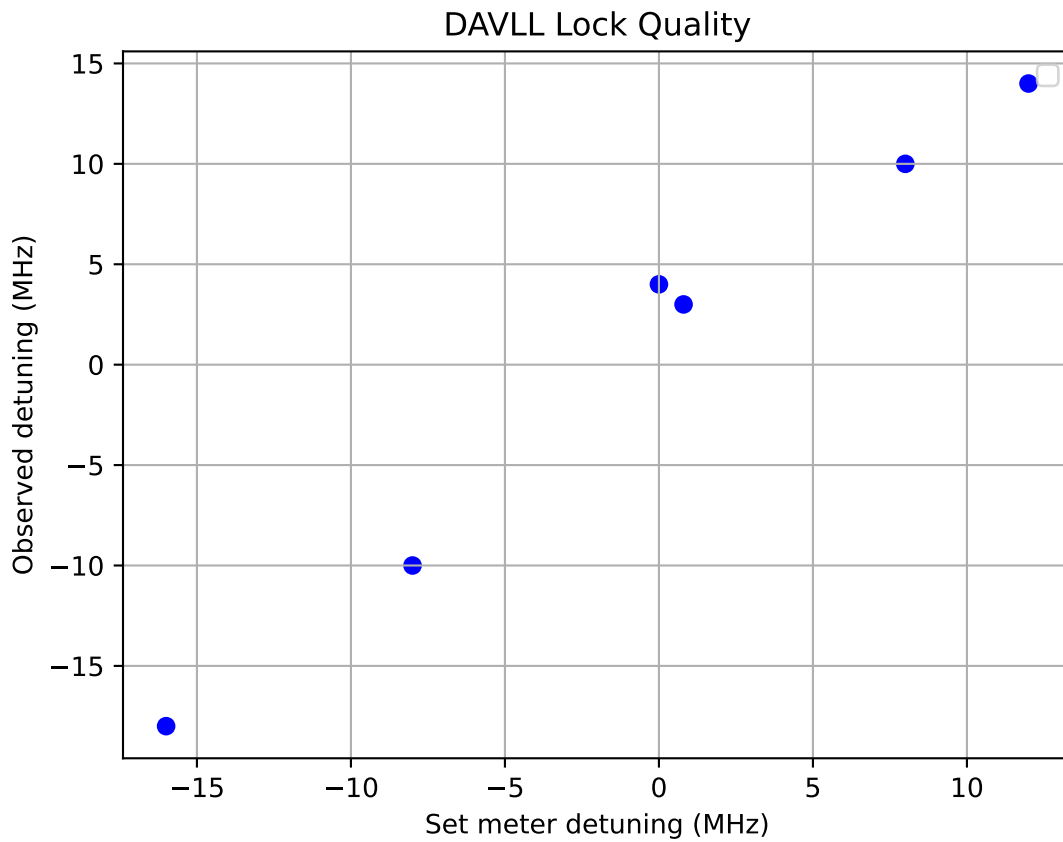
Figure 3.7: Plot of Observed detuning (measured via fitting) versus intended detuning set using the DAVLL system. Outside of the anomalous points close to resonance, there is a constant offset of +2 MHz for every set detuning.

Chapter 4

Loading atoms into fiber using machine learning

Loading cold atoms into the core of the HCPCF is a process that can be explained in a relatively simplistic manner, but it is a much more complex procedure in practice. Overall, it is achieved by preparing an atom cloud over the fiber and using gravity and an attractive red-detuned beam to funnel atoms into the core. However, preparing the cloud such that a maximal number of atoms load into the fiber's core requires optimizing multiple experimental parameters. Unfortunately, it is not as simple as maximizing the amount of atoms initially in the cloud before release. Atoms that successfully enter the fiber's core must be sufficiently cold and over the fiber in order to have such a trajectory. This requires multiple steps which include the initial creation of the optical molasses centered over the fiber, additional cooling below the Doppler limit via polarization gradient cooling (PGC), and funneling of the released cloud with the red-detuned dipole beam. Each step depends on various settings such as the intensity and detuning of the corresponding lasers, magnetic field intensities, and duration of each step. Altogether, this can form a parameter space whose dimensionality can easily exceed double digits. Given the intricate dependencies between several parameters, optimizing them is not as simple as scanning them individually. An intriguing solution to this otherwise complicated problem came from a couple of recent papers in cold atom physics, both of which use a software now known as M-LOOP. In the first paper, Hush et al. compare the performance of machine learning online optimization (MLOO), a precursor to M-LOOP by the same author, with the Nelder-Mead optimizer in the context of optimizing parameters for the production of a Bose-Einstein condensate (BEC) [44]. The study involves complex parameterization with 16 parameters, and the results demonstrate that MLOO achieves faster convergence than Nelder-Mead [44]. The

machine learning algorithm quickly identifies important parameters related to the production of BEC. The authors explore the impact of the number of particles in the learner on estimation accuracy and present a case where MLOO successfully eliminates an irrelevant parameter from the optimization process. Bentine et al. highlight the value of machine learning in optimizing experimental parameters with multiple dependencies in their paper [45]. They compare the convergence rates of three optimization methods and, notably, optimize all cooling stages in a quantum gas experiment simultaneously, achieving increased atom numbers in a Bose-Einstein condensate (BEC). The use of Gaussian Process (GP) regression helps identify sensitive settings within each cooling stage, enabling quick and efficient optimization within an hour [45]. The authors note the potential for counterintuitive optimal solutions and discuss the importance of stability in achieving consistent results. They conclude that GP regression is particularly beneficial in their experimental context due to its efficiency in handling a relatively small amount of training data compared to other methods like artificial neural networks [45]. Given the recent success of this software to optimize the complex process of Bose-Einstein condensate (BEC) formation, we have chosen to test it with our experimental setup.

Machine learning (ML) is a subfield of artificial intelligence (AI) that focuses on the development of algorithms and statistical models that enable computer systems to improve their performance on a specific task through experience and data, without being explicitly programmed. There are a few key factors of machine learning that need to be understood before discussing the results. First, a training phase must occur where data is collected for a set of parameters that are either randomly chosen, or selected using a simplistic triangulation method. This dataset is important as it is used to initially train the algorithmic model. Before discussing the potential models, we must address the concept of a cost function. The cost function measures the difference between the predicted values produced by the model and the actual target values. The goal of machine learning is to minimize this cost function, as a lower cost indicates better model performance. This is an important distinction as, for our case, there may be times when one wishes to maximize something (like atoms loaded in a fiber). For these instances, a creative cost function which inverts the result may be needed to adapt to existing ML models. The final factor is the model which is at the heart of the "learning" process. The goal is to find patterns in the data and formulate relations between the input parameters and the cost function.

4.1 Algorithmic models

4.1.1 Gaussian Process

GPs are a form of non-parametric probabilistic modeling. Rather than assuming a specific functional form for the relationship between input and output variables (i.e. linear regression), GPs model the entire distribution over possible functions that could describe the data. To illustrate this concept further, imagine you have a dataset of input-output pairs. A GP does not try to fit a single curve or line through these points. Instead, it considers many possible curves or functions, each corresponding to a different draw from the distribution over functions. These functions collectively represent the uncertainty about the true underlying relationship in the data.

GPs do not just give you a single prediction value but provide a predictive distribution over possible output values for a given input. This predictive distribution accounts for the entire range of possible functions, which is a key aspect of modeling uncertainty in Gaussian-process-based predictions.

4.1.2 Neural network

Another model often used in machine learning is a neural network. A neural network is a computational model inspired by the human brain's structure and functioning. Composed of interconnected nodes organized in layers, neural networks learn to map input data to output predictions through iterative adjustments of connection weights. The first layer receives and passes the raw input data to the subsequent layers. The number of nodes in this layer corresponds to the dimensionality of the input data. Intermediate layers, also known as hidden layers, transform the input data through a series of weighted connections and apply activation functions to introduce non-linearity into the model. The density of such layers is chosen typically based on the complexity of the system being learned. The output layer produces the final predictions for the raw data. The number of nodes in this layer depends on the specific task.

To make use of a neural network, one must train it. This is very similar to the methodology of machine learning in general. That is to say, a set of training data must be fed into the network and compared to the expected or target result. This is done via the aforementioned cost function. The error from output to expected is characterized by propagating this result backwards through the network where it can be compared to the original input.

This backpropagation enables one to adjust the weights of the inner layers to minimize the error.

4.1.3 Machine learning for atom loading

Both of the above models can be and have been used for machine learning in cold atom physics [44, 45]. While we will compare and contrast these models for our purposes of loading atoms into a fiber, both models are viable and can produce meaningful results in this field.

The major difference between these models is that neural networks are deterministic while GPs are fundamentally probabilistic. This distribution of probable functions does give GPs the ability to characterize uncertainty in the input. This distributive nature also grants GPs a general insensitivity to local minima. Having multiple possible functions can also help optimization using smaller datasets as there is greater flexibility in the choice of landscape. These perks are not usually had in the deterministic neural network as improper training, or not enough training, can lead to being stuck in local minima or not even converging to an answer. However, with proper training, neural networks are advantageous in their scalability with the parameter space. Computationally, GPs scale cubically with the parameter space whereas neural networks scale linearly [46]. Depending on the nature of the setup to be optimized, the computationally intensive GP may not be attractive. Thus, the choice of model truly depends on which drawbacks are more difficult to deal with. For us, the ability to characterize uncertainty and avoid local minima led to the choice of GP for the remainder of this chapter.

4.2 M-LOOP

For our experiment, we utilized a pre-established program to implement machine learning on our parameters. The program M-LOOP is a Python-implemented interface which allows a user to utilize several machine-learning algorithms which, when fed experimental data, can optimize an experimental output based on any number of different experimental inputs [47]. The general workflow of using M-LOOP is illustrated in figure 4.1, but will be further expanded upon here. There are several ways one can choose to communicate with M-LOOP. It is designed to control experiments though python, however, communication can be done through exchange of text files between itself and whatever program is used to control one's experiment. From here, one can choose several details of the implementation
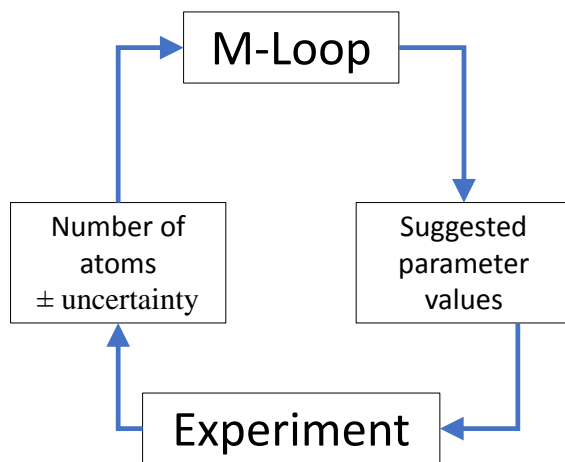
Figure 4.1: Workflow of M-LOOP. The implementation begins with initial parameters suggested by either the user or M-LOOP, then waits for an experiment to produce an output (cost function). This cost function is fed into M-LOOP which suggests new parameter values to either further train itself or guess a new input to give the best output.

like: the range of values each input can take, how many training points, the maximum time duration for a run as well as which algorithmic model to use (GP, neural network, etc.).

4.2.1 2-Dimensional test

Before a full test is done with the full parameter-space of our experiment, a test which could be verified manually must be done first to ensure M-LOOP is working as expected. Of course, there is a limit as to what non-trivial parameter scans can be done manually. Thus, a 2-dimensional scan of intensity and detuning of the light involved with the PGC stage of our experiment was performed. Polarization gradient cooling is an important step in the loading of atoms into the hollow-core fiber. There will be an optimal value which is a balance of temperature and the number of atoms which yields the largest number of

atoms inside the fiber's core. Additionally, there may be several combinations of intensity and detuning which give similar values as the two parameters can compensate for one another to a degree. This would mean there is a high likelihood of seeing local minima in this scan which stands as a good test for M-LOOP to navigate around. The results of the
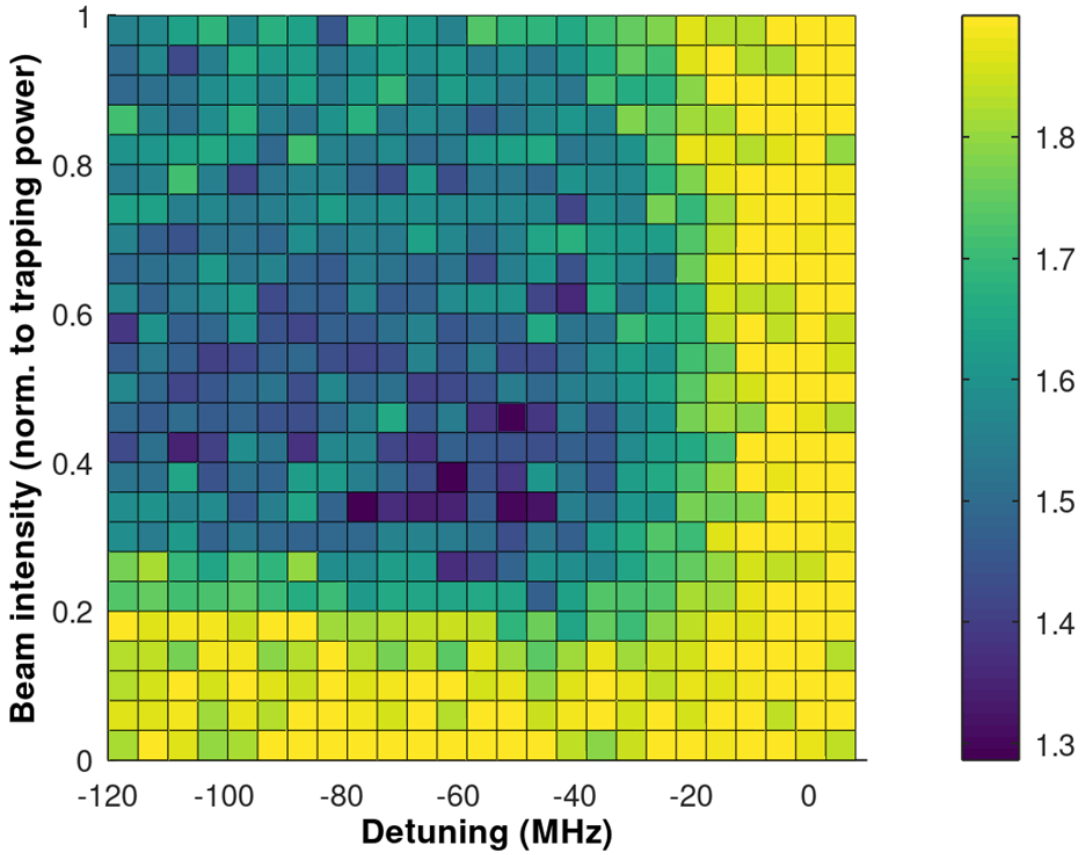
Figure 4.2: Manual scan of intensity and detuning for the polarization gradient cooling stage of the experiment. The colours correspond to the linear cost function, $2 - (N_a/1000)$, where N_a is the number of atoms loaded.

manual scan are shown in figure 4.2. The colours correspond to the linear cost function, $2 - (N_a/1000)$. One can see that the bottom and right edges of the plot show noticeably worse loading than the middle or top left. This makes sense as lower intensities (bottom) will have almost no cooling effect and lead to a faster expanding cloud while detunings close to resonance (right) will scatter more and heat up or disperse the cloud. Somewhere

in the middle lies what appears to be a few good loading parameters with a couple of local minima appearing of varying loading quality. Here, we can see how well the machine learning algorithm can avoid the local minima and find an optimal value.
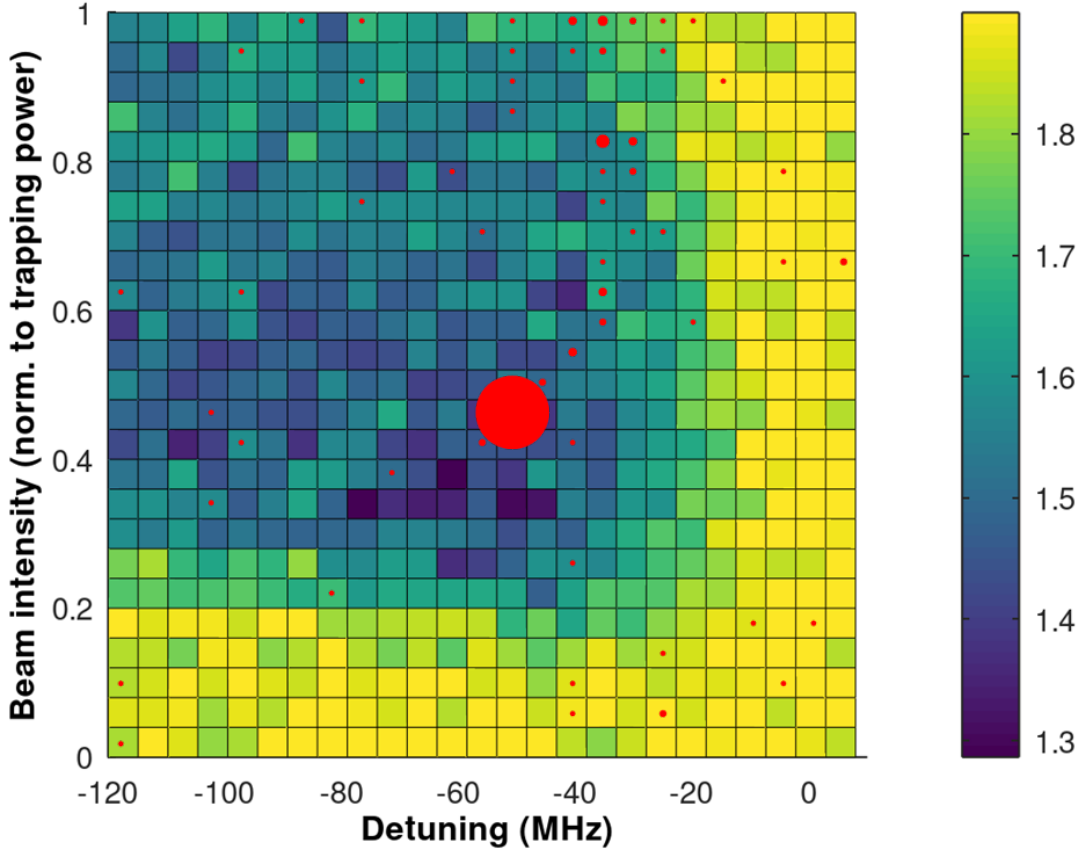
Figure 4.3: Results of machine learning overlapped with the manual scan of intensity and detuning for the polarization gradient cooling stage of the experiment. The size of the dot represents the number of times the algorithm queried the parameter. The colours correspond to the linear cost function, $2 - (N_a/1000)$, where N_a is the number of atoms loaded.

Figure 4.3 shows the result of a Gaussian-process-based machine learning scan of the same polarization-gradient cooling parameters that were tested manually (Fig. 4.2). As one can see, the algorithm visits a handful of parameters that lie along the edges of the

parameter space. From there, small steps are made (usually only changing one parameter) towards the center of the space. In the event that there is little change to the cost function (as is seen in the bottom and right edges) it appears that additional small increments are made to find meaningful change in the cost function. For larger changes to the cost function (such as the top or left edges), the algorithm takes bigger steps towards the center of the space. There are some points that are visited multiple times, however most are only visited once. The clear standout in this is the point ($\delta = -54$ MHz, $P = 0.44P_{\text{cooling}}$) which is visited 15 times. The reason is a major argument to choose GP; the ability to ascertain uncertainty. By revisiting a potential minima, one can not only become resistant to anomalous results arising from experimental errors, but also calculate uncertainty across the different measurements. The repeated probing of this point is not consecutive, interspersed among these are either points gathered from another function in the Gaussian distribution or random training points. This can be really helpful in avoiding local minima while still learning about the experiment.

Ultimately, what matters most when using machine learning is not only to find the global minimum or maximum, but to do so on a much faster timescale than traversing the parameter space manually. The machine learning run from figure 4.3 exemplifies this as it finds the same minimum cost value that the manual scan has, however the manual scan needed to traverse all 625 points (25×25 grid) whereas the machine learning algorithm found it after a total of 128 runs (including rechecking the point to ensure it was not a blip). Several runs using machine learning were attempted using the same 2-dimensional parameter space detailed above and highlighted in figure 4.3. As mentioned above, this parameter space is formed from the polarization gradient cooling stage's intensity and detuning values which can greatly affect the loading quality into the fiber. The runs are divided into two groups: the first involved using the cost function, $2 - (N_a/1000)$, and the second group used the cost function, $100/N_a$; where N_a is the number of atoms loaded into the fiber's core. Since M-LOOP only minimizes cost functions, loading quality needs to be rewritten such that more atoms reduces the cost function. The major difference between these cost functions is that the first is linear with respect to N_a whereas the second is purely reciprocal. Simply computing the reciprocal of N_a is the most direct approach to converting loading quality into a proper cost function, however the cost function will have a decreased sensitivity when the loading quality is poor. The linear cost function has the immediate problem that there is an assumed maximum attainable value (in our case, this is 2000) which could lead to unexpected behaviour. However, its linearity means that all values of N_a below 2000 will have the same weight in the cost function. Thus, both cost functions will be investigated to see if either one demonstrates an faster convergence towards a global minimum. The initial results using these cost functions are shown in figures 4.4 and 4.5.

The plots have been filtered such that only the next improvement in the cost function is plotted with the run number it occurred at. In between two nonconsecutive runs will be cost values that are worse or equal to the current best result in the particular experiment. Both plots appear to rapidly improve in cost with diminished returns as more runs are performed. Several experiments from both plots approach roughly the same loading quality of 600-700 atoms loaded. The major difference visible across these two plots is that the reciprocal cost function experiment has a few runs which appear to be fortunate in finding a good region very early through training and managed to optimize to a minimum just over 1100 atoms, lower than any linear cost function run. Although these runs also start at a higher loading quality than any other run.
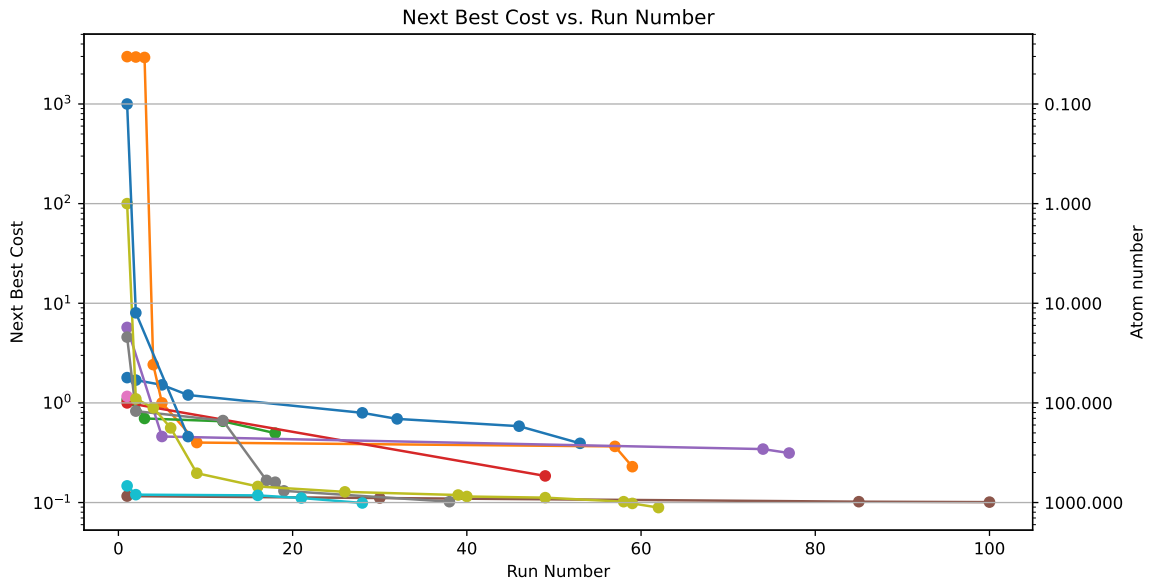
Figure 4.4: Machine learning optimization runs with polarization gradient cooling intensity and detuning as parameters. The cost function used is reciprocal (left vertical axis) and has the corresponding number of atoms loaded in the fiber on the right vertical axis. The different datasets are identical except for the starting point of the ML process.

The choice of polarization gradient cooling parameters as the initial test bed for machine learning in our experiment was made as it was a nontrivial example whose optimization served as the inspiration for attempting machine learning. While this is true, this particular parameter space may be a poor choice as there are many minima in the dataset (seen in
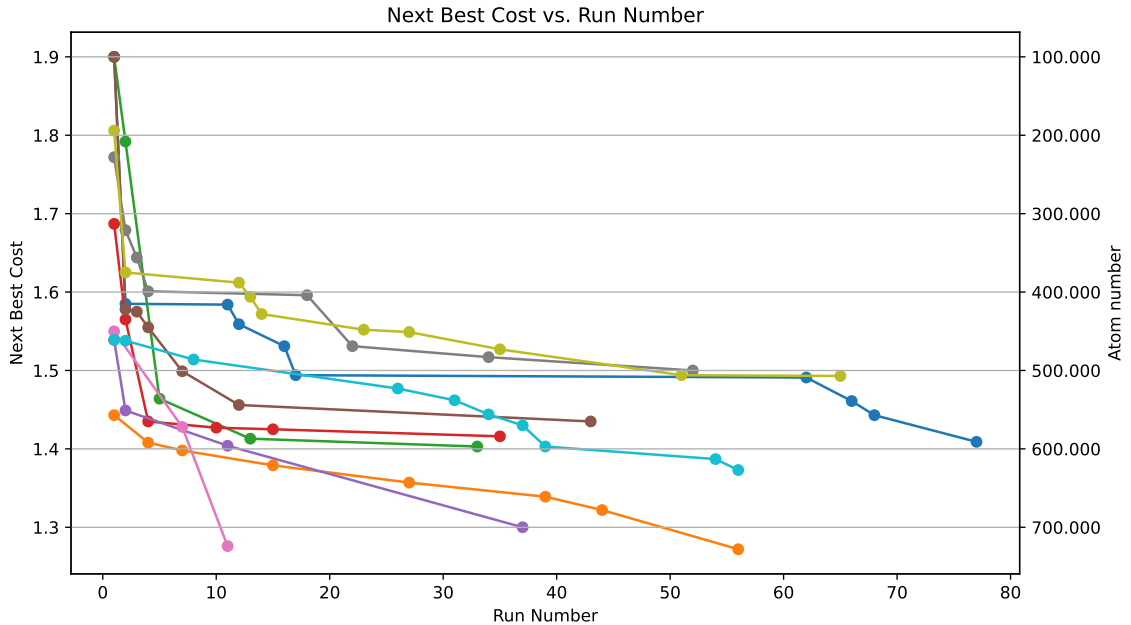
Figure 4.5: Machine learning optimization runs with polarization gradient cooling intensity and detuning as parameters. The cost function used is linear (left vertical axis) and has the corresponding number of atoms loaded in the fiber on the right vertical axis. The different datasets are identical except for the starting point of the ML process.

figures 4.2 & 4.3) that are very close in loading quality. To truly judge which cost function approach (linear versus reciprocal) performs better, a fake dataset with well known values, multiple local minima, but a single global minima would be best to use before real data from an experiment with uncertainties is used.

An attempt at running machine learning for a significantly larger parameter space was done and tabulated in figure 4.6. The parameters, PGC duration, time between cloud release and probing, PGC detuning, PGC intensity, initial trapping beam intensity, initial trapping beam detuning, repumper detuning, magnetic field gradient intensity, and magnetic field bias strength were varied via machine learning using the reciprocal cost function as its feedback. The results show an improvement on the overall number of atoms loaded at about 3000 compared the best results from only adjusting the PGC parameters. However, this result is not as good as the best loading previously done in this lab at around 10,000 atoms. Ultimately the thought is that, while 175 runs is almost twice as much as the
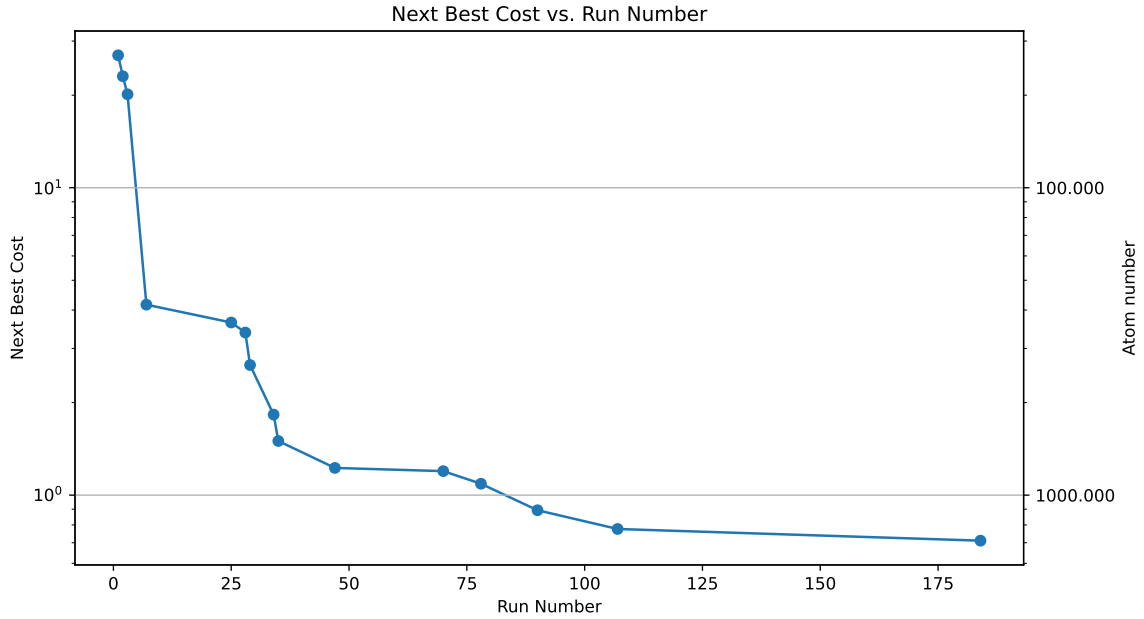
Figure 4.6: Machine learning optimization attempt with 9 parameters using a reciprocal cost function. The corresponding number of atoms loaded in the fiber is detailed on the right vertical axis.

runs in figure 4.4, it is most likely not enough for a parameter space as large as this one and it would be best if this optimization could be run for significantly longer. Unfortunately, our system is not stable enough to allow for long, unsupervised, runs and efforts are being made to improve the robustness of the setup.

Chapter 5

Loading efficiency versus dipole trap wavelength

When loading atoms into the core of the fiber, a red-detuned dipole beam is employed to greatly enhance the loading efficiency. Laser-cooled atoms present advantages such as minimal Doppler broadening and the prevention of atom-wall collisions by confining the atoms within a waveguide using an optical dipole trap. However, the dipole trap light induces an AC Stark shift in the confined atoms, altering the central frequency of optical transitions and introducing inhomogeneous broadening. These effects depend on the dipole trap power and the radial distribution of atoms in the fiber [48]. To address this, one can use a wavelength that imparts identical Stark shifts to both the ground and excited levels that form the interested transition; such a wavelength is commonly referred to as the magic wavelength. Alternatively, the dipole trap intensity can be modulated at a frequency of approximately 1 MHz [49, 50]. Atom probing occurs when the trapping light is off, and the trap is reactivated to prevent collisions with walls and atom loss. While this strategy mitigates ac Stark shift effects, the time window for probing atoms without inhomogeneous broadening is now constrained by the transverse temperature of atoms and the fiber core diameter. Transverse cooling, as proposed and observed in [51], or opting for a fiber with a larger-diameter hollow core (especially if the experiment doesn't require maximizing the interaction probability between a single atom and a single photon) could potentially extend the probing window.

Before delving further into the musings mentioned above, one should go over why one needs to go to such trouble when using optical dipole traps. Increasing the intensity of the dipole trap will directly increase the trap depth, however, it may not be as simple as making it as strong of a force as possible. Let us first look at how to characterize the

strength of the dipole beam in terms of atom loading. An atom illuminated by a laser is equivalent to a dipole immersed in an electric field:

$$\vec{p} = \alpha \vec{E} \tag{5.1}$$

Which can lead to the formula for the interaction potential of said dipole due to the driving field $\vec{E}$:

$$U_{dip} = -\frac{1}{2}\langle \alpha \vec{E} \rangle \tag{5.2}$$

From [52], we can rewrite U_{dip} in a more conspicuous form,

$$U_{dip} = -\frac{3\pi c^2}{2\omega_0^3}\left(\frac{\gamma}{\omega_0 - \omega} + \frac{\gamma}{\omega_0 + \omega}\right)I(r) \tag{5.3}$$

Which simplifies, using the rotating wave approximation, to:

$$U_{dip} = \frac{3\pi c^2}{2\omega_0^3}\left(\frac{\gamma}{\delta}\right)I(r) \tag{5.4}$$

Where c is the speed of light, ω_0 and γ are the transition frequency and linewidth of the atom, and $\delta = \omega_0 - \omega$ is the detuning of the dipole beam from the transition. From here, it is clear that both a more intense beam or a more resonant beam will give a deeper trap potential. In principle, these would give better loading efficiency. However, there are two important things to note before delving further. Firstly, moving closer to resonance increases the trap depth, but it will also increase the scattering rate. As per [52], the scattering rate for the light beam is,

$$\hbar \Gamma_{sc} = \frac{3\pi c^2}{2\omega_0^3}\left(\frac{\gamma}{\delta}\right)^2 I(r) \tag{5.5}$$

which increases at a faster rate than the trap depth. Since a greater scattering rate will cause warming of the atoms and potential scattering into a dark state. Thankfully, the converse being that one can move far off from resonance and the trap depth will not degrade as quickly as the scattering rate. The second issue that arises is the notion that a strong enough beam brings with it non negligible AC stark shift.

5.1 AC Stark shift

The AC Stark effect, also known as the Stark shift or dynamic Stark effect, is a phenomenon in atomic physics that describes the shift in energy levels of an atom due to the presence

of an external oscillating electric field, such as that from a laser beam. We can examine this by analyzing the population dynamics of a two level atom illuminated by laser light. For light whose intensity is characterized by Rabi frequency, Ω and detuning from the transition, δ, the populations of the ground state and excited state can be described as [26]

$$\dot{\tilde{c}}_2(t) = i\delta\tilde{c}_2(t) + i\Omega c_1(t) \tag{5.6}$$

$$\dot{c}_1(t) = i\Omega^*\tilde{c}_2(t) \tag{5.7}$$

As we are discussing a largely detuned light beam, we can assume that there is negligible excitation and take $c_1(t) = 1$ which simplifies eq. (5.6) to

$$\dot{\tilde{c}}_2(t) = i\delta\tilde{c}_2(t) + i\Omega \implies \tilde{c}_2(t) \quad = -\frac{\Omega}{\delta}\left(1 - e^{i\delta t}\right) \tag{5.8}$$

Given the oscillating component of eq. (5.8) is at the rate of the large detuning, δ, we can average it out and consider only the slower dynamics. Moving back from our earlier assumption of $c_1(t) = 1$ and taking $\tilde{c}_2(t) = -\frac{\Omega}{\delta}c_1(t)$ and putting it into eq. (5.7) gives

$$c_1(t) \approx c_1(0)e^{-i|\Omega|^2 t/\delta} \tag{5.9}$$

Here, we can see the ground state population varies with $|\Omega|^2 t/\delta$, acting as an energy shift of that amplitude. This shift is the aforementioned AC Stark shift.

5.2   Magic wavelength

One way of mitigating the Stark shift is to select a dipole trap wavelength that is detuned in such a way that the AC Stark shift for both the ground and excited state is the same. This would be equivalent to not having a shift at all from the perspective of probing the atom. Such a wavelength is often called the magic wavelength. Before delving further into this, it is important to note two factors. First, there may not exist, strictly speaking, a true magic wavelength where the net light shift of a transition (ground and excited levels) is zero. Often, the wavelength which imparts the smallest light shift is denoted as the magic wavelength. second, this calculation is done for a particular ground and excited state; a magic wavelength found for one transition may not be as insensitive for another transition. Despite this, it is still incredibly valuable as atom trapping experiments complexify. We can begin by noting the equation for the shift for a state $|F, M_F\rangle$ due to a laser of frequency,

ω, and intensity, I from [53]:

$$\hbar\Delta_{AC} = \frac{3\pi I c^2}{2} \sum_{F',M_F} \frac{A_{j'J}}{\omega_{FF'}^3} \left(\frac{1}{\omega_{FF'}+\omega} - \frac{1}{\omega_{FF'}-\omega} \right) (2F+1)(2F'+1)(2J'+1)\dots$$

$$\dots \begin{pmatrix} F' & 1 & F \\ M_{F'} & 0 & -M_F \end{pmatrix}_{(3-J)}^2 \begin{Bmatrix} J & J' & 1 \\ F' & F & I_n \end{Bmatrix}_{(6-J)}^2$$

(5.10)

Where summation is done over all dipole-allowed transitions. $\omega_{FF'}$ and $A_{j'J}$ is the frequency and Einstein coefficient (respectively) of the transition made between the level whose Stark shift is being calculated and the current level being summed over. The matrix terms are the Wigner 3J and 6J (as labelled) symbols which determine the transition strengths. To find the net Stark shift of a particular transition, one must calculate (5.10) for both levels. For our interests, we wish to investigate possible shifts for the $\left|6S_{1/2}, F = 4, m_F = 0\right\rangle \rightarrow \left|6P_{3/2}, F' = 5, m_F = 0\right\rangle$ transition. The Grotrian diagrams outlining the nearby possible transitions for each level of interest are shown in figures 5.1 and 5.2. Further information for several of the transitions is outlined in table 5.1. The hyperfine splitting from the center of gravity can be calculated with

$$W = \frac{1}{2}AK + B\frac{^3/_2 K(K+1) - 2I(I+1)J(J+1)}{4I(2I-1)J(2J-1)}$$

(5.11)

with

$$K = F(F+1) - I(I+1) - J(J+1)$$

(5.12)

Figure 5.3 shows the result of the Stark shift calculation for the $\left|6S_{1/2}, F = 4, m_F = 0\right\rangle$ and $\left|6P_{3/2}, F' = 5, m_F = 0\right\rangle$ states of cesium. The asymptotic regions correspond to allowed transitions for that state. There are a few pieces of information from Figure 5.3 that we use for experiments. The first would be considered the main goal of these plots which would be wavelengths with little to no net Stark shift across the two levels; such wavelengths being known as magic wavelengths. For this, there are a couple times where the two lines intersect which signifies a magic wavelength for this specific transition (e.g. 884 nm & 937 nm). The ultimate choice of 937 nm is due to the fact that: it is red detuned for both D lines (852 & 894 nm), and that the nonzero Stark shift in the vicinity around the intersect point is relatively shallow. The second point being important as any drift in the dipole trap frequency would not be detrimental as well as, given that the magic wavelength is slightly different for neighbouring hyperfine transitions and the D1 line, having minimal Stark shift for other transitions needed for more complicated experiments (e.g. pump and control beams on different hyperfine levels or the other D line).

Table 5.1: Hyperfine coupling constants and lifetimes of cesium levels

State	Frequency (THz)	A (MHz)	B (MHz)	T (ns)	Reference
$5D_{3/2}$	434.68	48.6	0.4	966	[54]
$5D_{5/2}$	437.60	-21.2	1	1351	[54]
$6P_{1/2}$	335.12	291.92	0.00	34.89	[42]
$6P_{3/2}$	351.73	50.28	-0.53	30.47	[42]
$6D_{3/2}$	677.19	16.36	-0.7	60.00	[55]
$6D_{5/2}$	678.48	-4.60	0.23	60.70	[56, 57]
$7S_{1/2}$	555.70	545.90	0.00	48.28	[58, 59, 60]
$7P_{1/2}$	652.57	94.40	0.00	165.21	[61, 62, 63]
$7P_{3/2}$	657.87	16.61	-0.19	137.54	[61, 62, 63]
$7D_{3/2}$	780.89	7.36	-0.1	89.10	[64]
$7D_{5/2}$	781.52	-1.81	1.01	89.10	[64]
$8S_{1/2}$	729.01	219.08	0.00	93.10	[65]
$8P_{1/2}$	770.73	42.93	0.00	376.00	[66]
$8P_{3/2}$	773.21	7.61	-0.01	320.00	[66]

5.3   Modulated dipole beam

In the event that the magic wavelength cannot be used, or a larger trap depth is required, one must move to a modulated beam in order to avoid the Stark shifts. Figure 5.4 shows an example of the pulse sequence for a optical depth measurement with a modulated dipole trap. The main desire is to avoid the Stark shifts induced by the strong dipole trap by having any probe or control beams interact with the atoms while the dipole beam is off. However, if the dipole beam is off for too long, the atoms will disperse within the fiber and collide with the walls of the fiber. With the the effect of Stark shifting minimized due to modulation, the choice of dipole trap wavelength is more flexible. However, there may be a limit to the choice of wavelength and power as one may be able to go arbitrarily close to a transition. It is possible some more complicated effects may occur as the wavelength approaches a transition. To test this, atom loading in the fiber will be probed for different wavelengths as a function of power.

First, let us examine how the loading efficiency is affected with increasing intensity for different wavelengths. Our experimental setup is the same as outlined in figure 1.8, with the dipole beam source being further outlined in figure 5.5. Modulation is achieved by sending a pulse sequence electronically to an AOM whose first order diffraction is used in the experiment. The Ti;Sapphire laser used can provide significant power ($\sim$ 50 mW
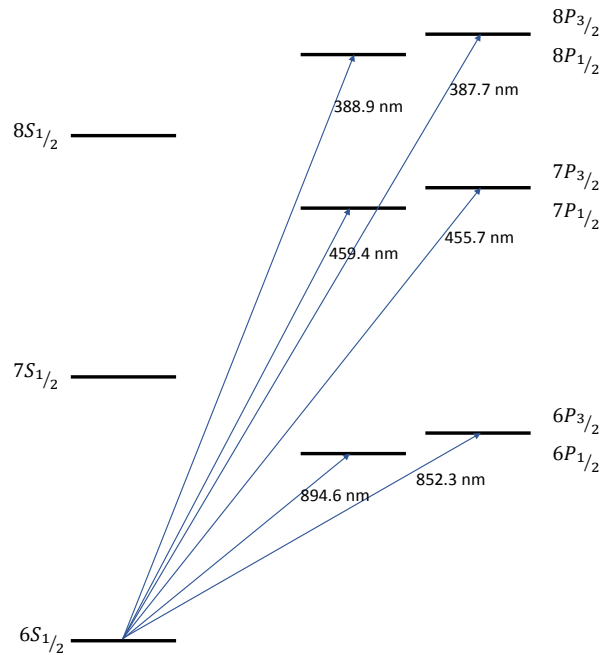
Figure 5.1: Grotrian diagram showing nearby possible transitions for the $\left|6S_{1/2}\right\rangle$ level with center of gravity wavelengths labelled for each transition.

coupled though hollow-core) at any red-detuned wavelength we desire. However, despite it providing the bulk of its power in the form of a narrow linewidth source centered around a chosen wavelength, there is still some small amount of light exiting the laser at nearby wavelengths. Spectrally, this appears as a sort of broadened "pedestal" surrounding the main emission. While it is small compared to the main emission peak, it is still significant
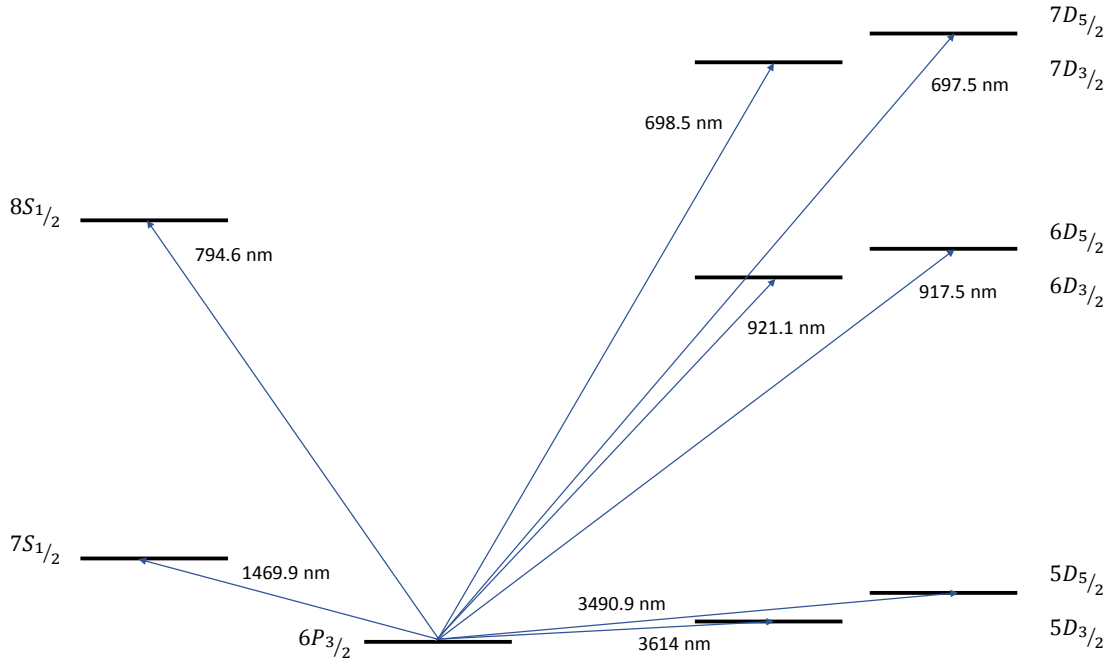
Figure 5.2: Grotrian diagram showing nearby possible transitions for the $\left|6P_{3/2}\right\rangle$ level with center of gravity wavelengths labelled for each transition.

if coupled into the experiment, e.g. by adding noise to signals collected with the single-photon detectors. Thus, we mitigate this in two possible ways of which both were tested. First, we employed a grating and a long enough path such that only a wavelength window of 1 nm is permitted through the fiber, as confirmed by a spectrometer. Additionally, we explored the use of a Semrock longpass filter which allows light beyond 900 nm to pass. Both options work exceptionally well to prevent any resonant (namely close to the D1 line at 894 nm) light entering the experiment, but the Semrock filter has an efficiency in excess of 90% compared to the meager 60% from the grating approach. This ultimately led us to choosing the Semrock filter moving forward.

While it is difficult to glean any key trends from figure 5.6, the general expectation is that the loading would trend heavily with trap depth, given that the wavelengths are far away from the nearest resonance (894 nm). If this were true, at any given power, the wavelength nearest to 894 nm would have better loading due to having a deeper trap depth. However, figure 5.6 shows multiple crossings which would imply that particular wavelengths may outperform other wavelengths despite having a smaller trap depth for

55
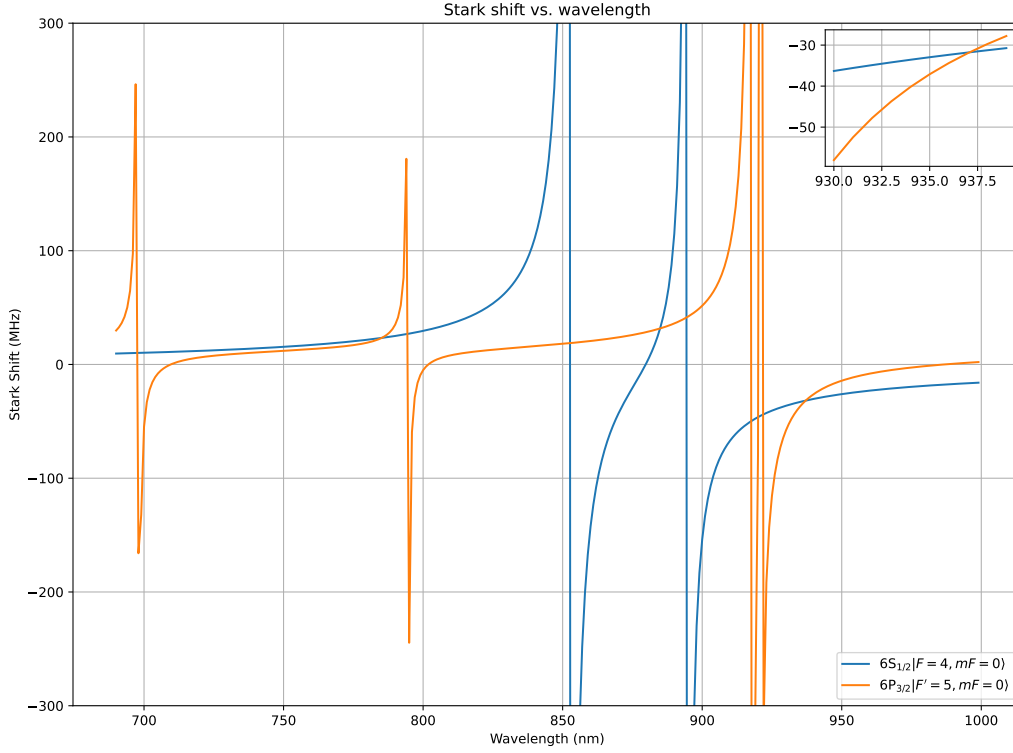
Figure 5.3: Plot of Stark shift for $\left|6S_{1/2}, F = 4, m_F = 0\right\rangle$ and $\left|6P_{3/2}, F' = 5, m_F = 0\right\rangle$ levels as a function of wavelength. The inset in the top right shows the region where the two plots intersect, which implies a net zero Stark shift or magic wavelength, at about 937 nm

the same power.

Thus, examining different wavelengths at equal trap depths for a few trap depth values would help to illuminate whether there is an optimal wavelength. This measurement will also be made by frequency scan of a probe beam to ensure there is not a problem with the bleaching measurement done in figure 5.6.

Figure 5.8 shows the results of frequency scans at different wavelengths whose power is adjusted such that equal trap depth is maintained (with Fig. 5.7 showing the raw data for the experiment). The measurement was performed at different trap depths to gather more data to ensure the correct trend is observed. The plots show that, for the majority

56
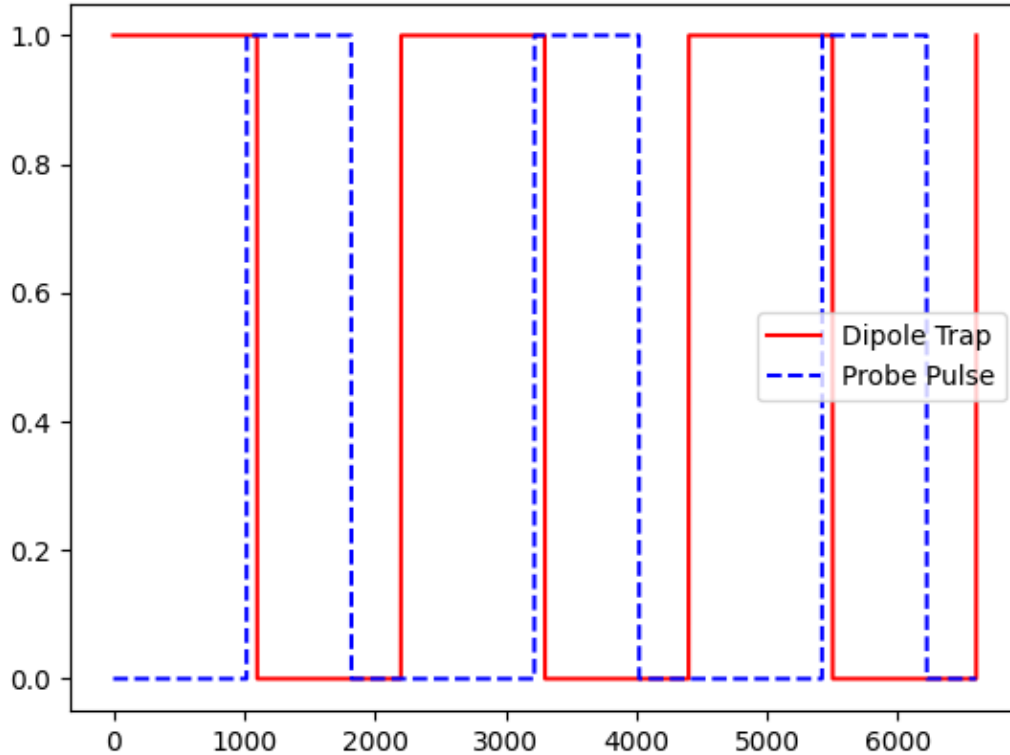
Figure 5.4: Example of modulation pulse sequence for a simple probe scanning experiment. The main goal is to probe the atoms while the dipole is off to prevent any Stark shift from interfering with experiments. These sequences are supplied to acousto-optic modulators to create the laser pulses. The slight overlap seen in the plot is to compensate for unequal delay in the optical path for each laser. The result is that, optically, the two sequences are out of phase with each other.

of wavelengths, atom loading is nearly identical when the trap depth is maintained. Due to the limitations of the titanium;sapphire laser's power output for longer wavelengths, larger trap depths could not be performed for the same wavelength range. While 925 nm appeared to be unusually effective in the lowest trap depth plot, the next plot shows it to have roughly the same loading quality as other wavelengths at equivalent trap depth.
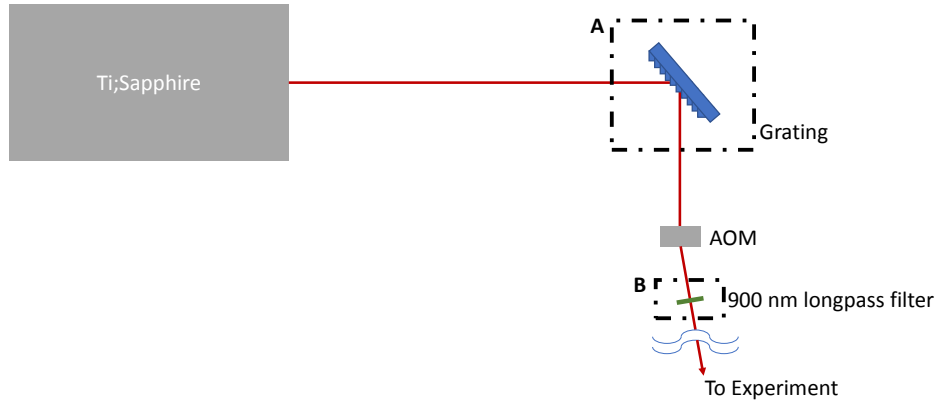
Figure 5.5: Simplified scheme for the generation of the modulated dipole beam. We employ a Ti;Sapphire broadband tunable laser which can provide a high power beam ranging from 700 nm to 1000 nm. An AOM is used as a fast shutter which enables modulation. Finally, to ensure that only the interested wavelength enters the experiment, both a grating (option A) and a Semrock longpass filter with cut-on wavelength of 900 nm were explored. These options are seen in dashed boxes as they are implemented separately.

The only wavelength which continually underperforms compared to other wavelengths is 905 nm. While there could be some photoionization effect such as what was seen with rubidium in [67], this effect was only seen for wavelengths much closer (sub nanometer) to a transition. 905 nm is over 10 nanometers away from the closest transition of $6S_{1/2} \rightarrow 6P_{1/2}$ at 894 nm. It is possible that there could be a coupling issue where a portion of the power may not have been coupled through the core of the fiber which means that an effectively lower power would be seen by the atoms loading into the core of the fiber. This is possible due to the length of the fiber being too short (2.5 cm) to fully attenuate multimode coupling. Alternatively, it is possible that the modulation did not work correctly for this wavelength leading to some partial Stark shift giving the appearance of a smaller number of atoms when probed. It is also important to note that figure 5.8 does not agree with
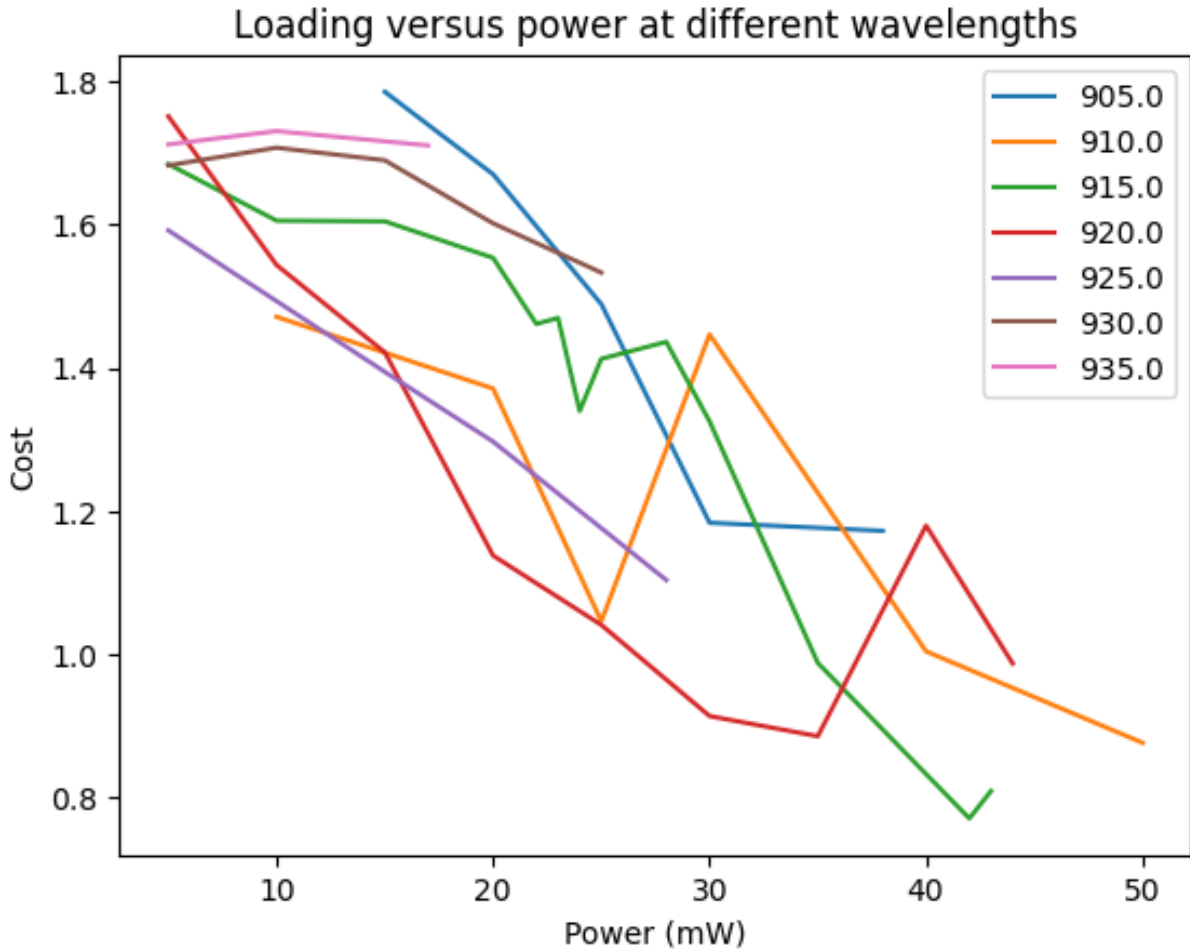
Figure 5.6: Loading quality vs dipole beam power for different wavelengths of the dipole beam. Here, the 'Cost' referred to by the Y-axis is the formula: $2 - (N_a/1000)$, where N_a is the number of atoms loaded. This cost function is used for the machine learning outlined in chapter 4.

figure 5.6 which showed multiple wavelengths outperforming their calculated trap depths. Thus, redoing this experiment while looking more closely at the possible problems that could cause either the bleaching measurement to incorrectly report the loading quality or any potential problems that could cause 905 nm light to perform poorly compared to its measured power.
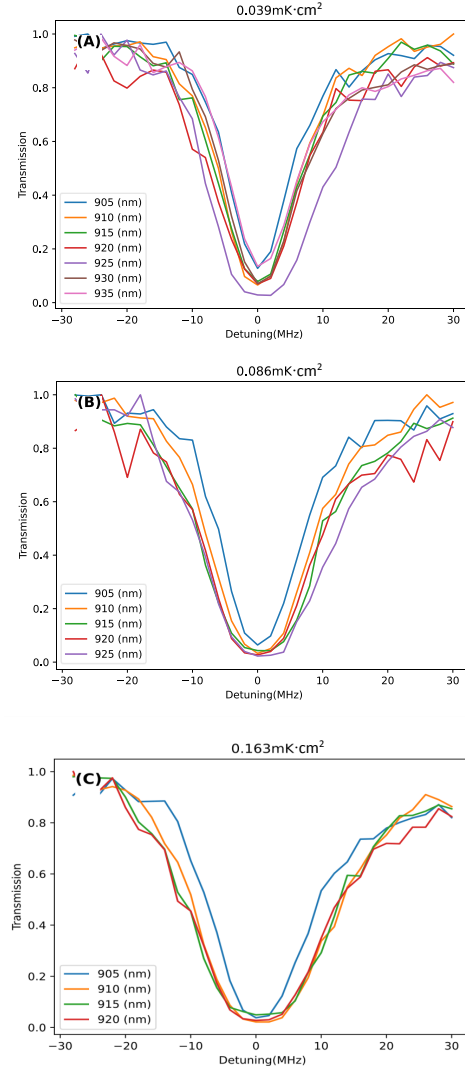
Figure 5.7: Optical depth of atoms loaded into the hollow-core fiber as a function of dipole beam wavelength. For each wavelength, the intensity was adjusted such that the trap depth was maintained at the specified values. Trap depths are written in units of $mK \cdot cm^2$ since the dipole beam diverges as it exits the fiber and so the trap depth would also be a function of distance from the fiber. Writing the trap depth as $mK \cdot cm^2$ removes this distance dependence for the sake of comparison.
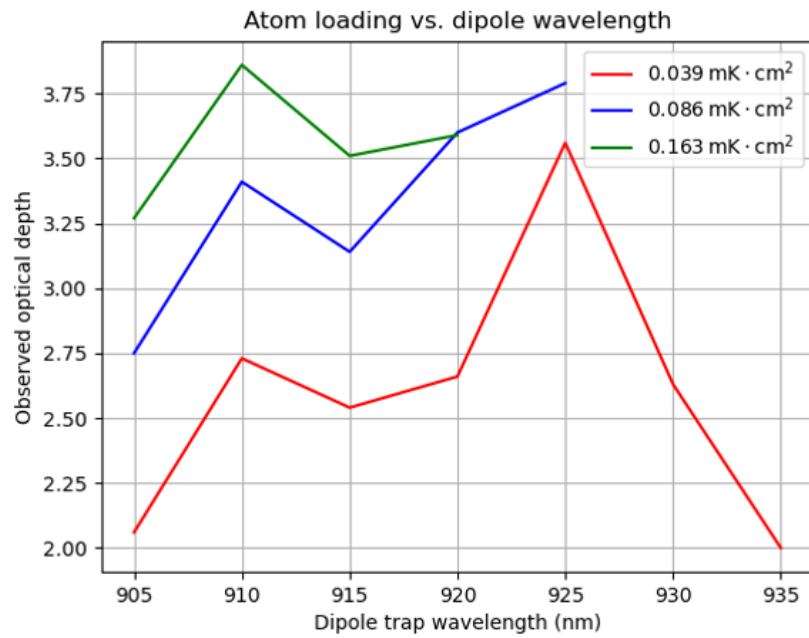
Figure 5.8: Summary plot for the raw data presented in Fig. 5.7

Chapter 6

Two-photon electromagnetically induced absorption

One of the main goals for this project is to realize wavelength conversion of single photons produced by a QD using cold atomic cesium. this would be a demonstration of a non-trivial or strong interaction between photons produced by a solid-state emitter and an atomic ensemble. In particular, previously reported demonstrations of such interfaces have been limited to slowing down the QD produced photons in warm atomic ensembles [68, 69, 70]. To do this, a four-wave mixing scheme will be utilized as illustrated in figure 6.1. The experiment involves illuminating one of the lower transitions ($\left|6S_{1/2}\right\rangle \rightarrow \left[\left|6P_{1/2}\right\rangle$ or $\left|6P_{3/2}\right\rangle\right]$) as well as the upper transition on the diagonal. In doing so, when a photon enters the atomic medium with a frequency close to the resonance of the unilluminated lower transition (for our purposes, this would be 894 nm) the result would be an emitted photon whose frequency aligns with the unilluminated upper transition (1470 nm for an input of 894 nm). The efficiency of this conversion depends on the choice of detunings for the various control beams and input photon as well as the number of atoms loaded into the core of our fiber (i.e. optical depth). Simulations of the conversion were performed by my colleague, Sai Sreesh Venuturumilli, and a summary of the results is outlined in figure 6.2. The plot simulates four-wave mixing for continuous wave fields entering an atomic cloud of a given optical depth and adjust parameters such as detuning and intensities of the control fields to maximize the efficiency of the conversion of 894 nm light into 1470 nm or 794 nm light; the percent efficiency is added to the plot accordingly. The Y-axis represents how far the 894 nm light can be detuned while efficiency is still maintained (the value of which is noted by the blue and red points). This graph shows some promising efficiencies if we can reach or surpass an optical depth of 100.
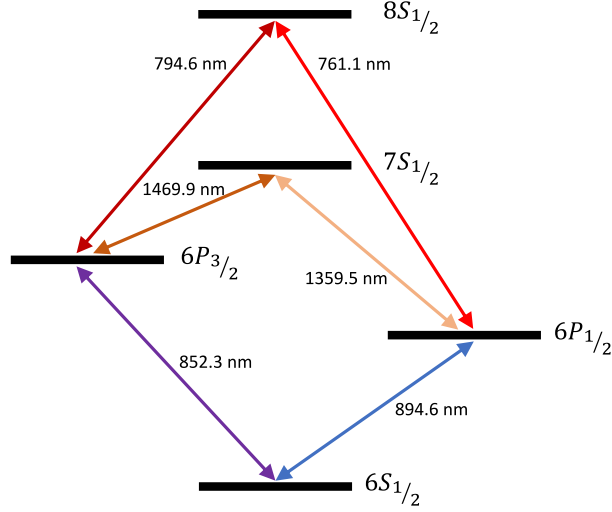
Figure 6.1: Level diagram of cesium that shows two possible diamond schemes to be used for wavelength conversion.

6.1   Two-photon absorption

Before we dive into a four-wave mixing experiment, we wish to implement a part of the diamond scheme, namely a cascade or ladder scheme. Such a scheme is highlighted in figure 6.3 and the particular wavelengths for the meter, Ω_m, and probe, Ω_p, fields used for this experiment are 794 nm and 852 nm, respectively. The additional benefit of exploring the ladder scheme is to investigate quantum memories with our setup. The results of this exploration are detailed in section 6.2. The choice of this particular ladder scheme is mostly made due to the lasers and quality of laser locking that we currently have in the lab. The goal is to observe the transparency that results when the detunings of the meter and probe are such that $\Delta_m + \Delta_p = 0$. We can view this theoretically through the density matrix approach.
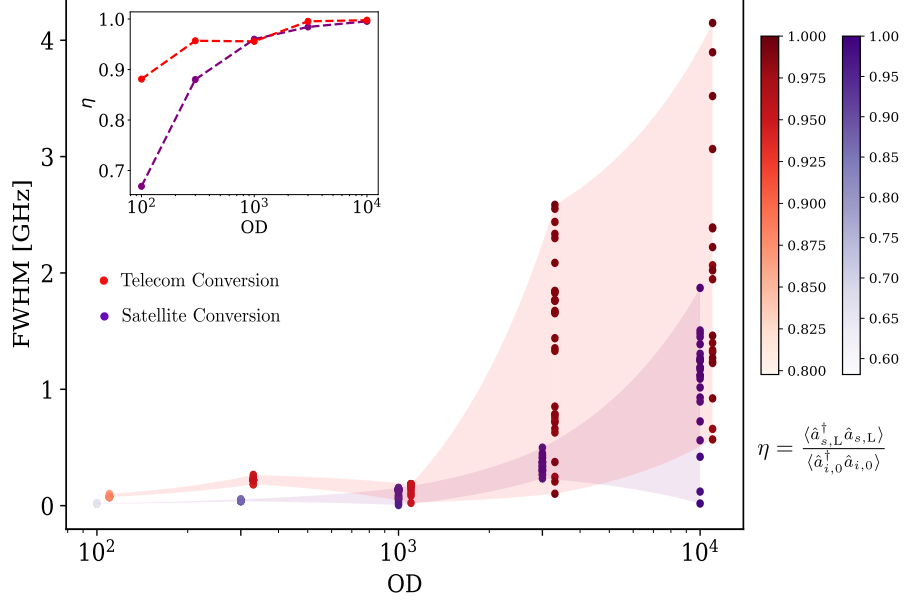
Figure 6.2: Conversion efficiency plot simulating the rate at which 894 nm continuous wave light certain bandwidth (y-axis) would be converted to 794 nm (blue - 'Satellite') or 1470 nm (red - 'Telecom') by means of a cold atomic cesium cloud with a certain optical depth (x-axis). Here, the 'bandwidth' is a measure of how far the 894 nm can be detuned while maintaining a high efficiency. Each point represents the maximum theorized conversion efficiency for a given bandwidth and an atom cloud of a given optical depth.

For a 3-level system, the optical Bloch equations can be written as (adapted from [71]:

$$
\begin{aligned}
\dot{\rho}_{11} &= -i\Omega_p\rho_{12} + \Omega_p^*\rho_{21} \\
\dot{\rho}_{31} &= -\left(\gamma_{13} - i(\Delta_p + \Delta_m)\right)\rho_{31} - i\Omega_p\rho_{32} + i\Omega_m^*\rho_{21} \\
\dot{\rho}_{22} &= \gamma_{13} - i\Omega_m\rho_{32} + i\Omega_m^*\rho{23} \\
\dot{\rho}_{21} &= -\left(\gamma_{12} - i\Delta_p\right)\rho_{21} + i\Omega_m\rho_{31} + i\Omega_p\left(\rho_{11} - \rho_{33}\right) \\
\dot{\rho}_{23} &= -\left(\gamma_{12} - i\Delta_m\right)\rho_{23} + i\Omega_p\rho_{13} + i\Omega_m\left(\rho_{22} - \rho_{33}\right) \\
\dot{\rho}_{33} &= 1 - \rho_{11} - \rho_{22}
\end{aligned}
\tag{6.1}
$$

This set of equations is typically solved numerically, but we can arrive at an analytical steadystate solution for this example if we make a couple of assumptions. First, we shall

take initial conditions of the atoms being entirely in the ground state. i.e.,

$$\rho_{11}(0) = 0$$
$$\rho_{22}(0) = \rho_{33}(0) = 0 \qquad (6.2)$$
$$\implies \rho_{32} = 0$$

These assumptions greatly simplify the equations in (6.1) to only two nontrivial relations:

$$- (\gamma_{12} - i\Delta_p) \rho_{21} + i\Omega_m \rho_{31} + i\Omega_p = 0$$
$$- (\gamma_{13} - i(\Delta_p + \Delta_m)) \rho_{31} + i\Omega_m^* \rho_{21} = 0 \qquad (6.3)$$

The above which are from $\dot{\rho}_{21} = 0$ and $\dot{\rho}_{31} = 0$, respectively. These can be used to get definitions for ρ_{31} and ρ_{21},

$$\rho_{31} = -\frac{\Omega_p \Omega_m^*}{\Gamma_{12}\Gamma_{13} + |\Omega_m|^2}$$
$$\rho_{21} = i\frac{\Gamma_{13}\Omega_p}{\Gamma_{12}\Gamma_{13} + |\Omega_m|^2} \qquad (6.4)$$

where $\Gamma_{12} = \gamma_{12} - i\Delta_p$, and $\Gamma_{13} = \gamma_{13} - i(\Delta_p + \Delta_m)$.

This allows us to write a formula for the probe susceptibility (from [71]),

$$\chi_p(\Delta_p, \Delta_m) = \left(\frac{N\mu_{12}^2}{\hbar\epsilon_0}\right) \frac{\rho_{21}}{\Omega_p}$$
$$= i\left(\frac{N\mu_{12}^2}{\hbar\epsilon_0}\right) \frac{\Gamma_{13}}{\Gamma_{12}\Gamma_{13} + |\Omega_m|^2} \qquad (6.5)$$

for the number of atoms, N, and the transition dipole moment, μ_{12}. When using this equation to fit experimental data, it is best to rewrite this to incorporate the common fitting parameter of optical depth which is:

$$OD = \frac{N\mu_{12}^2}{2\hbar\epsilon_0\gamma_{12}} \qquad (6.6)$$

This gives us a final form of susceptibility:

$$\chi_p(\Delta_p, \Delta_m) = iOD\frac{2\gamma_{13}\Gamma_{13}}{\Gamma_{12}\Gamma_{13} + |\Omega_m|^2} \qquad (6.7)$$
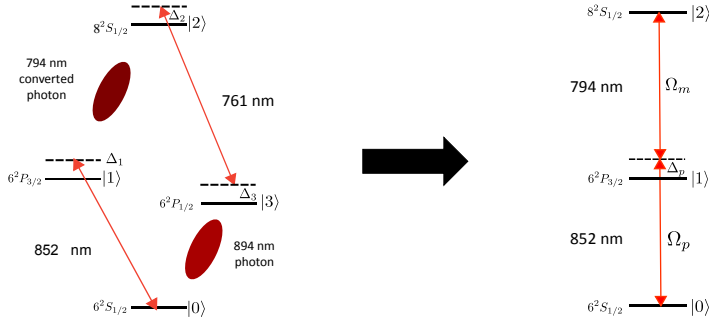
Figure 6.3: 4WM diamond scheme which takes an 894 nm photon emitted from the QD and converts it to a 794 nm photon via the cold atomic cesium. A preliminary test is to look at only one side of the diamond scheme in the form of a ladder scheme with 852 nm and 794 nm.

The data we measure in the lab is the intensity of the probe, so we must use the susceptibility equation (6.7) to get a formula for the probe's intensity. We can note that the electric field can be written using susceptibility as:

$$\mathcal{E}(z) = \mathcal{E}(0)e^{-(\text{Im}\{\chi\}+i\,\text{Re}\{\chi\})kz/2} \tag{6.8}$$

We can then arrive at an equation for intensity by noting that $I \propto |\mathcal{E}|^2$ which will lead to,

$$I(\Delta_p, \Delta_m) = I_0 e^{-\text{Im}\{\chi\}} \tag{6.9}$$

Here, we have collected any constants from the conversion of electric field to intensity, and the electric field amplitude, and incorporated them into I_0 as this is also a fitting parameter.

Now, let us examine the results of the experimental measurement of the two-photon absorption in the ladder scheme. The initial results are shown in figure 6.4. Here, the power of the meter field is maintained at approximately 1 μW inside the core of the fiber, but the detuning with respect to the $8S_{1/2}$ level is probed at a few different values. There is a clear and consistent movement of the transparency window as intended, but the position itself appears to be shifted towards higher than expected values. This is most noticable
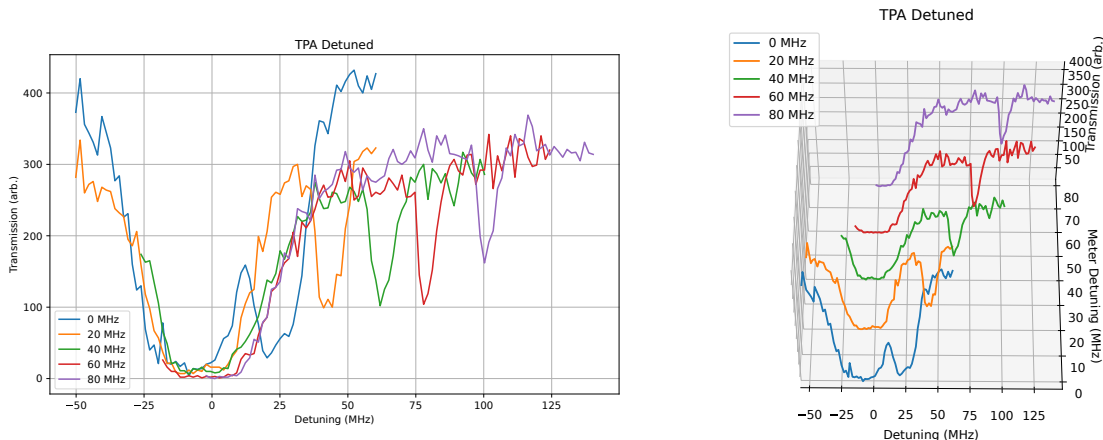
Figure 6.4: Preliminary data of two-photon absorption for the $6S_{1/2} \rightarrow 6P_{3/2} \rightarrow 8S_{1/2}$ ladder scheme in cold cesium atoms loaded into the hollow-core fiber.

in the resonant case as the window is clearly positioned to the right of resonance with the lower transition. A few possible reasons that could explain this shift are a stray magnetic field, offset in the AOM frequency, or an offset in the locking of the meter beam. The latter was investigated in chapter 3 and found to be about 2 MHz which does not fully account for the observed shift. Most likely, there is a combination of the above reasons that led to the overall shift seen.

Thus, we attempted to compensate for this offset but purposefully detuning the meter beam to see a peak at resonance. However, the result was unexpected.

Figure 6.5 shows the first attempt to compensate for the shift in the resonance seen in figure 6.4. It is clear that the compensation is not enough but moving to higher power in the meter beam revealed a splitting of the peak about zero probe detuning. Of course, high powers can very often lead to unexpected results. Therefore, it is necessary to probe this feature's dependence on the power of the meter beam more closely.

Figure 6.6 is the culmination of the meter beam power sweep mentioned previously. At lower powers, only one peak appears and its size seems to increase with meter power. This is as expected, however, the peak dissipates at about 600 nW inside the core of the fiber. Two peaks are then seen for meter powers of 700 nW and higher.

Works from other groups reporting multiple windows or peaks in a system with only one control field were reviewed in a search for an explanation of this phenomenon. Some papers describe multiple windows appearing due to atom interactions with cavities and
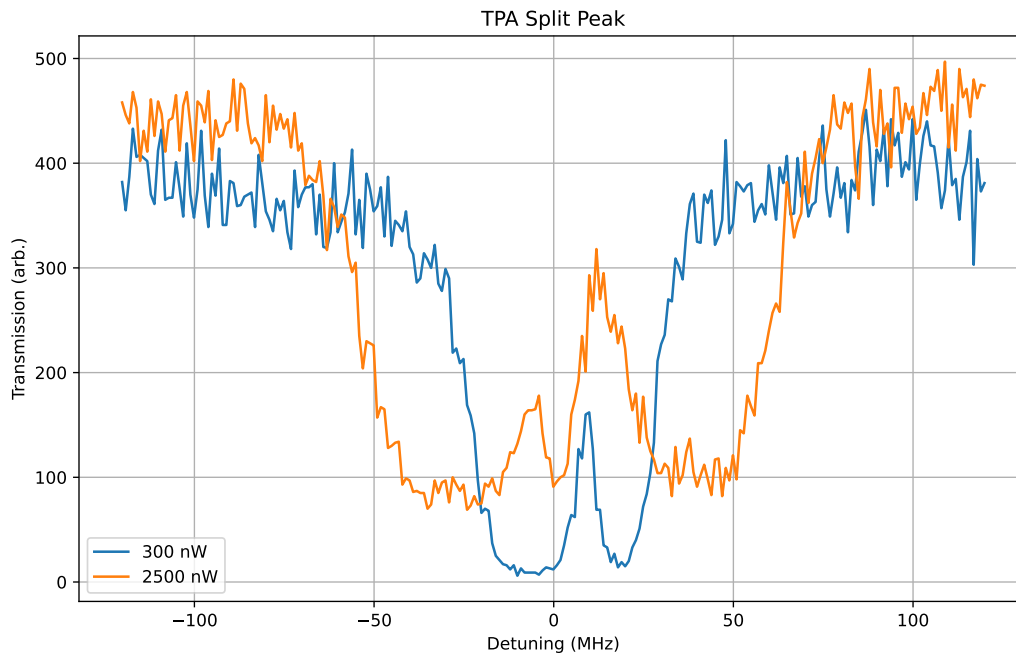
Figure 6.5: Preliminary data of two-photon absorption for the $6S_{1/2} \rightarrow 6P_{3/2} \rightarrow 8S_{1/2}$ ladder scheme in cold cesium atoms loaded into the hollow-core fiber. The meter beam is detuned in an attempt to compensate for an observed offset. The different lines are at different powers for the meter beam, as shown in the legend.

waveguides [72, 73]. Lei et al. provides a theoretical model depicting the effects of strong cavity coupling to a Λ type three level atom. In this model, residual reflections of the control (meter) field from the cavity act like additional control fields at a shifted frequency [72]. This leads to the formation of multiple peaks which increase and shift with increasing control power [72]. While the behaviour is similar to our case, there is no cavity in any way for our system. A slightly more similar system is in the effect of the waveguide in [73]. The paper involves a 1-dimensional waveguide with N atoms inside. The main result of this paper is that this theoretical model purports that this system would act as a single atom with (N+1) levels [73]. This could indeed produce multiple peaks in a two-photon absorption system with sufficient power. However, this is only theoretical and, while the hollow-core fiber provides good spatial confinement, there is not enough confinement or enough atoms to consistently create this two-peak phenomenon.
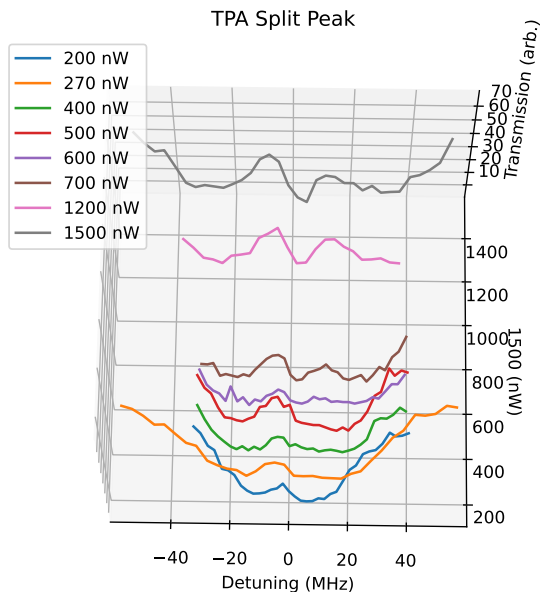
Figure 6.6: Preliminary data of two-photon absorption for the $6S_{1/2} \rightarrow 6P_{3/2} \rightarrow 8S_{1/2}$ ladder scheme in cold cesium atoms loaded into the hollow-core fiber. The meter beam is detuned in an attempt to compensate for an observed offset. The different lines are at different powers for the meter beam, as shown in the legend.

Finally, we arrive at a more likely scenario of a stray magnetic field leading to Zeeman splitting and the lifting of the magnetic sublevel degeneracies. Such an outcome has been observed both theoretically and experimentally multiple times [74, 75, 76]. How this leads to multiple peaks is explained below. An external magnetic field is applied to the system. This magnetic field causes the degeneracy of the magnetic sub-levels (m_F states) to be lifted due to the Zeeman effect. This splitting leads to a larger number of non-degenerate energy levels, allowing for more combinations of probe and control transitions based on selection rules. The result is the observation of multiple EIT windows, with the number depending on the magnetic field strength and the specific polarizations of the optical fields [74]. The size of the Zeeman splitting is determined by the strength of the magnetic field and is related to the hyperfine structure of the atomic levels. The selection rules for two-photon transitions depend on the polarizations of the input optical fields and the orientation of
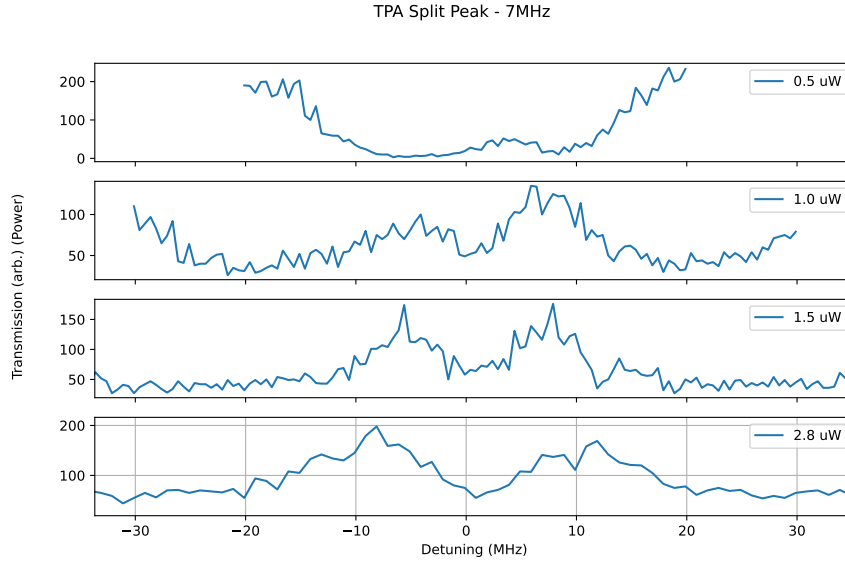
Figure 6.7: Preliminary data of two-photon absorption for the $6S_{1/2} \rightarrow 6P_{3/2} \rightarrow 8S_{1/2}$ ladder scheme in cold cesium atoms loaded into the hollow-core fiber. The meter beam is detuned in an attempt to compensate for an observed offset. The different plots are at different powers for the meter beam, as shown in the legend.

the applied magnetic field. For example, parallel polarization of the two fields requires $\Delta m_F = 0$, while perpendicular polarization allows $\Delta m_F = \pm 1$ [75]. Circular polarizations (left and right) follow $\Delta m_F = \pm 1$ selection rules [75]. The applied magnetic field leads to the formation of clusters of EIT components based on the selection rules [74]. Each Δm_F component consists of a cluster of lines, corresponding to allowed dipole transition routes that satisfy the two-photon selection rule. The magnetic field results in the splitting of the EIT window into various clusters, each associated with specific Δm_F values [74]. An atom can be excited through different cascade systems, creating different EIT windows. The applied magnetic field causes the $\Delta m_F = \pm 2$ EIT windows to shift in frequency space, leading to multiple, non-degenerate EIT windows [74]. The presence of the magnetic field results in a reduction in the depth of the observed EIT windows.

Of course, it is important to note that there is no purposeful applied magnetic field in our experiment when these datasets were taken. Thus, if this explanation applies, then a stray magnetic field of sufficient strength must be present. The best way to test this would either be to measure the magnetic field in the vicinity of the vacuum cell with a high resolution Hall probe or to purposefully add a magnetic field to see if more

transparency windows appear. This could, in principle, be done using the DC bias coils in our experimental setup (utilized in chapter 2).

6.2   Quantum memory schemes

Quantum memories are an integral component to any form of quantum information processing where two signals need to interact and timing becomes extremely important. Such systems include any multi-bit circuit in quantum computing, traffic control in quantum communication protocols, and naturally, entanglement swapping in quantum repeaters. There are a few different media in which quantum memories have been implemented, as mentioned in the first chapter, but we will focus on the cold atom variant throughout this chapter. Typically, quantum memory is implemented in cold atoms using one of the possible three-level schemes: the Λ-scheme, or the ladder scheme. The illustrations for these schemes can be found in figure 6.8.

There are a few considerations to be made when choosing one of these schemes. Often the most thought-of property of a quantum memory is its lifetime. This is straightforward as too short a lifetime limits the use-cases and flexibility of the memory. For this, researchers tend towards a Λ-scheme for their memory due to the storage state being a stable ground state with no dipole allowed transition to the initial ground state.

The result is a memory with lifetimes in the 10's of milliseconds or more [34]. However, experimentalists using this scheme will quickly realize a few drawbacks. The most prominent challenge is that the two ground states are less than 10 GHz apart for any alkalai atom which makes filtering out the strong control beam a difficult task that limits efficiency. There is also an additional need to prep the atomic medium as, since the storage state is a stable ground state, there can be a large portion of atoms populating the storage state. In some cases, significant noise arising from Raman scattering can affect this scheme. Albeit, this noise may predominantly affect warm atom implementations rather than cold atoms [77]. Finally, Λ-schemes have a limited bandwidth due nearby hyperfine states that are only a few 100 MHz to which could be accidentally coupled [78]. Thus, ladder schemes have begun to appear more in atomic implementations of quantum memories.

These memories, as shown in part B of figure 6.8, have only one ground state and now two excited states with the storage state being the highest energy level. Unlike Λ-schemes, they have a large separation of frequency between their probe and control on the order of at least a few terahertz. This makes filtering a strong control beam much simpler with options like gratings or spectral bandpass filters available with efficiencies often beyond
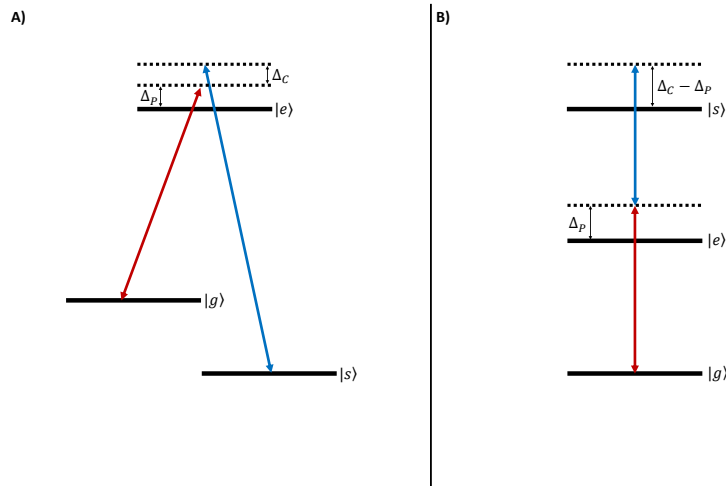
Figure 6.8: Possible level schemes for implementing quantum memory in an atomic medium. A) a lambda (Λ) type scheme involves two ground states with a single, shared, excited state. B) A ladder or cascade scheme involves a single ground state and two excited states where the upper excited state has no direct, dipole-allowed, decay path to the ground state. The levels for both schemes are labelled as: $|g\rangle$ for ground state, $|e\rangle$ for excited state, and $|s\rangle$ for the storage state.

90%. Ladder schemes also have no problem with unwanted population in the storage state due to it being an excited state. Finally, the hyperfine states are no longer a factor for the bandwidth, allowing for GHz bandwidths. The major drawback for this implementation is clearly the lifetime as the storage state is an excited state which means its lifetime can be limited to 10's or 100's of nanoseconds. Although, one can compensate for this by choosing a storage state with a much higher principal quantum number (i.e. Rydberg state). Doing so can push the lifetime to μs scale [79, 80, 81], while ms times can be done with a Rydberg blockade and shelving to the second ground state [82].

6.2.1 Slow light and dispersion

With absorption and dispersion corresponding to the imaginary and real part of the medium's susceptibility, the Kramers-Kronig relation links any irregularity in absorption with one in dispersion. When EIT is present, the group velocity of light is significantly reduced due to positive dispersion, and it can be further slowed down by lowering the intensity of the control field [27]. This phenomenon, known as "slow light," has practical

applications in buffering optical communication traffic and forms the basis for quantum memory. In quantum memory, a light pulse is slowed down and compressed inside the EIT medium, and it can be stored and later retrieved by adjusting the control field intensity [27]. Thus, a simple test to see whether memory could be implemented with the current loading efficiency of cold cesium into the hollow-core fiber would be to observe a significant delay of a short pulse of light passing through the transparency window of the atom cloud under EIT conditions.
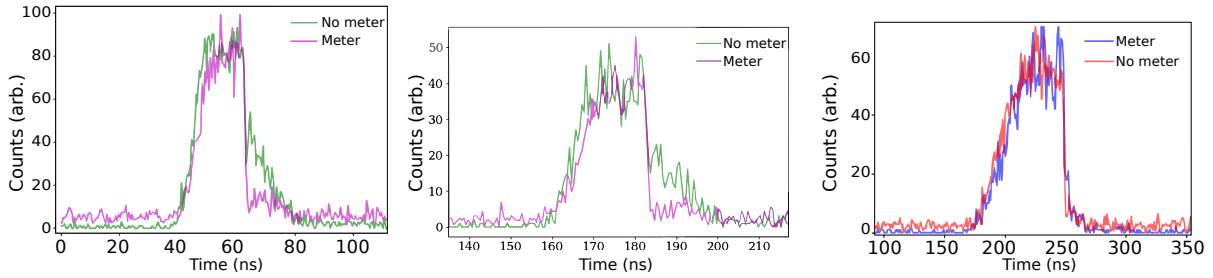
Figure 6.9: Delay measurement of light pulse with a full-width at half maximum (FWHM) of 30 ns passing through cold atomic cesium loaded into the hollow-core fiber. The atomic medium is under EIT conditions with the ladder scheme and the meter beam is detuned to +16 MHz. The pulse is detuned by -16 MHz such that the pulse is aligned with the transparency window. The different plots are simply different attempts using the same system and same settings.

Figure 6.9 shows the results of the delay test. Here, the signal without the control beam on is adjusted to match the height of the signal with the control beam to better see if there is any delay (the signal without the control beam will undergo some absorption so it will be of a lower height). Each subplot in figure 6.9 are simply repeated attempts to see if there is any noticeable delay due to the nonlinear dispersion under EIT conditions. It does appear that there is some consistent lag to the pulse within the transparency compared to the pulse transmitted without the control beam. This delay is only 1-2 ns which means that our system does not exhibit significantly strong dispersion yet. The strength of the dispersion is directly related to susceptibility which depends on the optical depth and coherence of the system and so, increasing the loading efficiency of atoms into the hollow-core fiber remains a high priority.

Temporarily moving away from the ladder scheme, the lambda scheme was also tested with the cold atom setup to examine its viability for full memory experiments. Unfortunately, experimentally observing EIT with the lambda scheme is much more challenging in
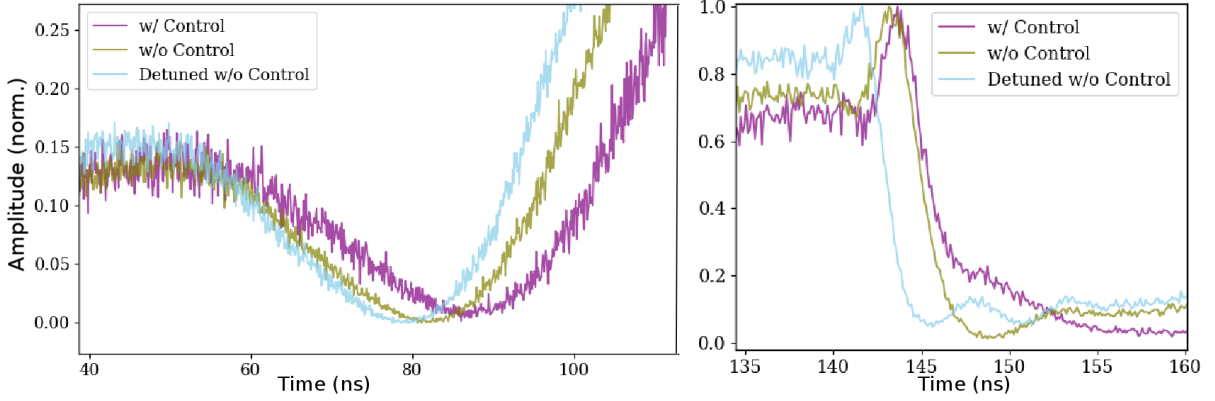
Figure 6.10: Trapezoidal light pulse with FWHM of 50 ns sent through a warm cesium vapour cell under EIT conditions using the lambda scheme. The left plot is the leading edge of the pulse whereas the right plot is the trailing edge. The control and probe are each detuned by 310MHz from the resonance of their respective transitions, such that the pulse's central frequency is aligned with the EIT transparency window. The detuned case without the control beam is detuned by 600 MHz such that there is no absorption by the atoms.

the filtering of the strong control beam. Due to the current limitations in filtering, we were unable to observe a clear signal in the hollow-core fiber setup. As a proof of principle, a warm cesium vapour cell was used to test the delay measurement with the lambda scheme. Initially, a trapezoidal pulse was tested and the results are shown in figure 6.10. There are three different pulses depicted in this figure: a pulse aligned with the transparency window with the control beam on, a pulse aligned with the transparency window without the control beam, and a pulse far-detuned away from the absorption dip without the control beam on. Ultimately these will undergo: a delay due to dispersion from an EIT-determined susceptibility, a delay due to a dispersion from a two-level susceptibility, and almost no delay as the dilute gas will have an effective refractive index near vacuum. Based on figure 6.10, there is roughly a 4 ns delay due to two-level dispersion and an additional 6.7 ns due to the EIT dispersion. However, a trapezoidal pulse is not quite the best appraoch for this measurement as it will have multiple frequency components which are affected by dispersion differently, leading to a distorted output. It is much better to use a Gaussian pulse, if possible, due to a Gaussian remaining a Gausian under Fourier transforms. Figure 6.11 shows the result of moving to Gaussian pulses for the delay experiment. From the plots, the observed delays are 3.3 ns for the 10 ns pulses and 3.9 ns for the 20 ns pulses. The difference in delay between the two cases is not significant, although it is important

74
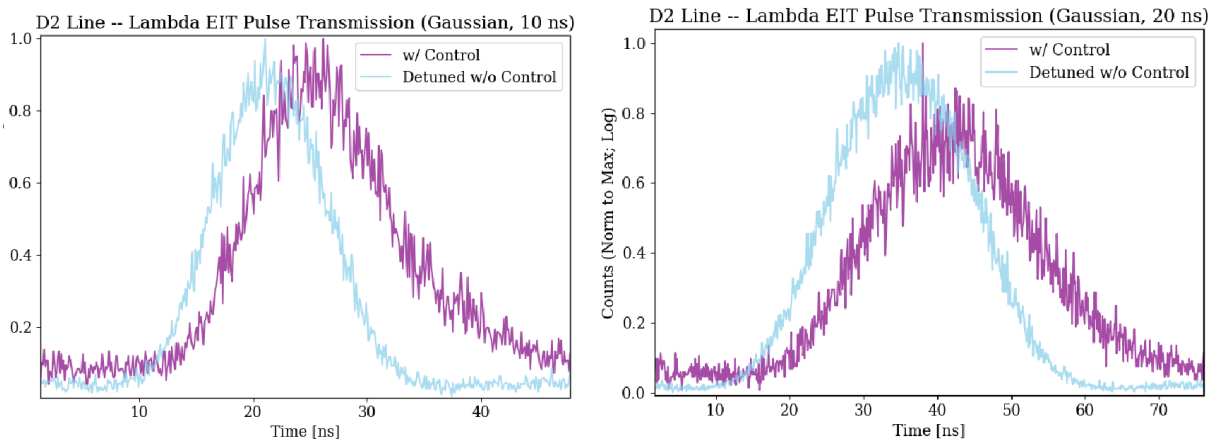
Figure 6.11: Gaussian light pulse with FWHM of 10 ns (left) and 20 ns (right) sent through a warm cesium vapour cell under EIT conditions using the lambda scheme. The control beam and probe are detuned in the same fashion as Fig. 6.10. The detuned case without the control beam is detuned by 600 MHz such that there is no absorption by the atoms.

to choose a pulse whose width corresponds to a bandwidth (Fourier transform) that can fit within the transparency window.

Chapter 7

Conclusion & Outlook

7.1 Summary

Fluorescence is a simple but useful diagnostic tool to analyze the atom cloud's properties. It highlights an equation for estimating the number of trapped atoms, considering various parameters such as detuning, intensity, and camera characteristics. While it may not provide an exact atom count, it serves as a valuable tool for optimization. There is another method for imaging the atom cloud, which involves shining a resonant beam through the cloud to create a shadow on a camera sensor. This method is used to estimate the number of atoms within the cloud and also assess its temperature. By tracking the cloud's expansion, the average velocity of atoms can be determined, allowing for temperature calculation. To better understand the trajectory of the atom cloud toward the fiber, a two-camera setup is used. This approach helps in aligning the densest part of the cloud with the fiber's core, improving loading quality. It also provides feedback for adjusting parameters, like the bias field, to optimize loading into the fiber. Optical bleaching, a single-shot measurement technique, provides a particularly potent characterization tool for measuring the number of atoms loaded into the hollow-core fiber. It involves sending a train of resonant pulses to "bleach" the atoms, moving them into a dark state. By counting the missing photons due to scattering, the number of loaded atoms can be determined. This method provides a reliable and quick way to estimate atom numbers and check probe coupling. The combination of these diagnostic tools allows for a comprehensive analysis of the atom cloud's properties, optimizing loading into the fiber for the experimental setup.

The implementation of a DAVLL system was used for the purpose of laser locking in experiments involving cascade/ladder schemes. The necessity of a different lock technique

is due to the laser needing to be locked to a transition between two excited state. This is because of the absence of population in the upper transition, making traditional laser locking architectures ineffective. DAVLL is introduced as a method that overcomes the challenge of locking lasers to transitions without upper-level population. It relies on the use of an external magnetic field across a vapor cell, which affects the degeneracy of the sublevels in the intermediate state. A typical DAVLL setup is outlined, which involves two counter-propagating lasers (meter and probe), a vapor cell with an external magnetic field, a quarter waveplate, a polarizing beam splitter, and matched photodiodes. The error signal for laser locking is generated by subtracting the signals from the matched photodiodes, creating a dip and a peak with a linear transition in between. The quality of laser locking through DAVLL using a frequency scan of the probe beam sent through a photonic crystal fiber loaded with cold cesium atoms was demonstrated. By varying the offset of the meter laser (794 nm), the transparency window is observed to shift as expected with a small observed, consistent, offset of 2 MHz. This offset is most likely due to an error in the RF wave used for the AOMs. In summary, the DAVLL method is introduced as an approach to laser locking for experiments involving cascade/ladder schemes, highlighting its use of EIT and transparency windows to lock lasers even when the upper transition has no population. The setup and results showcase the effectiveness of DAVLL in achieving the desired laser locking.

ML is then discussed in the context of optimizing experimental parameters in the field of cold atom physics. An overview is provided of machine learning principles, algorithmic models, and a specific Python-based tool called M-LOOP, which is used for machine learning in experimental settings. Machine learning is a subfield of artificial intelligence that focuses on developing algorithms and statistical models to improve computer system performance through experience and data. The training phase, cost function, and the choice of model are outlined as fundamental components of machine learning. Two machine learning models, Gaussian processes and neural networks, are discussed. Gaussian processes are highlighted as probabilistic models that account for uncertainty in predictions, while neural networks are deterministic and inspired by the human brain's structure. M-LOOP is introduced as a Python-based interface for implementing machine learning in experiments. It allows users to interact with various machine learning algorithms, input ranges, and other parameters for optimizing experimental outputs. The application of machine learning models in cold atom physics is specifically for optimizing the loading of atoms into a fiber. The choice of model, Gaussian processes, is explained due to its ability to handle uncertainty and avoid local minima. A 2-dimensional parameter scan of intensity and detuning for polarization gradient cooling is used as a test case to validate M-LOOP. Results are compared to a manual scan, and the ability of M-LOOP to navigate around

local minima is demonstrated. The use of different cost functions for machine learning was also explored. Two cost functions, one linear and another reciprocal, are applied to the 2-dimensional parameter space. The cost function's role in machine learning and its impact on convergence are discussed. A more extensive parameter space involving multiple experimental parameters is used for machine learning. The results indicate improvements in the number of loaded atoms but are still not at the desired levels. The need for a more robust system and longer optimization runs is emphasized. Overall, this section delves into the application of machine learning in cold atom physics experiments, showcasing its potential for optimizing complex experimental parameters, while also highlighting the challenges and choices involved in cost functions and parameter spaces.

The loading efficiency of atoms into the fiber's core is influenced by the strength and resonance characteristics of the dipole beam. Both a more intense and more resonant beam can create a deeper trap potential, theoretically leading to better loading efficiency. However, while moving closer to resonance increases trap depth, it also increases the scattering rate. Higher scattering rates can cause atom warming and scattering into a dark state. Conversely, moving far off resonance reduces the scattering rate but also the trap depth. The strong dipole beam introduces the AC Stark shift, which impacts energy levels of atoms due to the external oscillating electric field polarizing the atoms electronic state. The "magic wavelength" where the AC Stark shift for both ground and excited states is the same, can effectively mitigate the shift's effect. To avoid Stark shifts without using a magic wavelength, the use of a modulated dipole beam was introduced. This approach minimizes Stark shifting by probing with the dipole trap beam is off, allowing for greater flexibility in selecting the dipole trap wavelength. Experiments highlighting the loading efficiency with different wavelengths at equal trap depths were reported to test if there is an optimal wavelength to use as the dipole beam. There are notable deviations from the expected trends, particularly regarding 905 nm, which requires further investigation to understand the reasons behind its underperformance. This section lays the groundwork for understanding the complexities involved in optimizing atom loading in the fiber, including the trade-offs between trap depth, resonance, and the influence of Stark shifts. Further experiments and analysis are needed to fully comprehend the observed discrepancies and optimize the loading process.

The key aspects of two-photon electromagnetically induced absorption (TPEIA), focusing on the utilization of cold atomic cesium for wavelength conversion, was also explored. A four-wave mixing scheme is employed to enable the conversion of single photons. The efficiency of this conversion is contingent upon the choice of detunings, control field intensities, and the optical depth of the atomic core. Simulations indicate promising conversion efficiencies when an optical depth of 100 or higher is achieved. We also delved into two-photon

absorption within a ladder scheme, with an emphasis on the cascade or ladder scheme for quantum memory exploration. The ladder scheme offers advantages such as efficient filtering of the control beam, a lack of unwanted population in the storage state, and broad bandwidth capabilities. Theoretical and experimental results are presented, demonstrating the behavior of the ladder scheme and its potential applications in quantum memory systems. Notably, experimental tests of the ladder scheme reveal a modest delay of a couple of nanoseconds within the EIT medium, highlighting the potential for quantum memory applications. Additionally, the chapter discusses the phenomenon of slow light, which is crucial for quantum memory applications. Slow light, induced by positive dispersion under EIT conditions, has practical uses in optical communication traffic buffering and quantum memory. Experimental tests indicate a modest delay within the EIT medium, emphasizing the importance of improving the loading efficiency of cold cesium atoms into the hollow-core fiber. Finally, the lambda scheme is briefly explored, revealing challenges related to filtering the strong control beam. Despite these challenges, experimental tests using warm cesium vapor cells demonstrate delay measurements and the potential for lambda scheme-based quantum memory experiments. In summary, this chapter provides insights into the possibilities and challenges of utilizing cold atomic cesium for TPEIA, ladder schemes, slow light, and lambda schemes in the context of quantum memory and quantum information processing.

7.2 Outlook

7.2.1 Quantum dots

In the early stages of investigating the viability of getting single photons and entangled photons from the nanowire quantum dot sources in our lab, I pioneered the interfaces for excitation and characterization of the dots. The characterization is done by splitting the emission of the quantum dot with a 50/50 beamsplitter and monitoring the two output ports of the beamsplitter with SPCM. The counts are tagged using a high resolution time tagger device and those tags are analyzed via an autocorrelation program. This custom-built program read the photon tags as they were being collected and performed a $g^{(2)}(\tau)$ autocorrelation of the tags coming from each SPCM. By making use of some appropriately placed parellization, the program is able to compute coincidences at an 8 MHz rate. The result is a live readout of the photon statistics while the dot is emitting photons. This allows for the easier judgement of how long the experiment must run for until the statistics equilibrate, as opposed to waiting arbitrarily long times to get the result. The live readout

also allows for the detection of any experimental errors that may have occurred without having to run a full experiment before seeing the issue. The second component designed for the preliminary quantum dot experiment is the interface for excitation. Typically for solid-state photon sources (e.g. quantum dots, nitrogen-vacancy centers) a pulsed laser is used for excitation. Typically this is in the form of a broadly-tunable pulsed titanium;sapphire. However, this is a very expensive purchase for groups who only need it for a singular reason. Our approach is to make use of the much cheaper alternative of using a simple diode laser coupled to an electro-optic modulator (EOM). This implementation is roughly a tenth of the cost and allows for full control of the: pulse width, pulse shape, repetition rate, and wavelength of the pulse (changeable by using a different laser source). The problem for this setup lies in the nature of the EOM. The Michelson-interferometer-based device created pulses by splitting the light into two paths and applying a voltage that alters the length of one path such that there is constructive and destructive interference when the paths recombine at the output. This means that the shape of the voltage signal is imprinted on the optical signal; another way to look at it is that the EOM transduces an electronic signal into an optical signal. The aforementioned problem is that, like any interferometer, fluctuations in the path lengths will result in noise or background in the output. This led to a drift which, in turn, led to a slow increase in the background or "floor" of the pulses to a point where, from the perspective of the quantum dots, they were no longer pulses. This created a need for a circuit that could monitor the EOM output and apply a correcting voltage that kept the pulse contrast ratio maximized. The stabilizer is a digital circuit, that is reminiscent of a lock-in amplifier, that compares the phase accumulated by a small sinusoidal dither which results in an error signal that is anti-symmetric about zero. The reason to use a digital approach is to avoid some waveform distortion problems experienced in the analog lock-in amplifier. The results of the implementation of the stabilizer is shown in figure 7.1. These plots show an autocorrelation measurement of the output of the EOM with and without the stabilizer. The measurement follows the exact same procedure as the autocorrelation of the quantum dot emission. Effectively, this simply a high resolution means of observing these ultrashort (80-100 ps) laser pulses. The left plot of figure 7.1 shows the pulses without stabilization and the result is a very noisy background with a low contrast ratio of about 2.38. The background is very likely to cause unwanted excitation of the quantum dot which would lead to a poor autocorrelation of the quantum dot emission. The right plot of figure 7.1 shows the laser pulses with stabilization and there is a clear and significant reduction of the noisy background with a much-improved contrast ratio of 74.57.

The results of the stabilization can also be seen in figure 7.2. The top row of the plots are all measured without stabilization and the bottom row are all taken with stabilization.
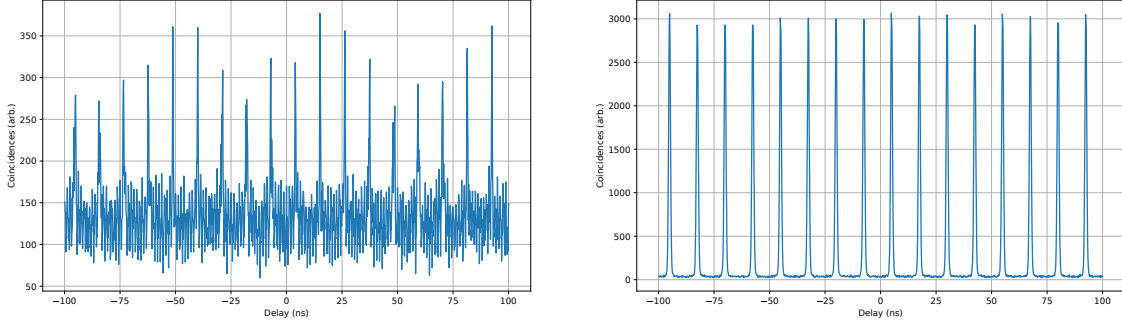
Figure 7.1: Autocorrelation of a pulsed laser used for exciting the quantum dots. The purpose of these plots is to verify that the pulse stabilizer circuit is working to suppress the background. It can be seen that the left plot (no stabilizer) is significantly noisier with a smaller contrast ratio of peak to background than the right plot (with stabilizer).

These plots also show the clear reduction of the background noise in the bottom row. This allows us to better asses the quality of single photons coming from our quantum dot source which is also shown in figure 7.2. The plots in the left column are autocorrelations of the exciton emission of the quantum dot. Such an emission is distinguished by individual photons ideally spaced out by the time between successive excitation pulses. Most notably, single photon sources are characterized by a lack of coincidences about $g^{(2)}(\tau = 0)$; this is most commonly known as anti-bunching. In the case of continuous-wave excitation, the coincidences beyond $\tau = 0$ equilibrate to 1 (normalized). However, when the excitation is pulsed, then there will be coincidences bunched by the repetition rate of the excitation pulses. Thus, the expectation for an ideal single photon source excited by pulses is to see an effective reformation of those pulses in the autocorrelation with a region of no coincidences in the domain, $\tau \in (-T_r, T_r)$ with T_r being the period of the pulse repetition. Of course experimentally speaking, the measurement will deviate from this ideal scenario in the form of a nonzero level around zero and a non infinitesimal width to the peaks that appear. These two features' size depend on the time jitter of both the SPCM and the pulsing of the laser, in addition to the quality of the quantum dot. How the quality of this single photon source is judged is by the ratio of coincidences at $\tau = 0$ and the average peak size of the pulses seen in the histogram. Generally, the accepted threshold for this value is $g^{(2)}(0) \leq 0.1$ for a source to be deemed a good source of single photons. In terms of the stabilized measurement in figure 7.2, this value would be about $g^{(2)}(0) = 0.047$. The right column of figure 7.2 shows the autocorrelation of the biexciton emission of the same quantum dot. An example level

81
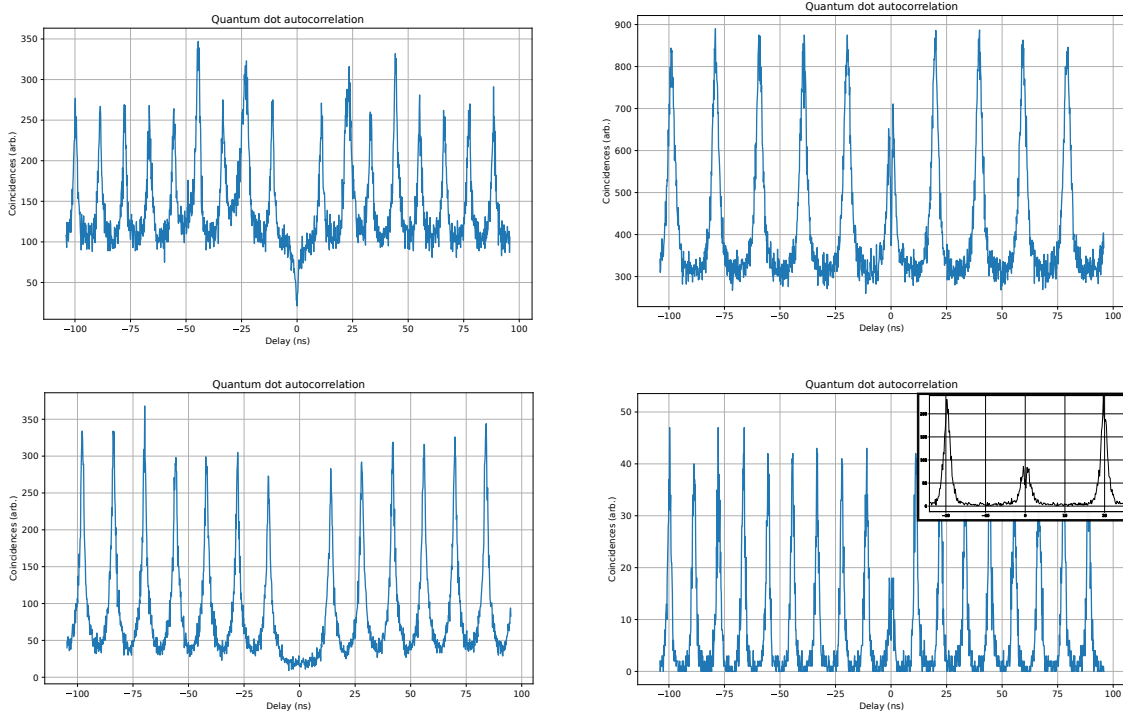
Figure 7.2: $g^{(2)}(\tau)$ autocorrelation of single photons from the quantum dot source due to: exciton emission (left column) and biexciton emission (right column). The top and bottom rows differ from the improvement made to the pulse stabilizer circuit for the excitation laser which dramatically reduces the noise in the emission. The inset in the bottom right plot is a continuation of the experiment in the main plot but with a small window to highlight the dip within the central peak.

diagram for a quantum dot is shown in figure 1.6 with $|XX\rangle, |X\rangle, |0\rangle$ representing the biexciton, exciton, and ground states, respectively. In the event of a quantum dot in the biexciton state, two photons will be emitted via a radiative cascade [30]. This behaviour appears in the autocorrelation via the signature "shoulder" peaks surrounding a dip near $\tau = 0$ (see the inset in figure 7.2). This excitation path is important as it is how we intend to generate entangled photon pairs as was previously observed [35, 30]. Overall, I successfully developed interfaces for excitation and characterization of nanowire quantum dot sources, which included a custom program for real-time photon statistics analysis, a cost-effective excitation method using a diode laser, an EOM, and a stabilizer circuit to improve the laser pulse quality, resulting in enhanced quality single photon and potential

entangled photon emission from the quantum dots.

7.2.2 Future improvements

In chapters 2, 4 and 5, there were multiple approaches to optimize the loading efficiency of cold atoms into a hollow-core fiber. Penultimately, there was significant progress made in loading more atoms, allowing us to observe nontrivial signals such as two-photon absorption as well as two and three-level delay of a pulse propagating through the loaded atoms. Ultimately, however, there is still a need for a greater number of atoms inside the fiber. This is necessary to implement the desired experiments of not only preliminary wavelength conversion and memory experiments, but also interfacing this cold atom system with the GHz-bandwidth single photons from the quantum dot source. Based on the simulation results presented in chapter 6, an optical depth in the range of 100 or larger affords us an efficiency of the aforementioned experiments to measure meaningful results beyond the noise of the system. One of the major improvements to the system which shall be implemented is moving to a solid-core fiber coupled input into the hollow-core fiber. Currently, the hollow-core fiber segment is isolated inside the vacuum chamber with light coupling in and out of the hollow-core being done in free-space using coupling lenses located just outside of the vacuum cell. Unfortunately, there are a few problems in this approach which can make optimizing atom loading challenging. The biggest limitation is the input coupling of requisite light sources into the core of the photonic crystal fiber. The limitation lies in the relatively short length of the hollow-core fiber segment. While it is considered a single-mode fiber, this definition is given due to the strong attenuation of higher order modes and there is an inherent assumption that the fiber is sufficiently long enough that these higher-order modes dissipate. Since our fiber segment is only 2.5 cm long, higher-order modes can still be quite strong, especially in terms of the attractive dipole beam whose power is in the 10's of milliWatts. This imposes some restrictions in how we characterize the settings of our system as noting the power inside the hollow-core is not as simple as a trivial power measurement after the light exits the fiber and vacuum cell. This would be the case for a normal length (> 1 m) of some more traditional solid-core fiber. We have observed dramatically different loading efficiencies for the same observed dipole beam power, with the only difference being an adjustment to the coupling mirrors going into the fiber. This would imply that, while the overall power exiting the fiber is the same, the amount coupled into the core compared to the cladding is less. Matters are made worse when the coupling also drifts and reduces the amount of time we can confidently run a machine-learning optimization.

To address this, We have developed an on-chip adapter which couples light from a

solid-core fiber into the hollow-core fiber segment. This chip, which works by bringing the ends of each fiber extremely close to each other (on the micron scale), hopes to provide a much more stable coupling into the hollow-core fiber. Even if the transfer of the light from the solid-core to the hollow-core is not perfect with some leakage into the cladding, the consistent translation of power measure and optical depth is the major desired outcome. A few other benefits can be had with this implementation as well. A fiber-coupled system allows are more efficient interface for multi-beam input. Overlapping multiple beams in free-space typically requires partially reflective elements (e.g. windows, beam samplers, beam splitters) with some beams being reflected and some transmitted. Unfortunately, so much power is simply being wasted in this approach and while some beams like the probe need to be weak anyway, it can be restricting in terms of scanning higher powers in the experimental parameter space. One can mitigate this by fiber coupling and then using a fiber-based splitter/multiplexer to reduce the free-space part to just one beam path. This would be a natural progression once the fiber adapter chip is used and so the adapter grants the added benefit of stability by removing the free space section just before the vacuum cell entirely. Improved stability in the system enables the usage of machine learning for larger parameter spaces that require longer durations of measurement.

With this implementation, we also wish to revisit the measurements outlined in chapter 5. While we believe the results shown in figure 5.7 to be very close to an accurate picture of the effect of dipole wavelength on the loading of atoms into the fiber. However, the results from 5.6 noticeably depart from the conclusion arrived at by figure 5.7. We wish to reconcile these differences and better understand the errors in measurement that led to them. Currently, the perceived origin of the error is the previously discussed notion of accidental coupling of the dipole beam to higher-order modes of the hollow-core fiber. By stabilizing the coupling into the hollow-core via the fiber coupling chip mentioned above, we hope to redo the measurement performed in figure 5.6 and arrive at a conclusion which matches both figure 5.7 and some trends established with different atom species.

Simultaneously, we want to continue pushing the use of machine learning with our experiment further. Greater stability grants the possibility of overnight runs with machine learning which could allow for an input parameter space dimensionality of 9 or more. This is far more than the 2-4 dimensions we have tested so far. Currently, we have established a nominal loading of 1000 atoms on a daily basis and we have in the past achieved a loading of 10,000 atoms. However, the past results, while extremely consistent until the experimental setup had to be reset, were achieved with brute force probing of parameters with perhaps a bit of luck. Thus, we have reason to believe we can achieve 10,000 atoms loaded into the hollow-core fiber again, but achieving this using a systematic optimization is significantly important to maintain progress in the lab when major changes are necessary.

Improving optical depth has been a recurring theme for most chapters in this dissertation. Although, this is not the only factor that affects the efficiency of the major results we wish to realize such as wavelength conversion and quantum memory. As per the susceptibility derived in chapter 6, coherence times of the atoms involved also play a strong role. Decoherence is a common problem for every quantum system and neutral atoms are no different. Sources of decoherence range from thermal, magnetic, electric and optical fluctuations from either the environment or experimental elements (e.g. magnetic coils, laser beam shape and intensity profile). A major focus for the future of this experimental setup is to investigate the temperature of the atomic cloud just after it has been loaded into the fiber. Temperature measurements of the cloud outside the fiber is done via a time of flight captured with absorption images (see 2.2.2). However, once loaded inside the fiber, absorption images are no longer useful. Thus, a new method for ascertaining the temperature of the atoms once loaded must be used. Our approach is to turn of the attractive dipole beam for some amount of time, t_d, and perform the "bleaching" measurement described in 2.2.4. This measurement gives us the number of atoms inside the fiber as a function of t_d which should decrease the longer the atoms spend without a dipole beam to draw them to the center of the fiber. Therefore, in a similar means of resolving the cloud's temperature from the cloud expansion at increasing time after release, the temperature could be similarly arrived at inside the fiber. This is approximated by the equation [83]:

$$N(t_d) \approx N_0 \left(1 - \exp\left\{ \frac{-\left(R_{\text{core}}/r_0\right)^2}{1 + \left(v_T/r_0\right)^2 t_d^2} \right\} \right) \tag{7.1}$$

Ultimately, the goal would be to extend the time before the atoms collide with the walls of the fiber. From here, we can attempt transverse cool the atoms while inside the fiber. Transverse cooling is achieved by introducing a blue-detuned laser beam into a dipole trap that guides atoms in an optical fiber [51]. This blue-detuned light preferentially scatters atoms from one energy state to another. As the atoms naturally decay back to their original state, their energy decreases due to the difference in Stark shift between these two states. A low-power repumper laser, which works more efficiently at the trap's edge due to the position-dependent Stark shift, recycles the atoms back to their original state [51]. This cooling process occurs as atoms move back and forth within the trap. The energy reduction corresponds to the peak energy difference between the Stark-shifted hyperfine states during each cycle, resulting in cooling of the atoms.

The interest in interfacing cold neutral atoms with waveguides has rapidly grown since the inception of the evanescent wave-based mirrors. Thereafter, a myriad of different waveguides have been used in conjunction with a few different atomic species. From plasmonic, slot and ridge waveguides, 1D and 2D photonic crystals, anti-resonant reflecting

optical waveguides (ARROW), nanobeams, nanofibers, and of course hollow-core photonic crystal fibers; there are so many different approaches to maximize the capabilities of cold atoms. While there is still some progress to be made in improving loading efficiency, the experimental control interfaces and diagnostic tools outlined in this dissertation are crucial to systematically recover loading when changes are made to the setup. If we wish to implement the change to a fiber-coupled direct input into the hollow-core fiber in the vacuum cell, these tools become extremely useful. We can couple this with the promising results from the machine learning integration to push the efficiency further with a full parameter space scan. While we have confidence that there will be improvement in the atom loading, our hopes are to test quantum memory protocols with our setup as well as attempt to interface the single photons with the cold atoms. Such experiments would lead to a significant step forward in the realization of a quantum repeater and the development of quantum networks.

References

[1] Vladimir Georgievich Minogin and Vladilen Stepanovich Letokhov. *Laser light pressure on atoms*. CRC Press, 1987.

[2] Othmar Marti and Victor I Balykin. Light forces on dielectric particles and atoms. In *Near Field Optics*, pages 121–130. Springer, 1993.

[3] Richard J Cook and Richard K Hill. An electromagnetic mirror for neutral atoms. *Optics Communications*, 43(4):258–260, 1982.

[4] Max Born et al. E. wolf principles of optics. *Pergamon Press*, 6(188):36–111, 1985.

[5] VI Balykin and VS Letokhov. Atomic cavity with light-induced mirrors. *Applied Physics B*, 48:517–523, 1989.

[6] Mark A Kasevich, David S Weiss, and Steven Chu. Normal-incidence reflection of slow atoms from an optical evanescent wave. *Optics letters*, 15(11):607–609, 1990.

[7] H Wallis, J Dalibard, and C Cohen-Tannoudji. Trapping atoms in a gravitational cavity. *Applied Physics B*, 54:407–419, 1992.

[8] Yu B Ovchinnikov, SV Shul'Ga, and VI Balykin. An atomic trap based on evanescent light waves. *Journal of Physics B: Atomic, Molecular and Optical Physics*, 24(14):3173, 1991.

[9] MA Ol'Shanii, Yu B Ovchinnikov, and VS Letokhov. Laser guiding of atoms in a hollow optical fiber. *Optics communications*, 98(1-3):77–79, 1993.

[10] Bruno Crosignani, Paolo Diporto, and Salvatore Solimeno. Guiding, diffraction, and confinement of optical radiation. *Guiding*, 1986.

[11] Michael J Renn, D Montgomery, O Vdovin, DZ Anderson, CE Wieman, and EA Cornell. Laser-guided atoms in hollow-core optical fibers. *Physical review letters*, 75(18):3253, 1995.

[12] Hendrik Christoffel Hulst and Hendrik C van de Hulst. *Light scattering by small particles*. Courier Corporation, 1981.

[13] H Mabuchi and HJ Kimble. Atom galleries for whispering atoms: binding atoms in stable orbits around an optical resonator. *Optics letters*, 19(10):749–751, 1994.

[14] F Treussart, J Hare, L Collot, V Lefevre, DS Weiss, Vahid Sandoghdar, JM Raimond, and S Haroche. Quantized atom-field force at the surface of a microsphere. *Optics letters*, 19(20):1651–1653, 1994.

[15] Fam Le Kien, VI Balykin, and K Hakuta. Atom trap and waveguide using a two-color evanescent light field around a subwavelength-diameter optical fiber. *Physical Review A*, 70(6):063403, 2004.

[16] Limin Tong and Eric Mazur. Subwavelength-diameter silica wires for microscale optical components. In *Optical Components and Materials II*, volume 5723, pages 105–112. SPIE, 2005.

[17] Fam Le Kien, S Dutta Gupta, VI Balykin, and K Hakuta. Spontaneous emission of a cesium atom near a nanofiber: Efficient coupling of light to guided modes. *Physical Review A*, 72(3):032509, 2005.

[18] Fam Le Kien, Victor I. Balykin, and Kohzo Hakuta. State-insensitive trapping and guiding of cesium atoms using a two-color evanescent field around a subwavelength-diameter fiber. *Journal of the Physical Society of Japan*, 74(3):910–917, 2005.

[19] Pochi Yeh, Amnon Yariv, and Emanuel Marom. Theory of bragg fiber. *JOSA*, 68(9):1196–1201, 1978.

[20] RF Cregan, JC Knight, P St J Russell, and PJ Roberts. Spontaneous emission from an erbium doped photonic crystal fibre. In *Technical Digest. Summaries of Papers Presented at the Quantum Electronics and Laser Science Conference*, pages 270–271. IEEE, 1992.

[21] Tim A Birks, Jonathan C Knight, and P St J Russell. Endlessly single-mode photonic crystal fiber. *Optics letters*, 22(13):961–963, 1997.

[22] Philip Russell. Photonic crystal fiber: finding the holey grail. *Optics and photonics news*, 18(7):26–31, 2007.

[23] T Takekoshi and RJ Knize. Optical guiding of atoms through a hollow-core photonic band-gap fiber. *Physical review letters*, 98(21):210404, 2007.

[24] Vlatko Balic, Michal Bajcsy, Alexander Zibrov, Vladan Vuletic, and Mikhail Lukin. Cold atoms inside a hollow-core photonic-crystal fiber. In *APS Division of Atomic, Molecular and Optical Physics Meeting Abstracts*, volume 38, pages K1–073, 2007.

[25] Lei Chen, Greg J. Pearce, Timothy A. Birks, and David M. Bird. Guidance in kagome-like photonic crystal fibres i: analysis of an ideal fibre structure. *Opt. Express*, 19(7):6945–6956, Mar 2011.

[26] M.D. Lukin. Lecture notes in modern atomic and optical physics ii, Decmber 2016.

[27] Alexander I Lvovsky, Barry C Sanders, and Wolfgang Tittel. Optical quantum memory. *Nature photonics*, 3(12):706–714, 2009.

[28] Michael R Sprague, Duncan G England, Amir Abdolvand, Joshua Nunn, Xian-Min Jin, W Steven Kolthammer, Marco Barbieri, Bruno Rigal, Patrick S Michelberger, Tessa FM Champion, et al. Efficient optical pumping and high optical depth in a hollow-core photonic-crystal fibre for a broadband quantum memory. *New Journal of Physics*, 15(5):055013, 2013.

[29] CM Haapamaki, J Flannery, G Bappi, R Al Maruf, SV Bhaskara, O Alshehri, T Yoon, and M Bajcsy. Mesoscale cavities in hollow-core waveguides for quantum optics with atomic ensembles. *Nanophotonics*, 5(3):392–408, 2016.

[30] Marijn AM Versteegh, Michael E Reimer, Klaus D Jöns, Dan Dalacu, Philip J Poole, Angelo Gulinatti, Andrea Giudice, and Val Zwiller. Observation of strongly entangled photon pairs from a nanowire quantum dot. *Nature communications*, 5(1):5298, 2014.

[31] J-P Bourgoin, E Meyer-Scott, B L Higgins, B Helou, C Erven, H Hübel, B Kumar, D Hudson, I D'Souza, R Girard, R Laflamme, and T Jennewein. A comprehensive design and performance analysis of low earth orbit satellite quantum communication. *New Journal of Physics*, 15(2):023006, feb 2013.

[32] James J. Refi. Optical fibers for optical networking. *Bell Labs Technical Journal*, 4(1):246–261, 1999.

[33] Di Zhu, Linbo Shao, Mengjie Yu, Rebecca Cheng, Boris Desiatov, C. J. Xin, Yaowen Hu, Jeffrey Holzgrafe, Soumya Ghosh, Amirhassan Shams-Ansari, Eric Puma, Neil Sinclair, Christian Reimer, Mian Zhang, and Marko Lončar. Integrated photonics on thin-film lithium niobate. *Adv. Opt. Photon.*, 13(2):242–352, Jun 2021.

[34] YO Dudin, L Li, and A Kuzmich. Light storage on the time scale of a minute. *Physical Review A*, 87(3):031801, 2013.

[35] Michael E Reimer, Marek Korkusinski, Jacques Lefebvre, Jean Lapointe, Philip J Poole, Geof C Aers, Dan Dalacu, W Ross McKinnon, Simon Frederick, Pawel Hawrylak, et al. Voltage induced hidden symmetry and photon entanglement generation in a single, site-selected quantum dot. *arXiv preprint arXiv:0706.1075*, 2007.

[36] Rubayet Al Maruf, Sreesh Venuturumilli, Divya Bharadwaj, Paul Anderson, Jiawei Qiu, Yujia Yuan, Mohd Zeeshan, Behrooz Semnani, Philip J Poole, Dan Dalacu, et al. Widely tunable solid-state source of single-photons matching an atomic transition. *arXiv preprint arXiv:2309.06734*, 2023.

[37] E Poem, C Weinzetl, J Klatzow, KT Kaczmarek, JHD Munns, TFM Champion, DJ Saunders, J Nunn, and IA Walmsley. Broadband noise-free optical quantum memory with neutral nitrogen-vacancy centers in diamond. *Physical Review B*, 91(20):205108, 2015.

[38] Aleksei R. Matanin, Konstantin I. Gerasimov, Eugene S. Moiseev, Nikita S. Smirnov, Anton I. Ivanov, Elizaveta I. Malevannaya, Victor I. Polozov, Eugeny V. Zikiy, Andrey A. Samoilov, Ilya A. Rodionov, and Sergey A. Moiseev. Toward highly efficient multimode superconducting quantum memory. *Phys. Rev. Appl.*, 19:034011, Mar 2023.

[39] Pengfei Wang, Chun-Yang Luan, Mu Qiao, Mark Um, Junhua Zhang, Ye Wang, Xiao Yuan, Mile Gu, Jingning Zhang, and Kihwan Kim. Single ion qubit with estimated coherence time exceeding one hour. *Nature Communications*, 12(1):233, Jan 2021.

[40] Anindya Rastogi, Erhan Saglamyurek, Taras Hrushevskyi, Scott Hubele, and Lindsay J. LeBlanc. Discerning quantum memories based on electromagnetically-induced-transparency and autler-townes-splitting protocols. *Phys. Rev. A*, 100:012314, Jul 2019.

[41] Jinxian Guo, Xiaotian Feng, Peiyu Yang, Zhifei Yu, L. Q. Chen, Chun-Hua Yuan, and Weiping Zhang. High-performance raman quantum memory with optimal control in room temperature atoms. *Nature Communications*, 10(1):148, Jan 2019.

[42] D.A. Steck. Cesium d line data.

[43] Taehyun Yoon and Michal Bajcsy. Laser-cooled cesium atoms confined with a magic-wavelength dipole trap inside a hollow-core photonic-bandgap fiber. *Phys. Rev. A*, 99:023415, Feb 2019.

[44] Paul B Wigley, Patrick J Everitt, Anton van den Hengel, John W Bastian, Mahasen A Sooriyabandara, Gordon D McDonald, Kyle S Hardman, Ciaron D Quinlivan, P Manju, Carlos CN Kuhn, et al. Fast machine-learning online optimization of ultra-cold-atom experiments. *Scientific reports*, 6(1):25890, 2016.

[45] Adam J Barker, Harry Style, Kathrin Luksch, Shinichi Sunami, David Garrick, Felix Hill, Christopher J Foot, and Elliot Bentine. Applying machine learning optimization methods to the production of a quantum gas. *Machine Learning: Science and Technology*, 1(1):015007, 2020.

[46] David Barber. *Bayesian reasoning and machine learning.* Cambridge University Press, 2012.

[47] P. B. Wigley, P. J. Everitt, A. van den Hengel, J. W. Bastian, M. A. Sooriyabandara, G. D. McDonald, K. S. Hardman, C. D. Quinlivan, P. Manju, C. C. N. Kuhn, I. R. Petersen, A. N. Luiten, J. J. Hope, N. P. Robins, and M. R. Hush. Fast machine-learning online optimization of ultra-cold-atom experiments. *Scientific Reports*, 6(1):25890, May 2016.

[48] Michal Bajcsy, S Hofferberth, Thibault Peyronel, Vlatko Balic, Qiangrong Liang, AS Zibrov, Vladan Vuletic, and Mikhail D Lukin. Laser-cooled atoms inside a hollow-core photonic-crystal fiber. *Physical Review A*, 83(6):063830, 2011.

[49] Frank Blatt, Thomas Halfmann, and Thorsten Peters. One-dimensional ultracold medium of extreme optical depth. *Optics Letters*, 39(3):446–449, 2014.

[50] Ashby P Hilton, Christopher Perrella, Fetah Benabid, Ben M Sparkes, Andre N Luiten, and Philip S Light. High-efficiency cold-atom transport into a waveguide trap. *Physical Review Applied*, 10(4):044034, 2018.

[51] Thibault Peyronel, Michal Bajcsy, Sebastian Hofferberth, Vlatko Balic, Mohammad Hafezi, Qiyu Liang, Alexander Zibrov, Vladan Vuletic, and Mikhail D Lukin. Switching and counting with atomic vapors in photonic-crystal fibers. *IEEE Journal of Selected Topics in Quantum Electronics*, 18(6):1747–1753, 2012.

[52] Rudolf Grimm, Matthias Weidemüller, and Yurii B Ovchinnikov. Optical dipole traps for neutral atoms. In *Advances in atomic, molecular, and optical physics*, volume 42, pages 95–170. Elsevier, 2000.

[53] Chung-Yu Shih. *Characterizing Single Atom Dipole Traps For Quantum Information Applications*. PhD thesis, Georgia Insitute of Technology, 2013.

[54] K Fredriksson, Hans Lundberg, and Sune Svanberg. Fine-and hyperfine-structure investigation in the 5 d 2- n f 2 series of cesium. *Physical Review A*, 21(1):241, 1980.

[55] Andrew Kortyna, C Tinsman, J Grab, MS Safronova, and UI Safronova. Experimental and theoretical study of the 6 d 3/2 polarizability of cesium. *Physical Review A*, 83(4):042511, 2011.

[56] Baodong Yang, Zhiyu Gou, Junmin Wang, and Haitao Zhou. Doppler-free dual-excited state spectroscopy and its application for measurement of hyperfine structure of 6d5/2 level of 133cs. *Applied Physics B*, 128(11):212, 2022.

[57] MT Herd, EC Cook, and WD Williams. Absolute frequency measurement of the 6 d 5/2 level of neutral cs 133 using two-photon spectroscopy. *Physical Review A*, 104(4):042812, 2021.

[58] Yunhui He, Jiabei Fan, Liping Hao, Yuechun Jiao, and Jianming Zhao. Precise measurement of hyperfine structure of cesium 7 s 1/2 excited state. *Applied Sciences*, 10(2):525, 2020.

[59] Guang Yang, Jie Wang, Baodong Yang, and Junmin Wang. Determination of the hyperfine coupling constant of the cesium 7s1/2 state. *Laser Physics Letters*, 13(8):085702, 2016.

[60] George Toh, Jose A Jaramillo-Villegas, Nathan Glotzbach, Jonah Quirk, Ian C Stevenson, Jungo Choi, Andrew M Weiner, and Daniel S Elliott. Measurement of the lifetime of the 7 s s 1/2 2 state in atomic cesium using asynchronous gated detection. *Physical Review A*, 97(5):052507, 2018.

[61] WD Williams, MT Herd, and WB Hawkins. Spectroscopic study of the 7p1/2 and 7p3/2 states in cesium-133. *Laser Physics Letters*, 15(9):095702, 2018.

[62] ZJ Jabbour, RK Namiotka, J Huennekens, Maria Allegrini, S Milošević, and F De Tomasi. Energy-pooling collisions in cesium: 6 p j+ 6 p j→ 6s+ (nl= 7p, 6d, 8s, 4f). *Physical Review A*, 54(2):1372, 1996.

[63] George Toh, Nathan Chalus, Andrew Burgess, Amy Damitz, Poolad Imany, Daniel E Leaird, Andrew M Weiner, Carol E Tanner, and DS Elliott. Measurement of the lifetimes of the 7 p 2 p 3/2 and 7 p 2 p 1/2 states of atomic cesium. *Physical Review A*, 100(5):052507, 2019.

[64] Andrew Kortyna, Nicholas Masluk, and Jonathan Farrar. Atomic beam measurements of theˆ 133cs 7dˆ 2d j hyperfine structure. In *APS Division of Atomic, Molecular and Optical Physics Meeting Abstracts*, volume 37, pages G1–034, 2006.

[65] K-H Weber and Craig J Sansonetti. Accurate energies of ns, np, nd, nf, and ng levels of neutral cesium. *Physical Review A*, 35(11):4650, 1987.

[66] Jonah A Quirk, Liam Sherman, Amy Damitz, Carol E Tanner, and DS Elliott. Measurement of the hyperfine coupling constants and absolute energies of the 8 p p 1/2 2 and 8 p p 3/2 2 levels in atomic cesium. *Physical Review A*, 107(1):012807, 2023.

[67] Carlos R Menegatti, Bruno S Marangoni, Nadia Bouloufa-Maafa, Olivier Dulieu, and Luis G Marcassa. Trap loss in a rubidium crossed dipole trap by short-range photoassociation. *Physical Review A*, 87(5):053404, 2013.

[68] N Akopian, L Wang, A Rastelli, OG Schmidt, and V Zwiller. Hybrid semiconductor-atomic interface: slowing down single photons from a quantum dot. *Nature Photonics*, 5(4):230–233, 2011.

[69] Johannes S Wildmann, Rinaldo Trotta, Javier Martín-Sánchez, Eugenio Zallo, Mark O'Steen, Oliver G Schmidt, and Armando Rastelli. Atomic clouds as spectrally selective and tunable delay lines for single photons from quantum dots. *Physical Review B*, 92(23):235306, 2015.

[70] Lucas Bremer, Sarah Fischbach, Suk-In Park, Sven Rodt, Jin-Dong Song, Tobias Heindel, and Stephan Reitzenstein. Cesium-vapor-based delay of single photons emitted by deterministically fabricated quantum dot microlenses. *Advanced Quantum Technologies*, 3(2):1900071, 2020.

[71] Ran Finkelstein, Samir Bali, Ofer Firstenberg, and Irina Novikova. A practical guide to electromagnetically induced transparency in atomic vapor. *New Journal of Physics*, 25(3):035001, 2023.

[72] Yan-Fen Sun, Lei Tan, and Yan Xu. Electromagnetically induced transparency of single λ-type three-level atoms in a high-finesse optical cavity. *Chinese Physics B*, 22(3):030309, 2013.

[73] WZ Jia and QY Cai. Multiple electromagnetically induced transparency without a control field in an atomic array coupled to a waveguide. *The European Physical Journal Plus*, 137(9):1–13, 2022.

[74] David J Fulton, Richard R Moseley, Sara Shepherd, Bruce D Sinclair, and Malcolm H Dunn. Effects of zeeman splitting on electromagnetically-induced transparency. *Optics communications*, 116(1-3):231–239, 1995.

[75] Sumit Bhushan, Vikas Singh Chauhan, M Dixith, and Raghavan K Easwaran. Effect of magnetic field on a multi window ladder type electromagnetically induced transparency with 87rb atoms in vapour cell. *Physics Letters A*, 383(31):125885, 2019.

[76] Rohit Hazra and Md Mabud Hossain. Study of multi-window electromagnetically induced transparency (eit) and related dispersive signals in v-type systems in the zeeman sublevels of hyperfine states of 87rb-d2 line. *Journal of Physics B: Atomic, Molecular and Optical Physics*, 53(23):235401, 2020.

[77] PS Michelberger, TFM Champion, MR Sprague, KT Kaczmarek, M Barbieri, XM Jin, DG England, WS Kolthammer, DJ Saunders, J Nunn, et al. Interfacing ghz-bandwidth heralded single photons with a warm vapour raman memory. *New Journal of Physics*, 17(4):043006, 2015.

[78] Omri Davidson, Ohad Yogev, Eilon Poem, and Ofer Firstenberg. Fast, noise-free atomic optical memory with 35% end-to-end efficiency. *arXiv preprint arXiv:2212.04263*, 2022.

[79] PD Kunz, NE Solmeyer, KC Cox, and DH Meyer. A cold-atom quantum memory for long distance quantum networks. In *2017 IEEE Photonics Society Summer Topical Meeting Series (SUM)*, pages 95–96. IEEE, 2017.

[80] L Heller, J Lowinski, K Theophilo, A Padrón-Brito, and H de Riedmatten. Raman storage of quasideterministic single photons generated by rydberg collective excitations in a low-noise quantum memory. *Physical Review Applied*, 18(2):024036, 2022.

[81] Sumit Bhushan, Vikas S Chauhan, and Raghavan K Easwaran. Ultracold rydberg atoms for efficient storage of terahertz frequency signals using electromagnetically induced transparency. *Physics Letters A*, 382(48):3500–3504, 2018.

[82] Neal Solmeyer, Xiao Li, and Qudsia Quraishi. High teleportation rates using cold-atom-ensemble-based quantum repeaters with rydberg blockade. *Physical Review A*, 93(4):042301, 2016.

[83] Taehyun Yoon and Michal Bajcsy. Laser-cooled cesium atoms confined with a magic-wavelength dipole trap inside a hollow-core photonic-bandgap fiber. *Physical Review A*, 99(2):023415, 2019.

[84] Michael E. Reimer, Gabriele Bulgarini, Nika Akopian, Moïra Hocevar, Maaike Bouwes Bavinck, Marcel A. Verheijen, Erik P.A.M. Bakkers, Leo P. Kouwenhoven, and Val Zwiller. Bright single-photon sources in bottom-up tailored nanowires. *Nature Communications*, 3(1):737, Mar 2012.

[85] K. P. Nayak, P. N. Melentiev, M. Morinaga, Fam Le Kien, V. I. Balykin, and K. Hakuta. Optical nanofiber as an efficient tool for manipulating and probing atomic fluorescence. *Opt. Express*, 15(9):5431–5438, Apr 2007.

[86] Xin Cao, Michael Zopf, and Fei Ding. Telecom wavelength single photon sources. *Journal of Semiconductors*, 40(7):071901, 2019.

[87] MS Safronova, UI Safronova, and Charles W Clark. Magic wavelengths, matrix elements, polarizabilities, and lifetimes of cs. *Physical Review A*, 94(1):012505, 2016.

[88] Jie Wang, Huifeng Liu, Baodong Yang, Jun He, and Junmin Wang. Determining the hyperfine structure constants of caesium 8s1/2 state aided by atomic coherence. *Measurement Science and Technology*, 25(3):035501, 2014.

[89] Suman Mondal, Sushree Subhadarshinee Sahoo, Ashok Kumar Mohapatra, and Amitava Bandyopadhyay. Formation of electromagnetically induced transparency and two-photon absorption in close and open multi-level ladder systems. *Optics Communications*, 472:126036, 2020.

[90] Miloš Rančić, Morgan P Hedges, Rose L Ahlefeldt, and Matthew J Sellars. Coherence time of over a second in a telecom-compatible quantum memory storage material. *Nature Physics*, 14(1):50–54, 2018.

[91] Andreas Wallucks, Igor Marinković, Bas Hensen, Robert Stockill, and Simon Gröblacher. A quantum memory at telecom wavelengths. *Nature Physics*, 16(7):772–777, 2020.

[92] Félix Bussières, Christoph Clausen, Alexey Tiranov, Boris Korzh, Varun B Verma, Sae Woo Nam, Francesco Marsili, Alban Ferrier, Philippe Goldner, Harald Herrmann, et al. Quantum teleportation from a telecom-wavelength photon to a solid-state quantum memory. *Nature Photonics*, 8(10):775–778, 2014.

[93] Jelena V Rakonjac, Dario Lago-Rivera, Alessandro Seri, Margherita Mazzera, Samuele Grandi, and Hugues de Riedmatten. Entanglement between a telecom photon and an on-demand multimode solid-state quantum memory. *Physical Review Letters*, 127(21):210502, 2021.

[94] Elena Arenskötter, Tobias Bauer, Stephan Kucera, Matthias Bock, Jürgen Eschner, and Christoph Becher. Telecom quantum photonic interface for a 40ca+ single-ion quantum memory. *npj Quantum Information*, 9(1):34, 2023.

[95] A Sieradzan, MD Havey, and MS Safronova. Combined experimental and theoretical study of the 6 p 2 p j→ 8 s 2 s 1/2 relative transition matrix elements in atomic cs. *Physical Review A*, 69(2):022502, 2004.

APPENDICES

Appendix A

Control sequence for M-LOOP with experiments

M-LOOP offers multiple ways to implement its machine learning models to an experiment, from its native Python to a command-line interface. Given that our preexisting experimental control software is written in LabVIEW, we were not able to utilize these interfaces. Thankfully, there exists a more generic means to share information between M-LOOP and any control software which is through the sharing of text files.

A.1   Interfacing with M-LOOP

An overview of the file interface with M-LOOP shall be discussed here. For control software written on Windows computers, one can initiate an M-LOOP instance through the command-line with[1]

```
1   $ M-LOOP.exe −c path\to\exp_config.txt >> results.txt
```

The location of the exp_config.txt will determine where M-LOOP will read and write to during the optimization run. This config file contains information about: the model

---

[1]When executing this through a program like LabVIEW or another language, it is important to make sure the shell remains open. For this, 'cmd /K' is added before 'M-LOOP.exe' to ensure the command line stays open after running the command.

(e.g. Guassian process), parameter space boundaries, parameter names, as well as exit conditions such as maximum duration and number of runs. Below is an example file that can be used to run M-LOOP:

```
1   interface_type = 'file'
2
3   num_params = 4
4   min_boundary = [0, -4.1, -4.0, 0.0]
5   max_boundary = [5, 4.1, 4.0, 10.0]
6   first_params = [2.2, -4.1, -4.0, 0.0]
7   controller_type = 'gaussian_process'
8   max_num_runs = 500
9   max_num_runs_without_better_params = 100
10  target_cost = 0.0000
11  max_duration = 3600
12  param_names = ['intensity','PGdetuning','MOTdetuning','Bfield']
13  training_filename = "...\\M-LOOP_archives\\learner_archive.txt"
14
15  #Learner options
16  cost_has_noise = True
17
18  #Timing options
19  no_delay = True
20
21  #File format options
22  interface_file_type = 'txt'
23  controller_archive_file_type = 'mat'
24  learner_archive_file_type = 'txt'
25
26  #Visualizations
27  visualizations = True
```

A few notable options shown above are the 'param_names' which helps navigating the results much easier as well as 'training_filename' which tells M-LOOP to use data from a previous run. Using data from a previous run can be helpful in the event that an experiment cannot be run in the time it takes to find the minimum cost value.

The piping command ('...>> results.txt') sends the output of the command line into the file 'results.txt'. Since M-LOOP will provide progress updates of this run (and any

errors) as output in the command line shell, it is good to have this stored in a file to access later and to read into your control software for user feedback.

Upon initiation, M-LOOP will begin by writing a text file, 'exp_input.txt', to the directory that the config file was written in. This file will have the format:

```
params = [2.2, −4.1, −4.0, 0.0]
```

From here, the control software should read this file and perform a cost function measurement using the parameter values written. The result of this measurement is to be written in a file called 'exp_output.txt' with the following format:

```
cost = 0.1
uncer = 0.01
bad = false
```

with two optional fields in 'uncer' for reporting known uncertainty in the measurement and 'bad' which tells M-LOOP that the measurement failed. For failed experiments, it is sufficient to only report 'bad = true'. The synchronization of communication between the control software and M-LOOP is done via the deletion of these files. M-LOOP will only search for and attempt to read 'exp_output.txt' when 'exp_input.txt' is deleted (by the control software). Conversely, the programmer of the control software can know when to read 'exp_input.txt' when the previously created 'exp_output.txt' has been deleted by M-LOOP. This avoids any potential errors from accessing files that have not been finished by the program.